

---

**Modelling the Last Glacial Maximum and Abrupt Climate Changes during  
the Last Glacial-Interglacial Cycle**

---

**Dissertation for the degree of  
Doctor of Natural Sciences  
submitted to  
Department of Physics/Electrical Engineering,  
University of Bremen**

**Xun Gong  
Bremen, October 2012**

Supervisor: **Prof. Dr. Gerrit Lohmann**

Department of Physics/Electrical Engineering,

University of Bremen

and Alfred Wegener Institute for Polar and Marine Research,

Bremerhaven

Referees: **Prof. Dr. Gerrit Lohmann**

Department of Physics/Electrical Engineering,

University of Bremen

and Alfred Wegener Institute for Polar and Marine Research,

Bremerhaven

**Prof. Dr. Peter Lemke**

Department of Physics/Electrical Engineering,

University of Bremen

and Alfred Wegener Institute for Polar and Marine Research,

Bremerhaven

## **Abstract**

The climate during the last glacial-interglacial cycle exhibits distinct climate states and variability in various time scales with different spatial characteristics. These changes occur for natural reasons, but their mechanisms are not well understood. Compared to the research on present-day climate, which involves influences of human activity, the investigation of the climate during the last glacial-interglacial cycle can attribute to discover the underlying process of natural climate change, and assist us to have a better prediction of future climate. Additionally, in comparison to studies on proxies, climate models provide a simplified numerical representation of dynamical and thermodynamical processes governing different components of the Earth's climate system, which is not able to be recorded in proxy data.

In this dissertation work, our first scientific focus is to clarify the mechanistic effects of a higher Northern Hemisphere ice sheet on large-scale North Atlantic Ocean surface circulation and Atlantic Meridional Overturning Circulation (AMOC) during glacial climate periods. We use the Community Earth System Models (COSMOS) to simulate five representative climate states during the last glacial-interglacial cycle: the Eemian interglacial, Mid Holocene, Pre-industrial (PI), stadial Marine Isotope Stage3 (MIS3), presented by 32 kilo years before present (ka B.P.), and Last Glacial Maximum (LGM). We have examined mean climatological states and variability of major large-scale North Atlantic Ocean surface circulation elements, including the Subtropical Gyre (STG), Subpolar Gyre (SPG), and Gulf Stream. Our results show that the existing Laurentide ice sheet and the elevated Greenland ice sheet induce increased surface winds over the North Atlantic Ocean during the LGM and MIS3, which subsequently enhance the North Atlantic gyres and the Gulf Stream. In addition, statistical analysis suggests that the correlation between AMOC and surface winds is increased during glacial climate states.

The second part of our work is targeted at the explanation of the difference of abrupt decadal climate changes during the last glacial-interglacial cycle. As documented in Greenland ice cores, abrupt decadal climate changes are less pronounced during maximum glacial conditions and strongly suppressed during the Holocene. We conduct hosing experiments for three different climate states during the last glacial-interglacial cycle (PI, 32 ka B.P. and the LGM). Our results show that the freshening of the surface North Atlantic Ocean leads to a similar reduction of the AMOC due to the freshwater perturbation, independent of the background climate. However, the subsequent recovery stages show distinct tempo-spatial characteristics, with respect to the initial AMOC resumption and the strength of a superposed AMOC overshoot. During the initial AMOC resumption, a stronger temperature inversion between the surface and intermediate layer (200-800 m) in the South Labrador Sea induces a quicker restart of convective processes (32ka B.P. > LGM > PI). A few decades later, an AMOC overshoot is caused by the advection of warmer and saltier tropical Atlantic Ocean water into the South Labrador Sea. In case of a glacial climate background, this provides a strong positive feedback on the initial resumption. In comparison to the 32ka B.P. experiment, this feedback is noticeably weaker during the LGM, and completely absent during the PI. Furthermore, the temporal isolation of South Labrador Sea and Greenland-Iceland-Norwegian Sea contributions to the AMOC overshoot highlights the combined role of the tropical Atlantic Ocean and the South Labrador Sea response to the overshoot dynamics. The dependence of the AMOC overshoot and the associated climatic response on the climate state provides a coherent concept in agreement with pronounced rapid climate changes during glacial times, as recorded by proxy data.

In addition to use fully coupled atmosphere-ocean model for the studies of different mechanistic processes in the Earth's climate system, we employ a regional high-resolution ocean model (the North Atlantic/Arctic Ocean-Sea Ice Model) for further understanding of the

hydrographic process of the surface Nordic Seas during the LGM, which has been reconstructed to be in different conditions by proxies in the CLIMAP (the Climate Long-Range Investigation, Mapping and Prediction) and GLAMAP (the Glacial Atlantic Ocean Mapping) projects. Using the atmospheric forcing corresponding to the CLIMAP and GLAMAP indicated surface ocean, our experiments successfully rediscovered the sea surface temperatures (SSTs) and sea ice cover, in agreement with the proxy reconstructions. Furthermore, the internal dynamics in our LGM experiments provide an intermediate cooling conditions in the Nordic Seas, colder than the GLAMAP reconstruction, but warmer than the CLIMAP reconstruction during the LGM. Furthermore, both the GLAMAP and CLIMAP atmospheric forcing lead to similar directions and magnitudes of surface ocean circulation in the Nordic Seas during the LGM, in spite of distinct features of the SSTs and sea ice cover.

# 1 Introduction

The last glacial-interglacial cycle refers to the time period covering the last alternation of glacial and interglacial climate states on the time scale of 100 kilo years (ka). More accurately, it begins with the Eemian interglacial and lasts to present [Dansgaard et al., 1993]. The Earth's climate during the last glacial-interglacial cycle as recorded by proxies has a large variability in both spatial and temporal features.

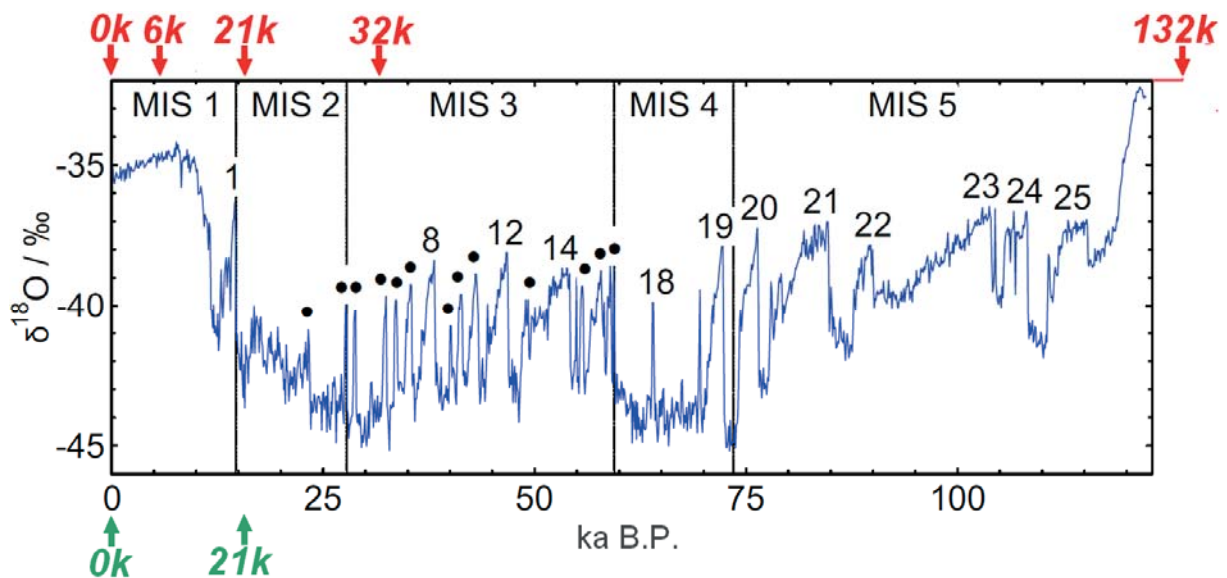


Figure 1.1. The oxygen-isotope data in the Greenland NGRIP ice core lasting from the present back to 123 ka B.P. (after Wolff [2010]). The Numbers indicate the occurrences of Dansgaard-Oeschger events (D-O). In addition, the red arrows show the time slices that are simulated by the Community Earth System Models (COSMOS), and presented in Chapter 3 and 4. The green arrows show the time periods that are simulated using the North Atlantic/Arctic Ocean-Sea Ice Model (NAOSIM) in Chapter 5.

Regarding oxygen isotope records obtained from deep-sea planktonic foraminifers cores, the last glacial-interglacial cycle can be subdivided into five periods, i.e. Marine Isotope Stage (MIS) 5, 4, 3, 2 and 1 [Aitken, 1997]. MIS5, approximately 130–74 ka before present (ka B.P.), experiences globally cooling process from a peak warm climate state (the MIS5e, also named as the Eemian interglacial) [Oppo et al., 2001]. Despite a large basis of a diversity in time definition by different proxy evidence, the climate during the Eemian interglacial is often referred as the period ~130–110 ka B.P. [Shackleton et al., 2003], which has a higher global mean surface air temperature (SAT) compared to the present, accompanied by a 4-6 m sea level rise. MIS5 exhibits a strong climate cooling in the following 36 ka. Subsequently, MIS4 (approximately 74–60 ka B.P.) represents the second last maximum glacial climate, with similar climate conditions as during the Last Glacial Maximum (LGM, 23-18 ka B.P.) [North Greenland Ice Core Project Members, 2004]. After a climate recovery within a few kilo years, the MIS3 epoch represents the climate transition approaching the LGM between 60 and 24 ka B.P., and well known for various rapid stadial-interstadial climate changes and variability [Huber et al., 2006]. MIS2 covers the time period including the LGM and the climate evolution until the end of the Younger Dryas (~12 ka B.P.). During the LGM, the Northern Hemisphere ice sheet reaches their maximum extension, accompanied by a ~116 m sea level drop [Clark et al., 2009]. At the beginning of the Holocene epoch (~ 11 ka B.P.), the Earth's climate enters the latest period MIS1, which is still ongoing, and regarded as a relatively stable interglacial period, yet still displays various climate fluctuations [Wanner, et al., 2008].

Over all time scales, Earth's climate change and variability occur in various spatio-temporal features, and are driven by external forcings and internal processes (Figure 1.2). Weather systems can rapidly change within a few months, while climate-related processes are slower. The basin-scale ocean circulation and climate indexes of atmospheric circulation, such as the

North Atlantic Oscillation (NAO) [Walker, 1924] and the El Niño–Southern Oscillation (ENSO) [Bjerknes, 1969], show variation periods of decades. Furthermore, little ice ages may happen on the time scale of centuries [Eddy, 1976; Brovkin et al., 2009]. As shown in Figure 1.2, the millennial-scale climate change during the last glacial-interglacial cycle, as the time scale studied in this dissertation, is closely related to the Milankovitch cycles, and variations in greenhouse gases and ice sheets. The tectonic effect of continental drift and Mountain uplift to millennial-scale climate variations is negligible, but becomes important for climate research on the time scale longer than millions of years (Figure 1.2). In contrast, the consequences of sea level and ice sheet variations on the topography are carefully considered in our work.

Overall, the combination of non-tectonic topography, orbital parameter and greenhouse gas concentrations mostly determine millennial-scale climate change during the last glacial-interglacial cycle. In the theory of Milankovitch cycles, three parameters are used to describe the Earth's orbits: eccentricity, precession and obliquity [Milankovitch, 1920]. In comparison, eccentricity has the longest period of 100 ka and 400 ka, followed by precession (19 and 23 ka) and obliquity (41 ka) (Figure 1.3a-c). The superposition of these astronomical cycles determines local annual mean amount of solar radiation that arrives at the top of atmosphere, and the intensity of seasonality. Then, the greenhouse gas concentrations in the atmosphere decide the actual proportion of total solar energy entering in the Earth's climate system (Figure 1.3d, e, f). However, it is debated whether the greenhouse effect acts as a trigger or acts as a mechanism providing positive feedback to climate warming (e.g. Delmas et al., [1980]; Neftel et al., [1980]; Lüthi et al., [2008]; Shakun et al., [2012]). In contrast, the variation of ice sheets is firstly a pure response to the change of temperature and precipitation, and then subsequently provides strong feedbacks in the mechanisms of both thermodynamics

and dynamics [Scambos et al, 2000; Pausata et al., 2011].

It is well-known that the spatio-temporal features of the North Atlantic Ocean are sensitive to regional and global climate change. In particular, the variability of the Atlantic Meridional Overturning Circulation (AMOC) is regarded as a comprehensive indicator diagnosing climate variations. Aiming at a further understanding of climate change during the last glacial-interglacial cycle, it is essential to untangle the evolution of the North Atlantic Ocean circulation during past interglacial and glacial periods and differences between these periods, which is also important for understanding the present-day (PD) state, and assessing future climate change.

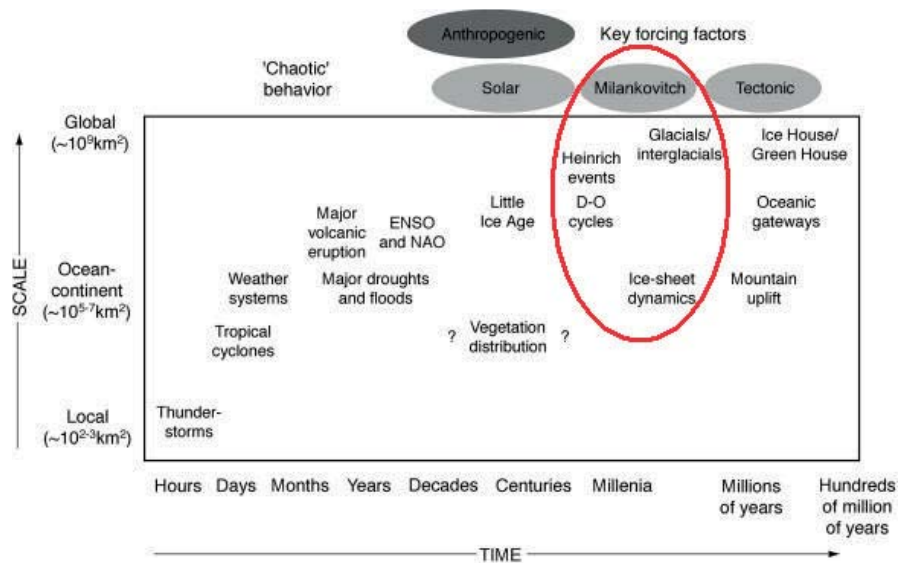


Figure 1.2. The spatial and temporal dimensions of the Earth's climate system plotted on logarithmic scales. The red circle indicates the millennial-scale climate events and corresponding climate forcing (after [Maslin and Christensen, 2007]).

Compared to the studies of proxy data, modeling work can provide a more detailed description of the underlying physical processes, and favors a better understanding of the

proxies by exhibiting regional climatic features with global feedbacks. In this dissertation work, our focus is to simulate and explain distinct features of the North Atlantic Ocean and Nordic Seas (the Greenland Sea, Iceland Sea and Norwegian Sea) climate systems during glacial and interglacial periods:

In Chapter 2, we present the model details regarding to the Community Earth System Models (COSMOS) and the North Atlantic/Arctic Ocean-Sea Ice Model (NAOSIM).

In Chapter 3, we try to untangle the mechanistic influence of the existence of the Laurentide Ice Sheet and elevated Greenland Ice Sheet on the North Atlantic Ocean circulation during glacial climate periods. The North Atlantic Ocean circulation and AMOC have been recorded by proxies to be different between glacial and interglacial climate states [e.g. CLIMAP, 1981; Slowey and Curry, 1992; de Vernal et al., 2002; Pflaumann, et al., 2003; McManus et al., 2004; Vautravers et al., 2004; Van Meerbeeck et al., 2009]. In previous mechanism studies, the changes in the North Atlantic Ocean surface circulation are demonstrated to closely related to the changes in surface winds [Munk and Palmen, 1950; Rhines and Schopp, 1991]. Subsequently, Pausata et al. [2011] use atmosphere general circulation model (AGCM) to explain that the differences in the atmospheric circulations between glacial and interglacial climate states are attributed to higher elevation of glacial ice sheet. Here, we use a fully coupled atmosphere-ocean model to simulate five different climate states of the Eemian interglacial, Mid Holocene, Pre-industrial (PI), stadial MIS3 and LGM, which show differences in ice sheet volume. In addition, we detect the changes of surface winds, also the strength of the North Atlantic gyres, Gulf Stream and AMOC<sup>1</sup>.

---

<sup>1</sup> A large part of this chapter has been submitted to the *Journal of Geophysical Research – Oceans*: Gong, X., X.d. Zhang, G. Lohmann, W. Wei, X. Zhang, and M. Pfeiffer (2012): Intensification of Glacial North Atlantic Gyres and Meridional Overturning Circulation due to elevated Northern Hemisphere Ice Sheet.

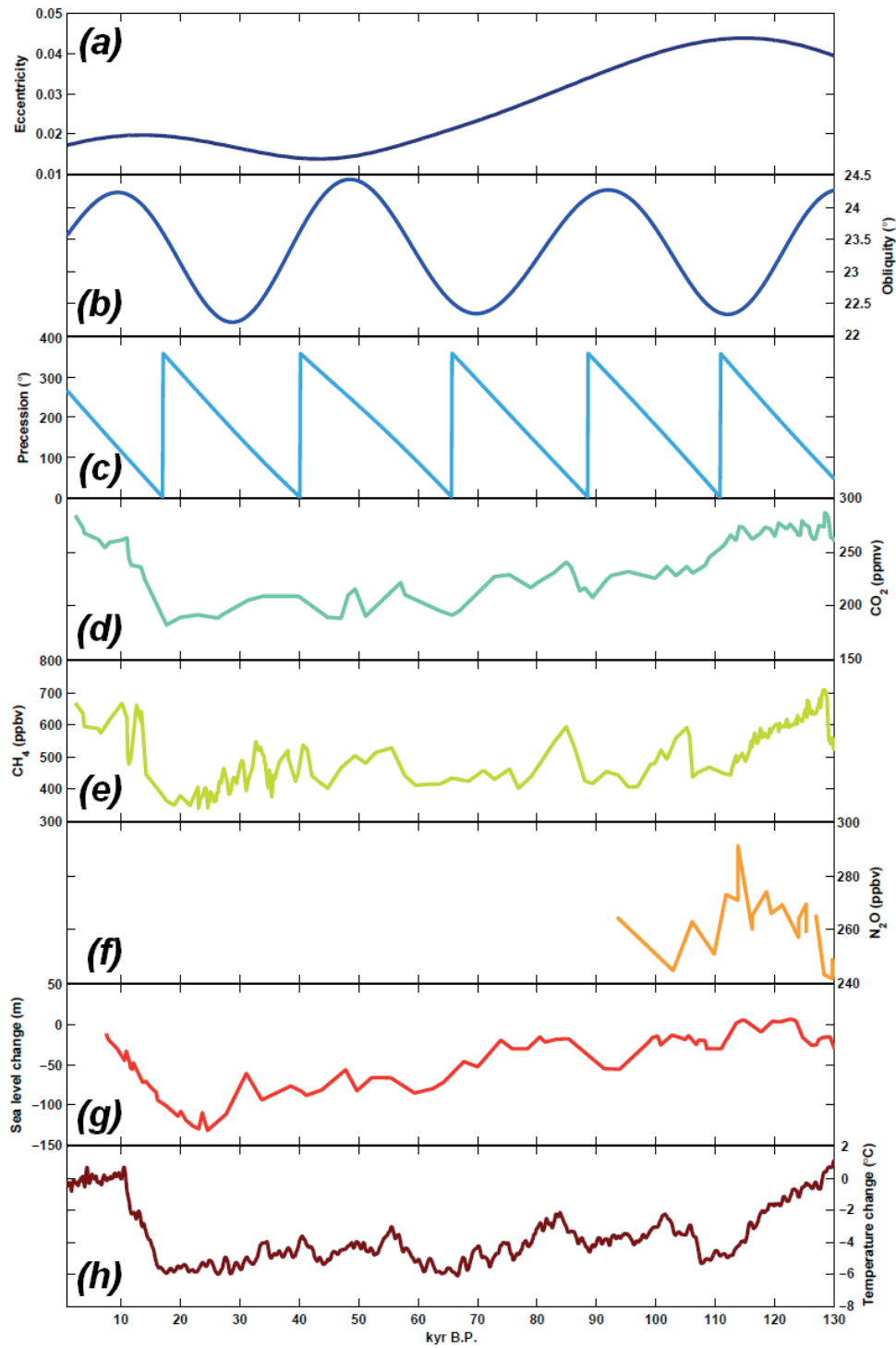


Figure 1.3. Time series of (a-c) orbital parameters [Laskar et al., 2004], (d-f) greenhouse gas concentrations [Petit et al., 1999], (g) sea level [Waelbroeck et al., 2002] and (h) Earth's surface temperature [Petit et al., 1999] over the last 130 ka.

In Chapter 4, as recorded in Greenland ice cores, abrupt decadal climate changes during the last glacial-interglacial cycle exhibit different features, which are less pronounced during maximum glacial conditions and strongly suppressed during the Holocene [Dansgaard et al., 1993] (Figure 1.1). The records of sedimentary nutrient proxy evidence and kinematic proxies indicate a notable correlation of abrupt climate changes and variations in the Atlantic meridional overturning circulation (AMOC) [e.g. McManus et al., 2004; Thornalley et al., 2011]. However, the mechanism resulting in these various abrupt decadal climate changes are still unclear. Hu et al. [2008] and Renold et al. [2010] reveal a gradual and two-phase recovery of the AMOC under the present and LGM conditions, and they emphasize the roles of the Bering Strait and the Greenland-Iceland-Norwegian Sea (Nordic Seas) on these AMOC variations, respectively. Prange et al. [2004] performed freshwater hosing experiments with a model of intermediate complexity for different glacial background states and found a two-step relaxation for background conditions with convection sites in the South Labrador Sea and the Nordic Seas, and a slower response for an AMOC background state without convection in the Nordic Seas. Moreover, the AMOC stability behavior and sensitivity to freshwater perturbations has been shown to be dependent on the background climate condition (e.g. Prange et al., 2003; Prange et al., 2004; Knorr and Lohmann, 2007). By conducting hosing experiments for three different climate states during the last glacial-interglacial cycle (the PI, 32 ka B.P. and LGM), we examine the spatio-temporal hydrographic characteristics and the deep-water formation in the South Labrador Sea and the Nordic Seas, and compare their distinct features based on background climate states<sup>2</sup>.

In Chapter 5, we focus on the state of the Nordic Seas during the LGM. The ocean dynamics in the Nordic Seas crucially influence regional and global climate changes, also sensitive to

---

<sup>2</sup> Most parts of this chapter have been submitted to the *Geophysical Research Letters*: Gong, X., G. Knorr, G. Lohmann, and X. Zhang (2012): *Dependence of abrupt Atlantic meridional ocean circulation changes on climatic states*.

their feedbacks [Hass, 1996; Rahmstorf, 1999; Kösters et al., 2005; Köhl et al., 2007]. In the study of the Nordic Seas during the LGM, the proxy records used in CLIMAP (the Climate Long-Range Investigation, Mapping and Prediction) and GLAMAP (the Glacial Atlantic Ocean Mapping) show extremely different sea surface conditions and sea ice cover [CLIMAP, 1981; Pflaumann et al., 2003; Paul and Schäfer-Neth, 2004]. Additionally, Braconnot et al. [2007] and Otto-Bliesner et al. [2007] show large spreads of simulating the glacial Nordic Seas between different Earth System Models (ESMs). Therefore, we apply the high-resolution NAOSIM model for better understanding of the underlying physical processes in the Nordic Seas during the LGM<sup>3</sup>.

In Chapter 6, summaries are given for the works in Chapter 3-5, and also future perspectives are outlined.

---

<sup>3</sup> *Parts of the work and results in this chapter are in preparation for a paper. Some basic description of experiments and the analysis of glacial Arctic sea ice have been recently accepted by the Earth and Planetary Science Letters: Stärz, M., X. Gong, R. Stein, D. A. Darby, F. Kauker, and G. Lohmann (2012): Glacial shortcut of Arctic sea-ice transport.*

## 2 Methodology

In this dissertation work, two numerical models are used: a coupled general circulation model i.e. the Community Earth System Models (COSMOS), and a high-resolution coupled ocean - sea ice model, i.e. the North Atlantic/Arctic Ocean - Sea Ice Model (NAOSIM). Depending on scientific questions, several experiments are conducted with distinctive model setups. In this chapter, we give detailed model descriptions for both COSMOS and NAOSIM, and experimental setups will be introduced in Chapters 3-5, respectively.

### 2.1 Model description for the COSMOS model

COSMOS is a global, fully coupled ocean - atmosphere - sea ice - land surface model. It was developed by the Max-Planck-Institute for Meteorology, and hierarchy improved in the Alfred Wegener Institute for Polar and Marine Research (AWI). Our version of COSMOS includes four components: the atmosphere component (atmosphere GCM - ECHAM5), the ocean component (ocean GCM - MPIOM), the land surface component (land surface vegetation model - JSBACH) and the coupler (OASIS3). The ECHAM5 utilizes a horizontal resolution of  $\sim 3.75^\circ \times 3.75^\circ$  with 19 hybrid sigma pressure levels in vertical [Röckner et al., 2003] (Figure 2.1a). For the ocean, MPIOM uses a formal horizontal resolution of  $\sim 3^\circ \times 1.8^\circ$  and on uneven 40 vertical layers [Marsland et al., 2003], and the resolution can be higher than  $1^\circ \times 1^\circ$  around the two grid poles over the Greenland and the Antarctic continent (Figure 2.1b). Over the land, JSBACH operates on the same horizontal grid as ECHAM5 [Raddatz et al., 2007], using eight simplified vegetation types in the simulation for land surface, as shown in Figure 2.2. Our COSMOS are run by the AWI super computer (NEC - SX8), the time step of computation is 86400 seconds (for the ocean) and 2400 seconds (for the atmosphere).

In ECHAM5, routines of river runoffs are prescribed, and subsequently the amounts of river runoffs are dynamically integrated according to global hydrological cycle in ECHAM5 (Figure 2.3) [Hagemann and Dumenil, 1998]. Further details of COSMOS refers to Stepanek and Lohmann [2012].

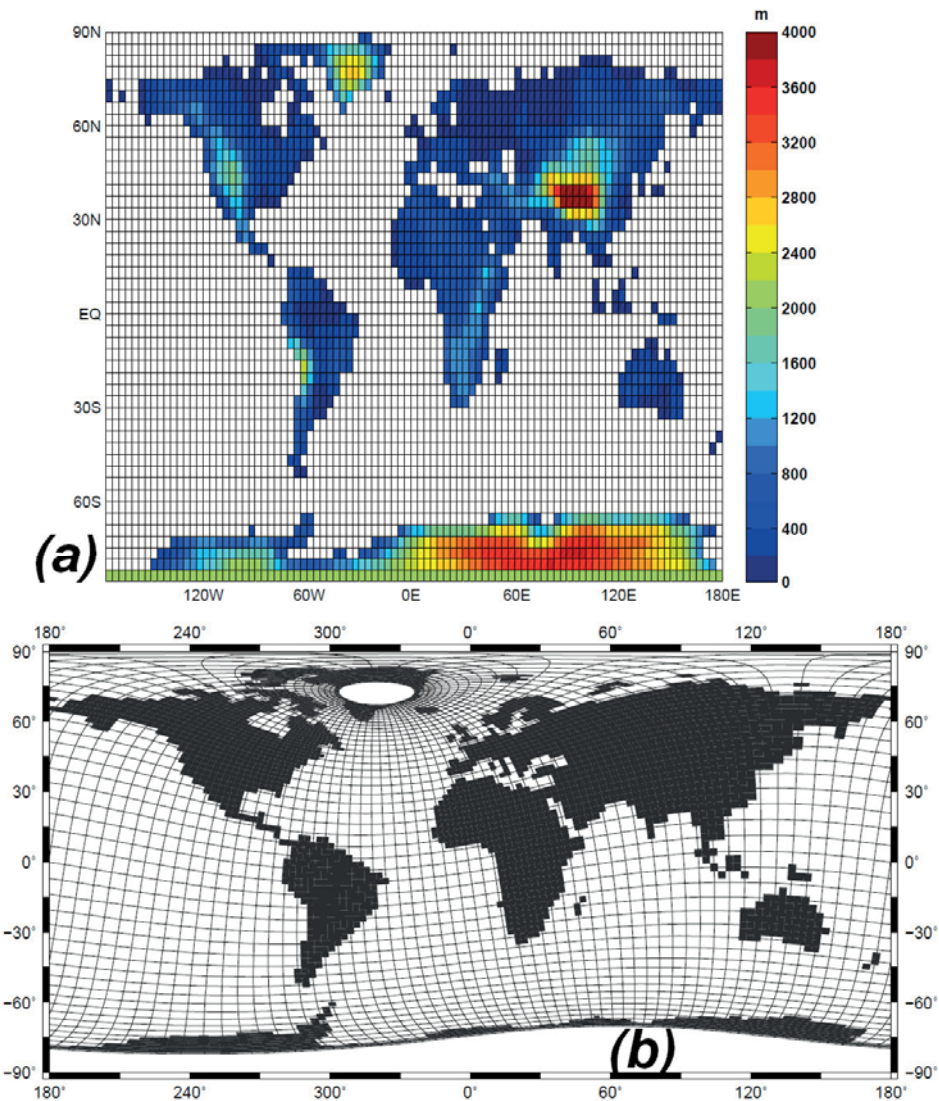


Figure 2.1. Model grids of (a) ECHAM5 and (b) MPIOM. The land area in MPIOM is indicated by black area, and the grid poles are marked white. The variation of surface altitude in ECHAM5 is shown by a color map.

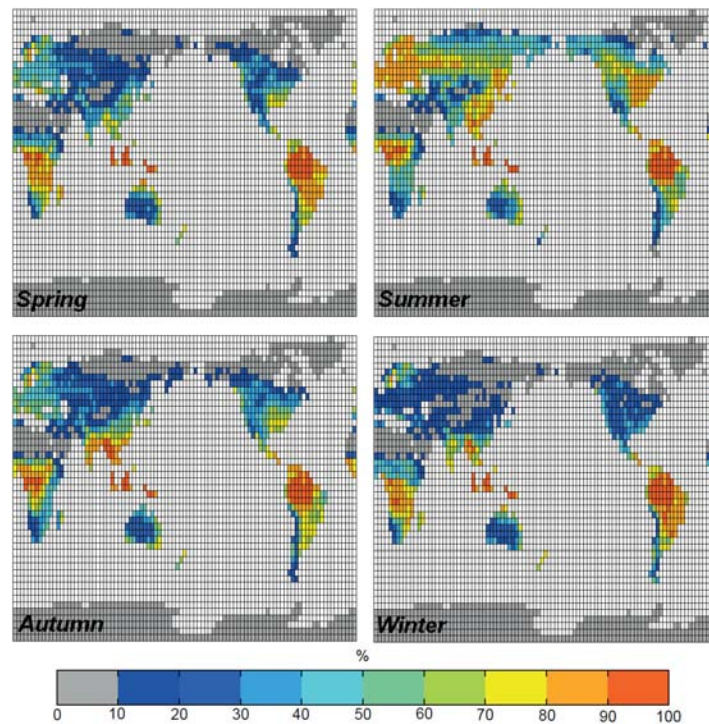


Figure 2.2. Present seasonality of the vegetated fractions of land grid, simulated by JSBACH.

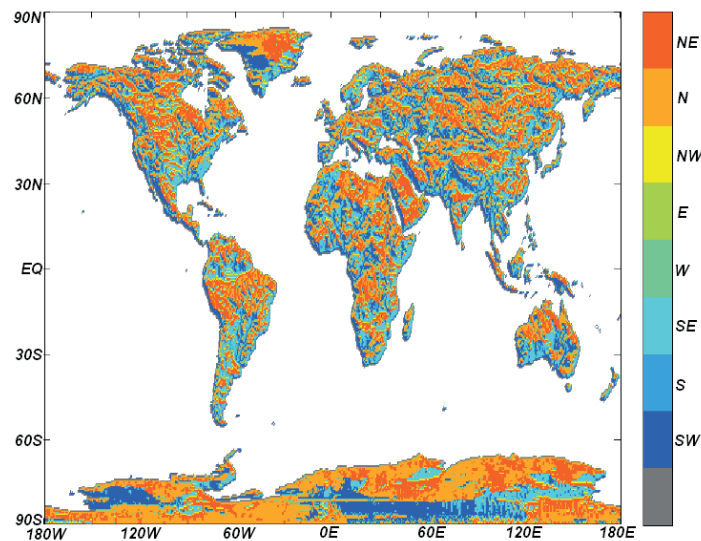


Figure 2.3. Present river directions in ECHAM5, shown in the horizontal resolution of  $0.5^\circ \times 0.5^\circ$  of the hydrological model. Grey indicates locations where river runoffs enter the ocean (after Stepanek and Lohmann [2012]).

## 2.2 Model description for the COSMOS model

NAOSIM is a regional, coupled ocean - sea ice model, which is derived from the Geophysical Fluid Dynamics Laboratory modular ocean model MOM-2 [Pacanowski, 1995; Zalesak, 1979], and hierarchy developed at AWI [Kauker et al., 2003; Köberle and Gerdes, 2003]. NAOSIM solves the primitive equations for the horizontal velocity components, temperature, and salinity. Subsequently, the vertical velocity, density, and pressure are calculated from diagnostic equations. The advection of tracers is handled by a flux-corrected transport scheme (Zalesak 1979; Gerdes et al. 1991), and the implicit diffusion associated with the advection scheme is the only diffusion acting on the tracers. In NAOSIM, frictions are implemented as Laplacian diffusion of momentum with horizontal and vertical viscosities of  $2.5 \times 10^4 \text{ m}^2 \text{ s}^{-1}$  (horizontal) and  $10^{-3} \text{ m}^2 \text{ s}^{-1}$  (vertical), respectively [Köberle and Gerdes, 2003].

Our high-resolution version of NAOSIM is formulated on a spherical rotated grid of  $0.25^\circ \times 0.25^\circ$ , and 30 unevenly spaced levels in vertical. The rotation of the grid shifts the equator to geographical  $30^\circ \text{W}$  and North Pole to  $(0^\circ \text{N}, 60^\circ \text{E})$ , which is realized as following transformation:

$$\begin{cases} geolat(i, j) = \max\left(-\frac{\pi}{2}, \min(90.0, \arcsin(\cos(mlat(i, j)) \times \cos(mlong(i, j))))\right) \\ geolon(i, j) = \text{mod}\left(\frac{11}{6}\pi + \left| \frac{\arccos(\cos(mlat(i, j)) \times \sin(mlon(i, j)) \times \cos(mlon(i, j)))}{\cos(\arcsin(\cos(mlat(i, j))))} \right|, 2\pi\right) \end{cases}$$

where,  $geolat(i, j)$  &  $geolon(i, j)$  are geographical latitude and longitude, and  $mlat(i, j)$  &  $mlon(i, j)$  are north-south and east-west coordinate in the model. As shown in Figure 2.4, NAOSIM covers the oceanic area including the Arctic Ocean, Nordic Seas and part of the northern North Atlantic Ocean Northward of  $50^\circ \text{N}$ .

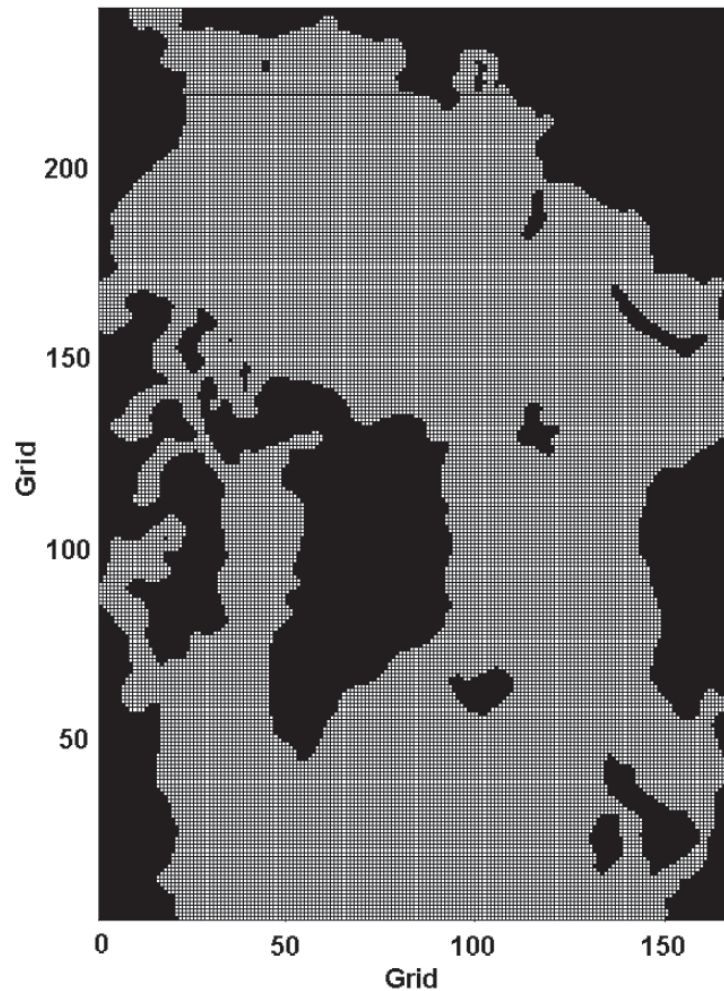


Figure 2.4. Model grids (approximately  $0.25^\circ \times 0.25^\circ$ ) of the NAOIM model for PDconditions. The land area is shadowed with black.

NAOSIM applies the Etopo5 data for the present ocean topography, with a modification of opening two channels in the Canadian Archipelago Seas [Levitus, 1982]. Moreover, the  $50^\circ\text{N}$  ocean boundary is open for water outflows, radiation of waves and sea ice drift [Stevens, 1991]. In the PD control experiment, the initial forcing uses the Arctic Ocean EWG climatology data of winter season (by Environmental Working Group joint U.S.-Russian atlas of the Arctic Ocean) [Steele et al., 2001]. As a compensation, the data of Levitus [1982] is used for the ocean parts, where exceeds the EWG area. Using the same data, surface salinity

restoring is performed every 180 days. Across the Bering Strait, a 0.8 Sverdrup (Sv) inflow towards the Arctic Ocean is applied in PD control experiment. Coupled with the oceanic part, the sea ice dynamics module employs a viscous-plastic rheology [Hibler, 1979], and the thermodynamic calculation is based on the theory of Semtner [1976]. At ocean surface, we use various variables to force our version of NAOSIM, including 2m air temperature, 2m dew point temperature, total cloud cover, net precipitation, sea surface wind speed and wind stress.

## **2.3 Statistical Analysis**

In the following Chapters, the statistical calculation of correlation, time lagged cross-correlation and t-test are used for the time series of North Atlantic surface winds, the strength of North Atlantic gyres and AMOC, which helps to clarify the variations of these climate index along with climate fluctuations in each climate state. The method details can be found in the book of Storch and Zwiers [2002].

### **3 Intensification of glacial North Atlantic gyres and meridional overturning circulation due to elevated northern Hemisphere ice sheet**

North Atlantic Ocean circulation constitutes an important branch of the Earth's climate heat engine, and plays a crucial role in modulating global and regional climate variability and change. The common view is that North Atlantic Ocean circulation transports warmer surface water from lower latitudes to subpolar basins, driven by surface winds and buoyancy contrasts, which are related to differential temperature and salinity stratification [Lynch-Stieglitz, 2001; Cianca et al., 2009; Dzhiganshin and Polonsky, 2009; Häkkinen and Rhines, 2009]. As an integral element, the AMOC is a prominent diagnostic of vertical circulation contributing to meridional water mass and heat exchange between low and high latitudes [Keigwin et al., 1994]. At the surface, the complex North Atlantic Ocean circulation can be simplified and represented by three main components: the Subtropical Gyre (STG), the Subpolar Gyre (SPG), and the Gulf Stream. Munk and Palmén [1950] gives a classic explanation of the dynamics of wind-driven ocean circulation, and finds that the solution for zonal winds gives the main gyres of North Atlantic Ocean circulation. The Gulf Stream is an important component of this surface gyre system. In subsequent work on 'wind-ocean circulation' mechanisms by Rhines and Schopp [1991], the wind stress curl zero line is identified as a boundary between the SPG and the STG. A change of northward subtropical water transport occurs when this boundary shifts. Additionally, the connection between the subtropical and the high-latitudes North Atlantic Ocean is strengthened when the wind stress curl zero line has a larger meridional tilt, and conversely it weakens when the zero line penetrates more zonally [Häkkinen and Rhines,

2009]. By diagnosing various factors influencing the meridional heat transport in the Atlantic Ocean, Marshall et al. [2001] suggests that North Atlantic gyres can potentially compensate the change of meridional heat transport with respect to the variability of the AMOC. Additionally, Hofmann and Ramstorf [2009] illustrates that subpolar and subtropical gyre changes in the North Atlantic Ocean can induce instability of the AMOC with respect to surface wind changes. Furthermore, the study of Montoya and Levermann [2008] points out that stronger wind stress during glacial periods can enhance northward salt transport in the North Atlantic Ocean, and act as a threshold for the deep-water formations to the south of Greenland. Therefore, North Atlantic Ocean circulation is considered to be essential in untangling past climate variability and change, which may also have important implications for understanding PD and future climate changes.

To understand the role of the North Atlantic Ocean circulation during the last glacial-interglacial cycle, numerous efforts have been made [e.g. McManus et al., 2004; Van Meerbeeck et al., 2009]. In the subtropical North Atlantic Ocean, vertical ventilation is found to be strengthened during glacial periods [Slowey and Curry, 1992]. The GLAMAP indicates that the position of the anticyclonic subtropical gyre during the LGM was close to that during the PI time period [Pflaumann, et al., 2003]. Both the CLIMAP [CLIMAP, 1981] and GLAMAP [Pflaumann, et al., 2003] found that the north polar water can be tracked as far south as 45°N, and the North Atlantic drift during the LGM locates at similar position as present. Meanwhile, the ocean water density estimated by multi-proxy data suggests conditions unfavorable for vertical convection and support the hypothesis of the spreading of a shallow, low-salinity buoyant layer over the northern North Atlantic Ocean during the LGM [de Vernal et al., 2002]. Additionally, it is found that a strong variation of the AMOC occurs with stadial-interstadial climate changes during MIS3, accompanying a high frequency

variability of the strength of the Gulf Stream [Vautravers et al., 2004; Van Meerbeeck et al., 2009]. All of these existing studies demonstrate large differences of the North Atlantic Ocean circulation between glacial and interglacial climate periods. However, there has been a lack of coherent descriptions of these differences, and underlying physical processes are still unclear. Here, we employed COSMSO to simulate four paleo climate states and the PI, which is performed as the reference control run. The Mid Holocene (6 ka B.P.) generally has a warm climate relative to PI, especially over the high latitudes of the North Hemisphere [Dansgaard et al., 1993]. During the Eemian (132 ka B.P.), the Earth climate becomes even warmer [Shackleton et al., 2003]. Revealed by the temperature reconstruction from ice core and ocean sediments, the LGM is the coldest climate state in the past 100 ka [Clark et al., 2009]. And, MIS3 is a geological epoch before the LGM (from 60 to 27 ka B.P.), when the Earth climate system approaches the LGM conditions, and exhibits strong stadial-interstadial climate variations [Dansgaard et al., 1993]. Here, we use a stadial MIS3 state at 32 ka B.P. as the representative climate state that is warmer than the LGM and colder than the PI period.

In our work, we diagnose the variations of the North Atlantic Ocean surface circulation and AMOC for these representative climate states during the last glacial-interglacial cycle. Particularly, we focus on revealing potential anomalies of the underlying dynamics in the ‘wind-gyre-AMOC’ system between glacial and interglacial climate states, which are hypothesized to be different with respect to the existence of the Laurentide Ice Sheet and elevated Greenland Ice Sheet during the glacial periods.

### **3.1 Experiment design for five climate states during the last glacial-interglacial cycle**

In order to simulate the past climate states, different external forcings and land-sea masks are required. Orbital forcing is inferred by Berger [1978], and greenhouse gas concentrations from the reconstructions using ice cores, including CO<sub>2</sub> [Indermühle et al., 1999], CH<sub>4</sub> [Brook et al., 2000] and N<sub>2</sub>O [Sower et al., 2003] (Table 3.1). The major differences of land-sea masks in the five simulations are due to sea level change and the variations of ice sheet coverage and thickness. For the LGM simulation, the paleo topography data are provided by the Paleoclimate Modelling Intercomparison Project Phase III (PMIP3, <http://pmip3.lsce.ipsl.fr/>), which prescribes that the sea level is 116m lower during the LGM than the PI. The ice sheet volume reaches a maximum in the Northern Hemisphere high latitudes (Figure 3.1c). By 7-8 ka B.P., the Laurentide Ice Sheet has mostly melted, and the Greenland Ice Sheet is almost equivalent to that in the PI [Overpeck et al., 2006]. According to PMIP3 protocol, the ice sheet and sea level during the Mid Holocene use the same set up as in the PI simulation [Crucifix et al., 2005; Wei et al., 2012]. Additionally, the land-sea mask in the Eemian simulation remains as in the PI, whereas the Greenland Ice Sheet is reduced by a half with respect to warmer SAT (Figure 3.1a) [Petit et al., 1999]. In the MIS3 simulation, sea level is decreased by 80 m relative to the PI [Köhler et al., 2011; Thompson and Goldstein, 2006]. According to the reconstructed data by the ICE-5G ice sheet model, the total volume of the Laurentide and Greenland ice sheets are smaller than those under the LGM conditions, and distributed differently [Peltier, 2004] (Figure 3.1d). Furthermore, the pathways of paleo rivers are also changed with respect to new topographies, calculated by a hydrological discharge model [Hagemann and Dümenil, 1998]. Consequently, the COSMOS model can dynamically calculate the river discharges according to the global hydrological cycle. The

simulations for PI and paleo climate periods have been used to test different climatologic features and variability on respective climate period (e.g. Wei et al., [2012]; Wei and Lohmann, [2012]; Zhang et al., [2012]).

To initialize COSMOS for different simulations, the ocean component MPIOM uses the Levitus' [1982] hydrographic data. In addition, the salinity of the entire ocean in the LGM and MIS3 simulations are respectively 1psu and 2/3 psu higher than PI, with respect to the salinity conservation due to the sea level change. Based on Zhang et al. [2012], the LGM ocean may have two quasi-steady states via the application of different initial conditions, which results from the difference in ocean deep layers. However, these states have similar surface ocean hydrographic properties and surface atmospheric circulation. In all our simulations, the atmospheric and land surface initialization are integrated from the PI state. Each simulation is run for 2000 years, where it reaches its quasi-equilibrium state. A climatology mean over the last 200 years is used to represent each climate state.

According to studies examining trajectories of Lagrangian drifters deployed under observation and model simulations, the subtropical and subpolar exchange in the North Atlantic Ocean is primarily located at the subsurface [Burkholder and Lozier, 2011]. Therefore, we use the upper 200 m mean ocean circulation to represent the surface North Atlantic Ocean in our analysis.

Table 3.1 Orbital parameters and greenhouse gas concentration in each COSMOS simulation.

	Eemian	Mid Holocene	PI	MIS3	LGM
Precession (°)	49.097	180.918	282.157	116.474	294.42
Obliquity (°)	24.2441	24.1048	23.4468	22.3620	22.949
Eccentricity	0.038231	0.018682	0.016724	0.015732	0.018994
CO2 (ppmv)	278	280	280	200	185
CH4 (ppbv)	650	760	650	450	350
N2O (ppbv)	270	270	270	220	200

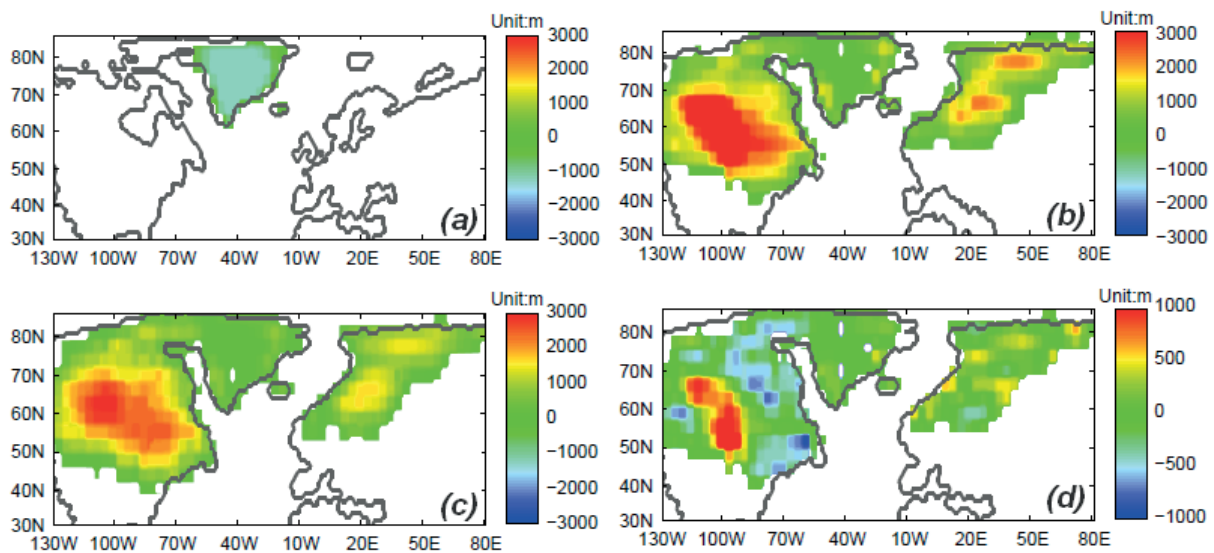


Figure 3.1. The anomaly of ice sheet thickness relevant to the PI in the (a) Eemian (b) MIS3 (c) LGM. The panel (d) shows the anomalous ice sheet thickness during the MIS3 minus that under the LGM condition.

## **3.2 COSMOS simulations for five climate states**

### **3.2.1 The North Atlantic surface winds**

We use the PI simulation as our control run, and also use it as a reference state when comparing with other climate states. As shown in Figure 3.2a, the PI surface wind field is characterized by three main wind systems. The easterly trade wind prevails throughout the tropics between 10°N and 30°N, whereas it turns in a north-easterly direction joining in the mid-latitude wind system over the North American Continent. Between 40°N and 60°N, the North Atlantic Ocean is dominated by the westerlies, which have a maximum wind speed along 50°N. Additionally, a cyclonic wind system forms over the region around Iceland.

Compared to the PI, the surface wind fields in the other four simulations demonstrate various changes, as expected (Figure 3.2b-e). In the Eemian simulation, the easterlies are noticeably weaker over the tropical North Atlantic Ocean, whereas the cyclonic wind system above the Nordic Seas becomes stronger. A most pronounced change occurs over the Greenland, which results from a reduced ice sheet volume. Comparably, the surface winds in the Mid Holocene simulation resemble those in the PI. In the simulations for the glacial climates (i.e. the LGM and MIS3), tremendous changes are exhibited with respect to the interglacial (i.e. the PI, Mid Holocene and Eemian period). Prominently, an anomalous anticyclonic wind system is found over most of the North American Continent. This is attributed to the dramatically reduced SATs over the Laurentide Ice Sheet. Subsequently, this anomalous wind pattern enhances the westerlies over the mid-latitude North Atlantic Ocean, which anomaly is particularly pronounced in the MIS3 simulation.

### **3.2.2 Sea surface temperature and sea ice**

Consistent with the proxy-reconstructed temperature change, the global mean sea surface temperature (SST) is highest during the Eemian period (Table 3.2), whereas it is comparable

to the PI during the Mid Holocene [North Greenland Ice Core Project Members, 2004]. In the glacial simulations, the global mean SST is decreased by 0.44°C in the MIS3 simulation, and is further reduced by 2°C during the LGM. Figure 3.3 provides a global view of SSTs in the simulations for different climate states. It is shown that high-latitude oceans have an amplification of SST increase during the Eemian interglacial and Mid Holocene, whereas they exhibit further cooling than tropical-subtropical oceans during glacial climates (MIS3 and LGM). Focus on the North Atlantic Ocean, a zoom-in view of the North Atlantic Ocean shows that the difference in SSTs between glacial and interglacial periods are larger than the anomalies between different interglacial climate states (the PI, Mid Holocene and Eemian interglacial) (Figure 3.4).

In Table 3.2, the glacial-interglacial variations of sea ice volume significantly exhibit climate change, and the detailed sea cover are shown in Figure 3.5-3.8. Both summer and winter sea ice edges (the lines of 15% sea ice concentration (SIC)) extend further southward during the LGM (Figure 3.4). Here, it should be noted that the Canadian Archipelago Seas and the Bering Strait have been closed as a result of lower sea level. Consequently, the ocean channels at the Greenland and Scotland Ridge (GSR) are the only ocean connections for ocean water exchange between glacial Arctic Ocean and the rest of global oceans.

Table 3.2 Global mean SST and sea ice volume in each COSMOS simulation.

	Eemian	Mid Holocene	PI	MIS3	LGM
Global SST (°C)	17.34	17.17	17.16	16.72	14.72
North Hemisphere Sea Ice Vol. (km <sup>3</sup> )	8111	14749	24697	44144	56996
South Hemisphere Sea Ice Vol. (km <sup>3</sup> )	9699	11981	13109	22381	24723

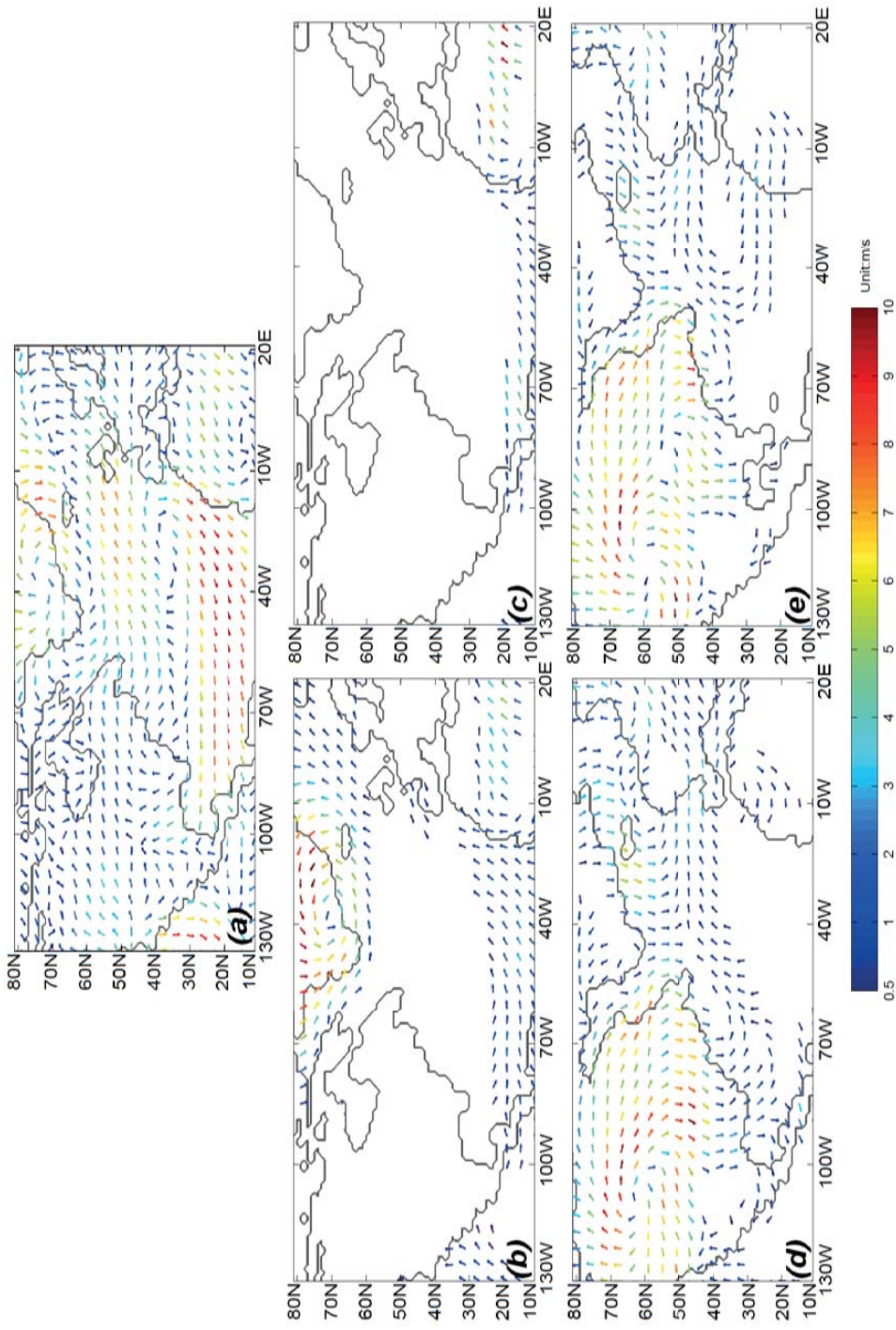


Figure 3.2. COSMOS simulated annual mean surface winds. Panel (a) shows the absolute values of PI surface winds. Subsequently, the anomaly of surface wind field relative to the PI are shown for the experiment of (b) the Eemian (c) Mid Holocene (d) MIS3 and (e) LGM.

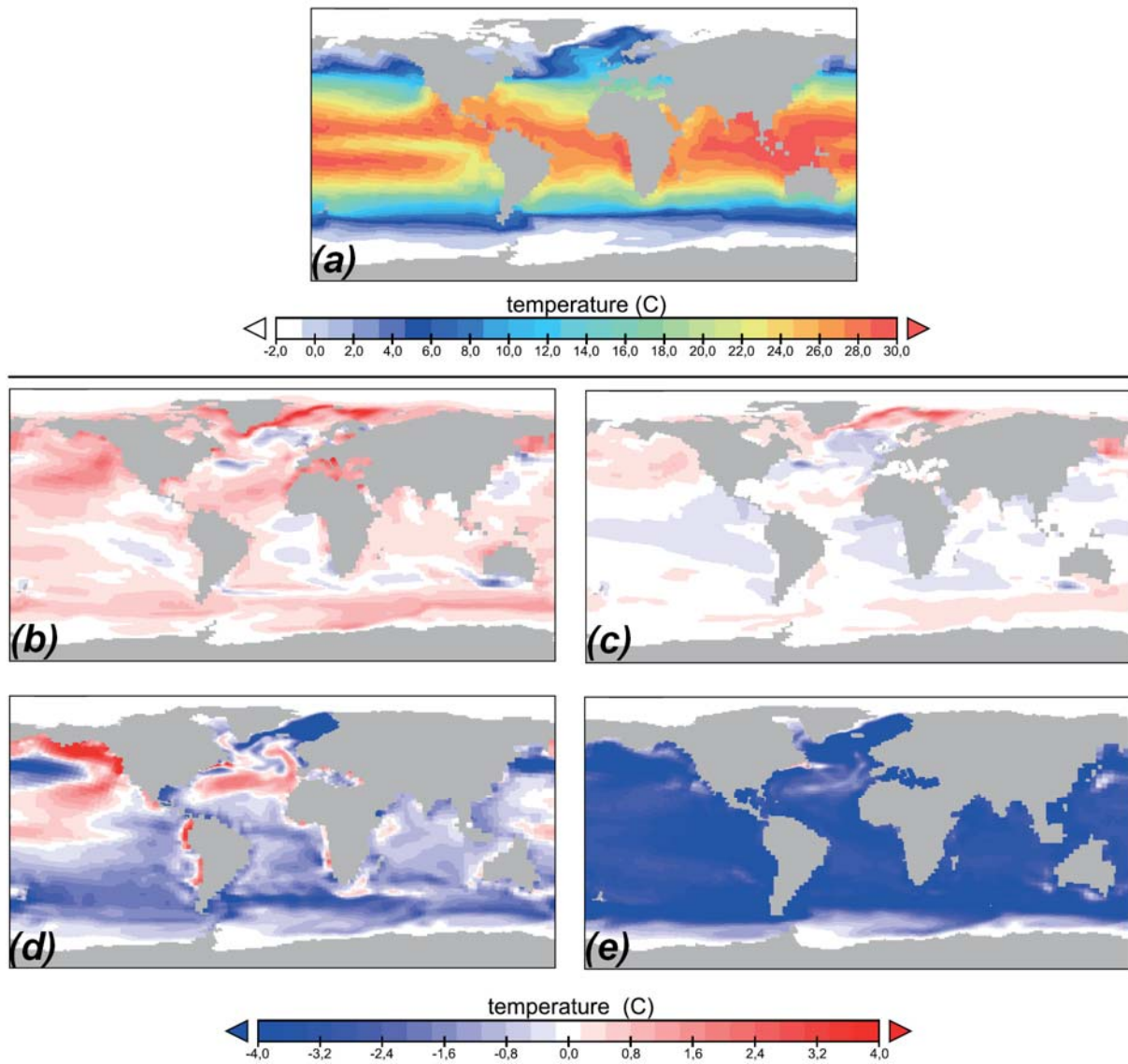


Figure 3.3. COSMOS simulated annual mean SSTs. The PI SSTs are shown in panel (a). Subsequently, the anomaly of SSTs relative to the PI are shown for the experiment of (b) the Eemian (c) Mid Holocene (d) MIS3 and (e) LGM.

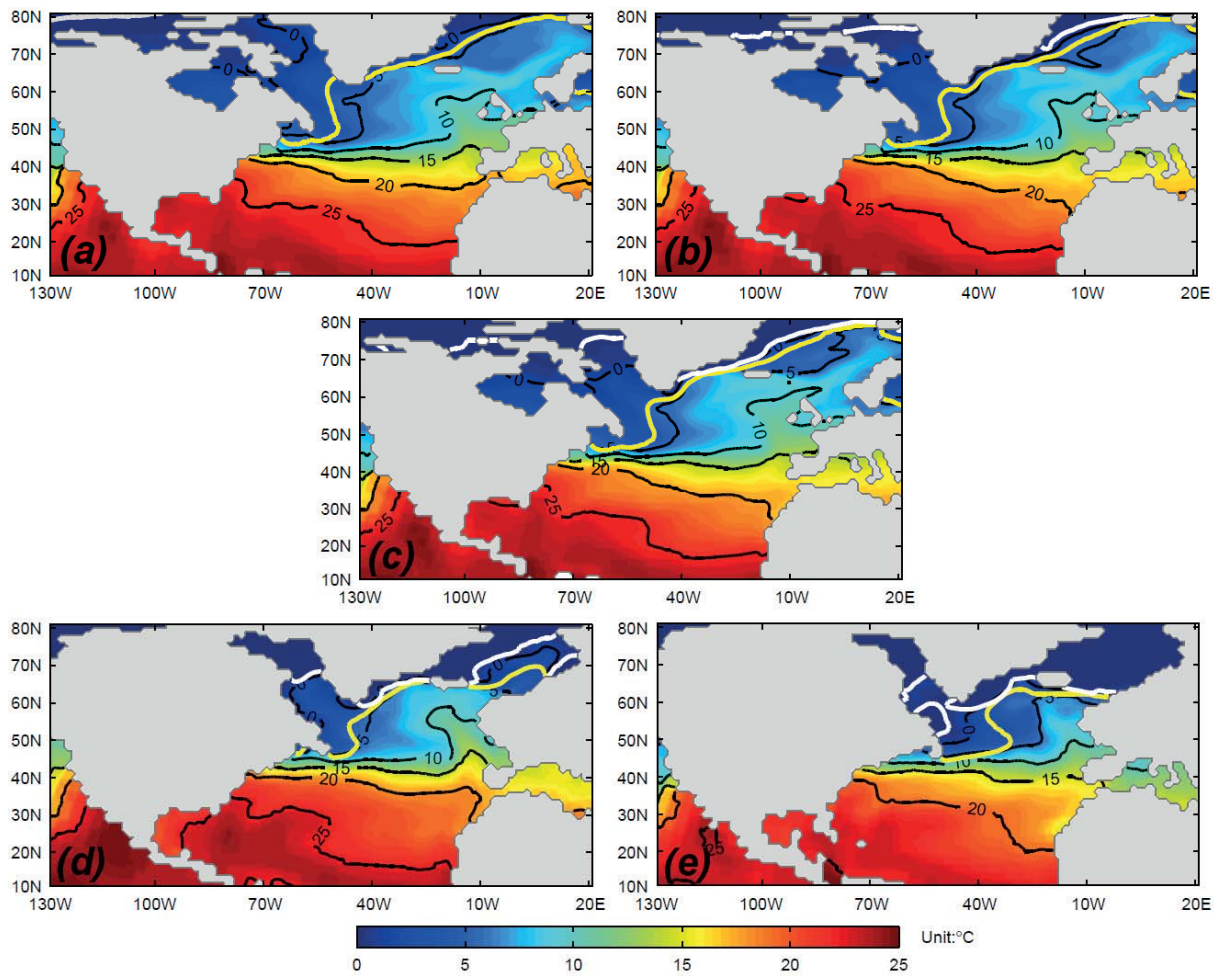


Figure 3.4. An zoom-in view of COSMOS simulated annual mean SSTs and 15% sea ice compactness lines (winter: yellow line, summer: white line) in the North Atlantic Ocean. Panels a-e show the experiments of (a) Eemian (b) Mid Holocene (c) PI (d) MIS3 (e) LGM, respectively.

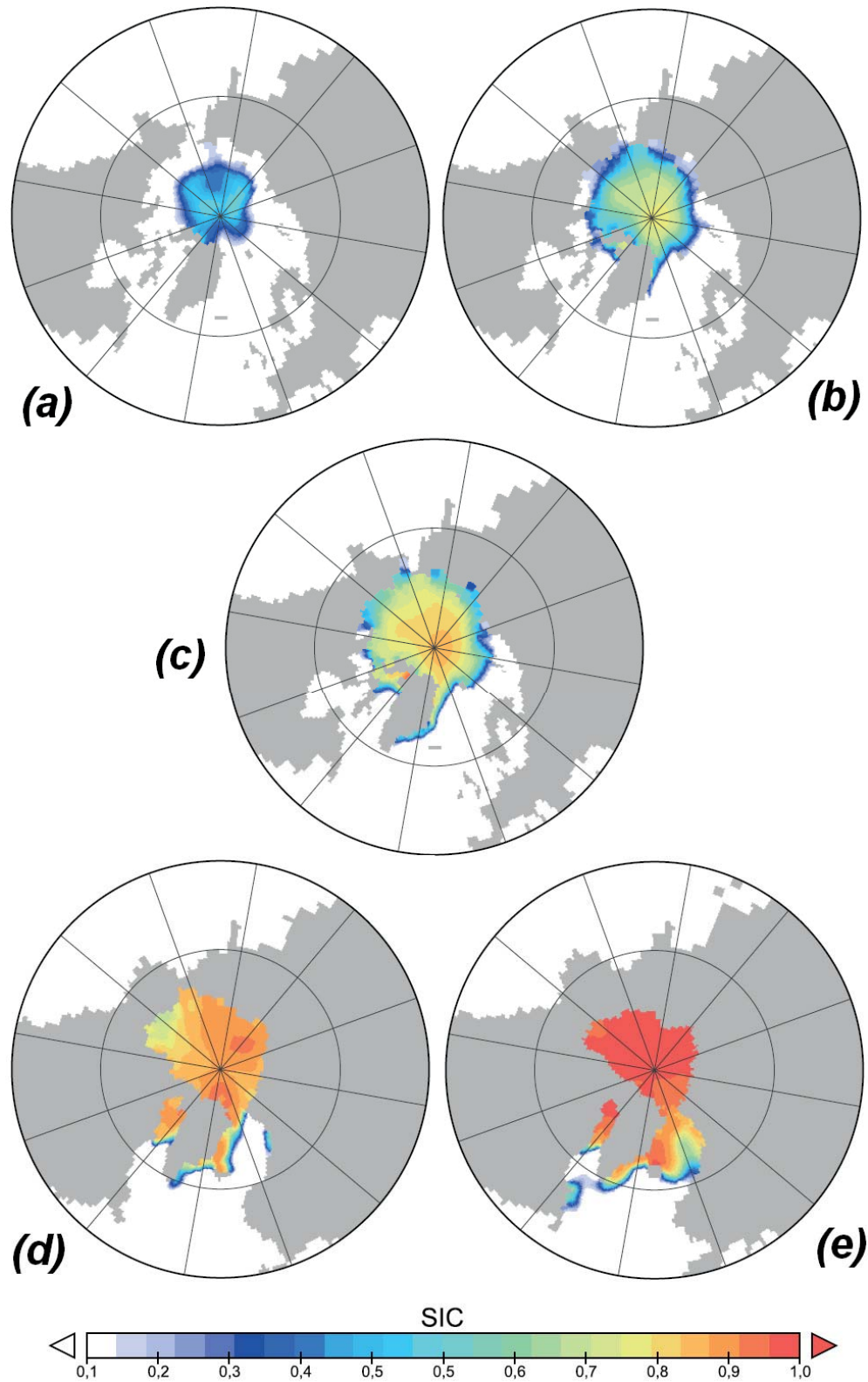


Figure 3.5. Northern hemisphere SIC during boreal summer in the COSMOS simulations of (a) Eemian, (b) Mid Holocene, (c) PI, (d) MIS3 and (e) LGM.

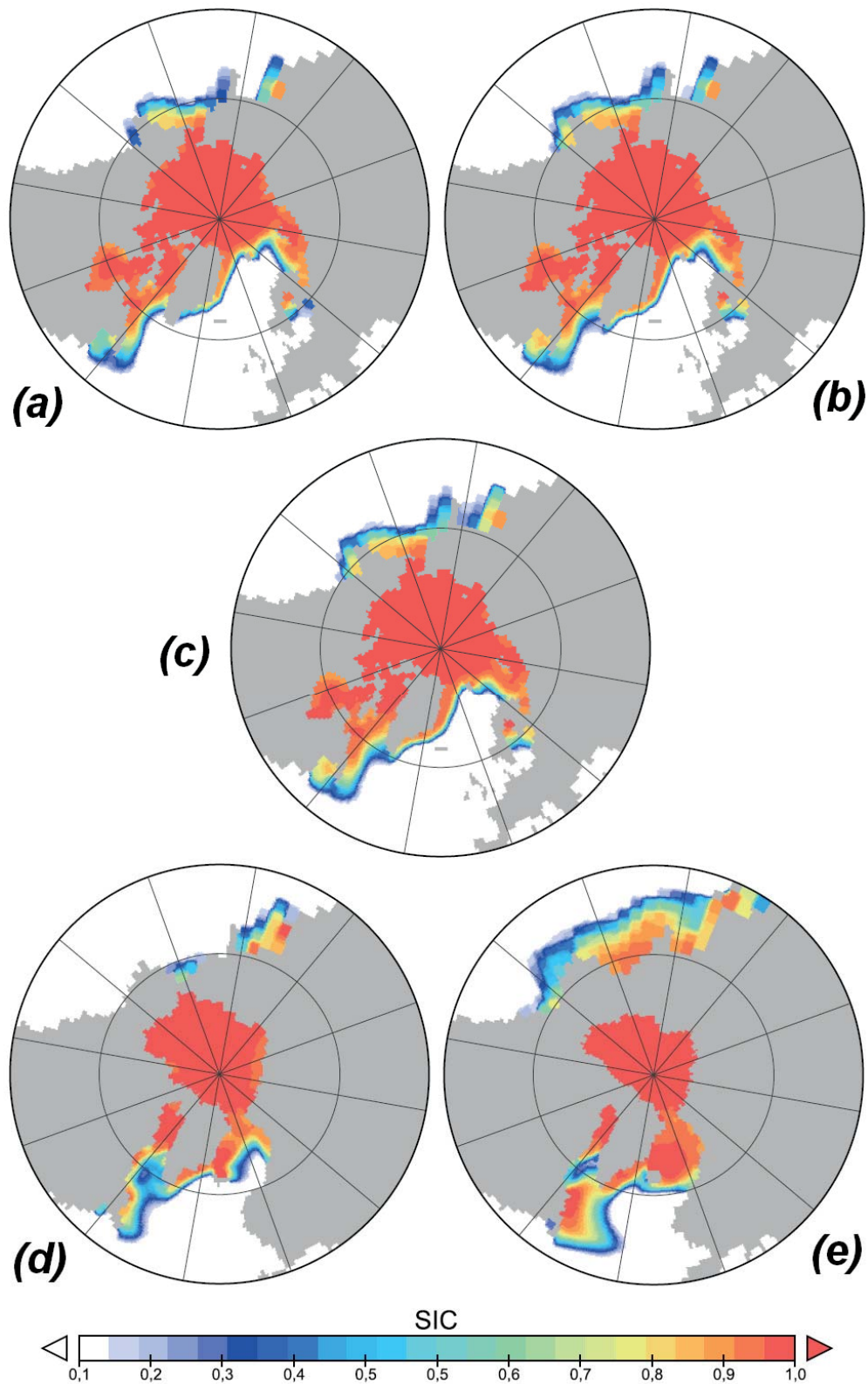


Figure 3.6. Northern hemisphere SIC during boreal winter, shown in the COSMOS simulations of (a) Eemian, (b) Mid Holocene, (c) PI, (d) MIS3 and (e) LGM.

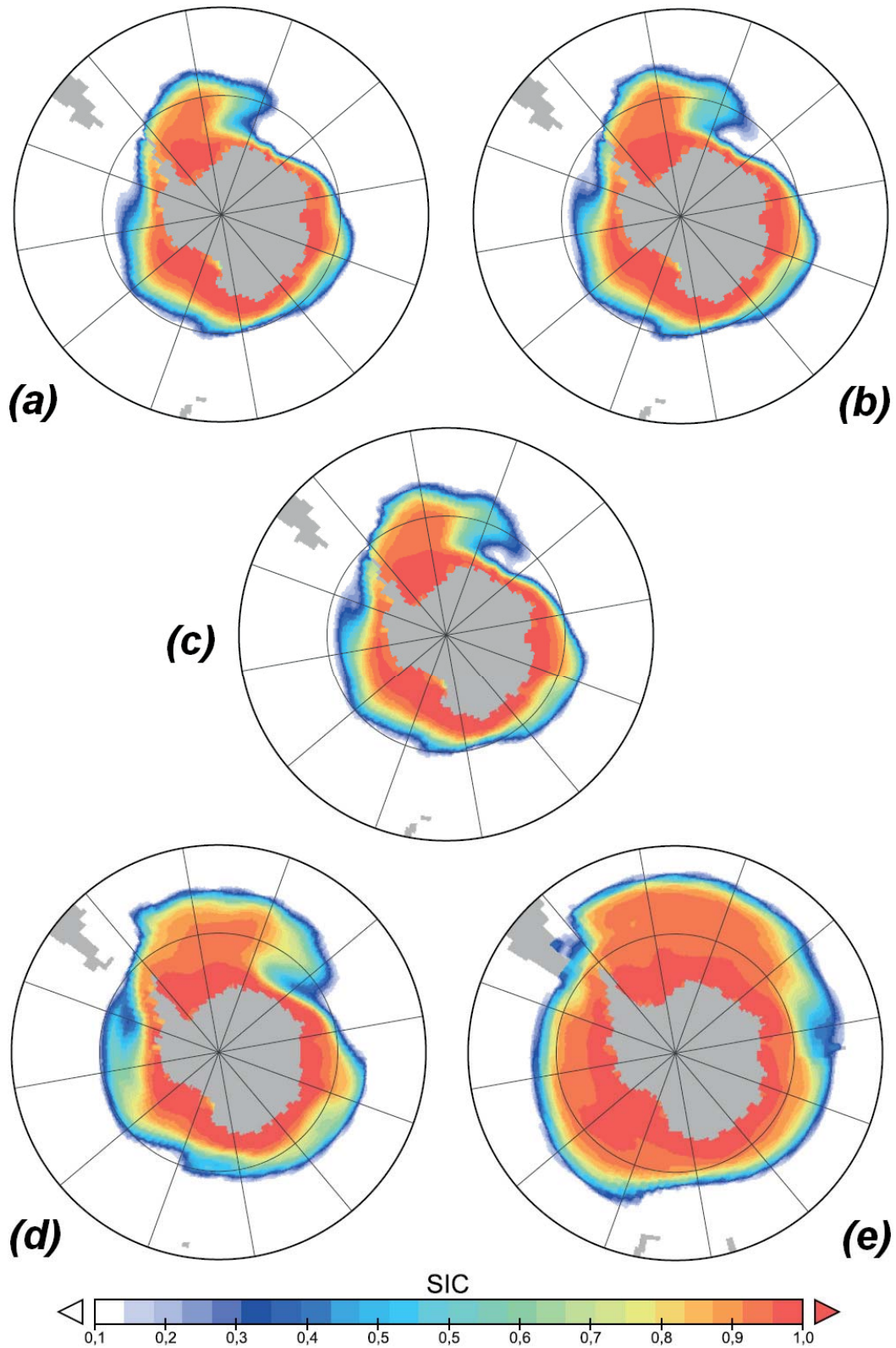


Figure 3.7. Southern hemisphere SIC during boreal summer, shown in the COSMOS simulations of (a) Eemian, (b) Mid Holocene, (c) PI, (d) MIS3 and (e) LGM.

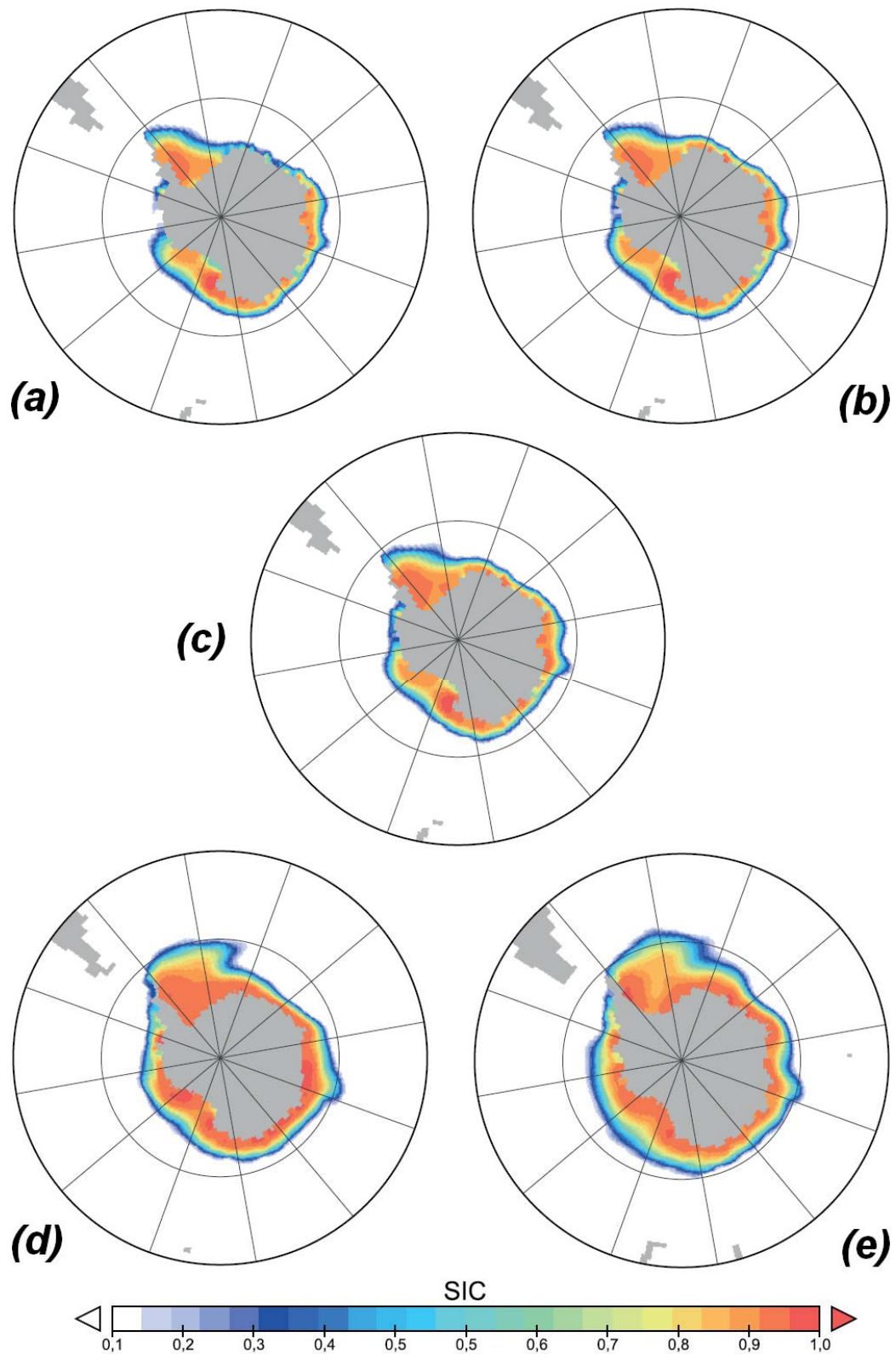


Figure 3.8. Southern hemisphere SIC during boreal winter, shown in the COSMOS simulations of (a) Eemian, (b) Mid Holocene, (c) PI, (d) MIS3 and (e) LGM.

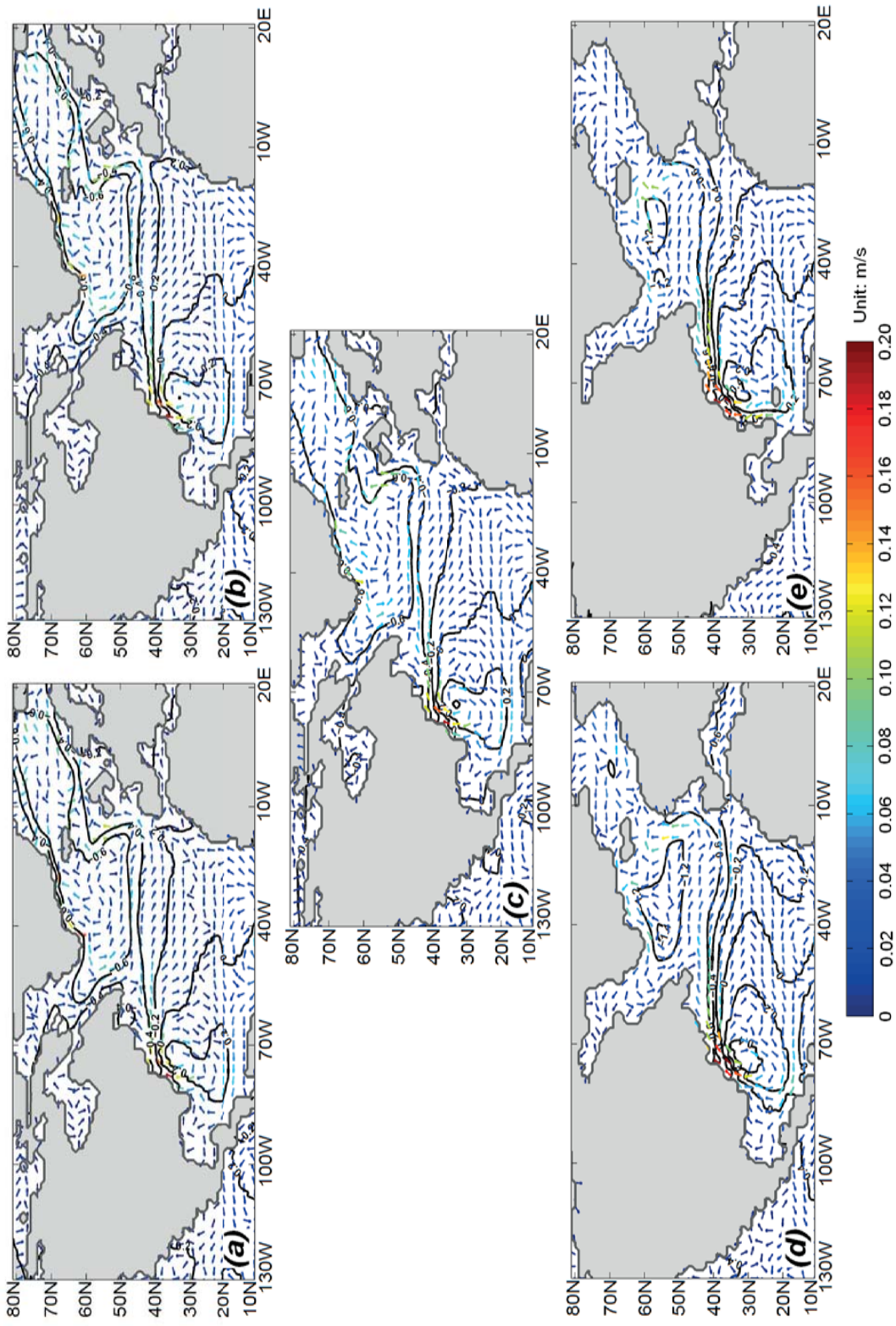


Figure 3.9. Upper 200m-mean ocean circulation (arrows) and SSHs (contour lines) in the COSMOS simulations of (a) Eemian (b) Mid Holocene (c) PI (d) MIS3 (e) LGM.

Table 3.3 Correlation Coefficients between the North Atlantic gyres and wind stress curls. The values in the table are shown in the format of ‘correlation coefficient / the year when the highest correlation occurs’. A negative value means the wind stress curl is leading North Atlantic gyres variation. The calculation of correlation coefficients uses 35 degrees of freedom with 95% confidence in the t-test, the values larger than 0.325 indicate significant correlations.

	Eemian	Mid Holocene	PI	MIS3	LGM
Subtropical WSC & STG	0.3/-1	0.44/-2	0.64/-4	0.43/-2	0.42/-3
Subpolar WSC & SPG	0.35/-2	0.53/-2	0.36/-3	0.54/-2	0.65/-3

### 3.2.3 North Atlantic Ocean surface circulation and AMOC

In the comparison between glacial and interglacial climates, the common features of North Atlantic surface circulation are characterized by the anticyclonic STG centered off the southeast coast North American, and SPG in the region south of Greenland and Iceland (Figure 3.9). The Gulf Stream sits between these two gyres with the maximum ocean current volumetric flow along the eastern coast of North America. However, considerable differences also occur in the North Atlantic Ocean surface circulation among the five climate states, especially between glacial and interglacial periods (Figure 3.9; Figure 3.10). According to the method of Backeberg et al. [2012], the strength of the STG and SPG is indicated by the sea surface height (SSH) at the gyre center (STG: maximum values; SPG: minimum value), which becomes stronger with the global cooling, except during the MIS3 and LGM, i.e. Eemian < Mid Holocene < PI < LGM < MIS3. Subsequently, the variation of sea level anomaly between the subtropical and the subpolar North Atlantic Ocean is also enhanced in the same way (Figure 3.11).

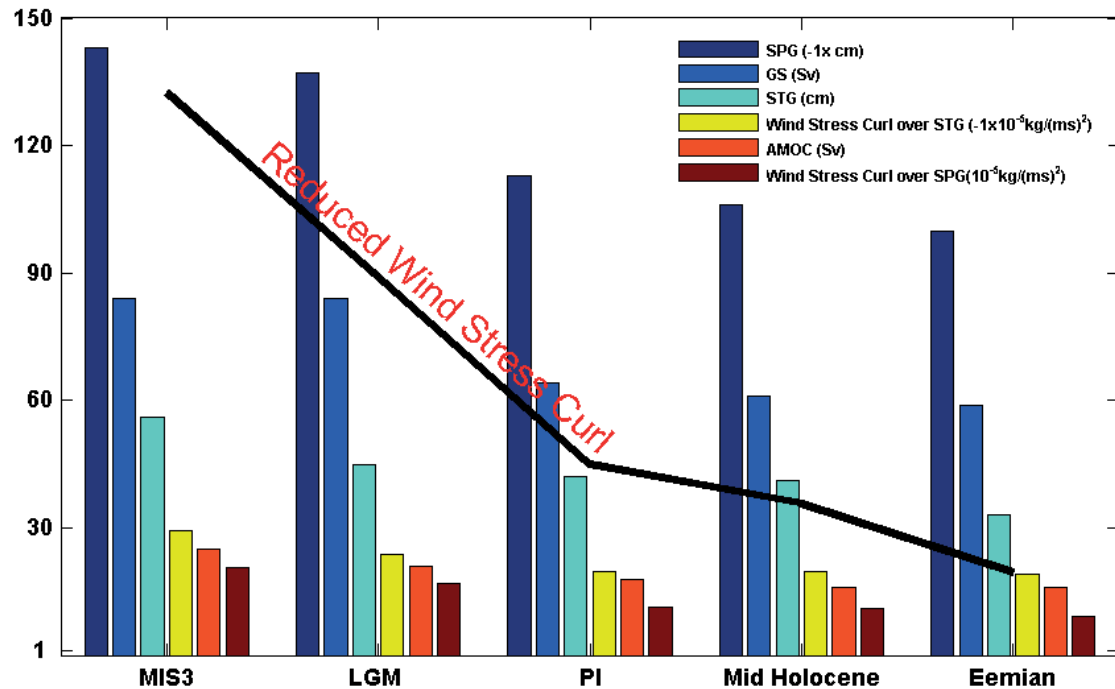


Figure 3.10. The strength of the SPG (dark blue, represented by timing -1of minimum SSH), Gulf Stream (blue), STG (cyan, represented by maximum SSH), wind stress curl over the STG (yellow, represented by timing -1of minimum value), AMOC (orange) and wind stress curl over the SPG (dark red). The regression line (black solid line) exhibits the trend of wind stress curl and the AMOC variation.

The Gulf Stream extends northeastward along the east coast of North America, and in an eastward direction it crosses the North Atlantic Ocean at around  $40^\circ\text{N}$ . At this stage, the water flow separates, with one branch travelling further northwards to form the SPG and the other recycling southwards along with the STG. Here, the strength of the Gulf Stream is identified by the volume of northward water mass transport across  $34^\circ\text{N}$ . Among different interglacial simulations, it becomes slightly weaker in a warmer climate, i.e. the PI (64 Sv) > the Mid Holocene (61 Sv) > the Eemian (58 Sv). In comparison, the Gulf Stream is strongly intensified in our MIS3 (84.7 Sv) and LGM (84.5 Sv) simulations. As shown in Figure 3.12,

the Gulf Stream signal is restricted up to 200 m depth. Furthermore, the position of Gulf Stream is off-shore shifted approximately from 78°W (interglacial) to 75°W (glacial).

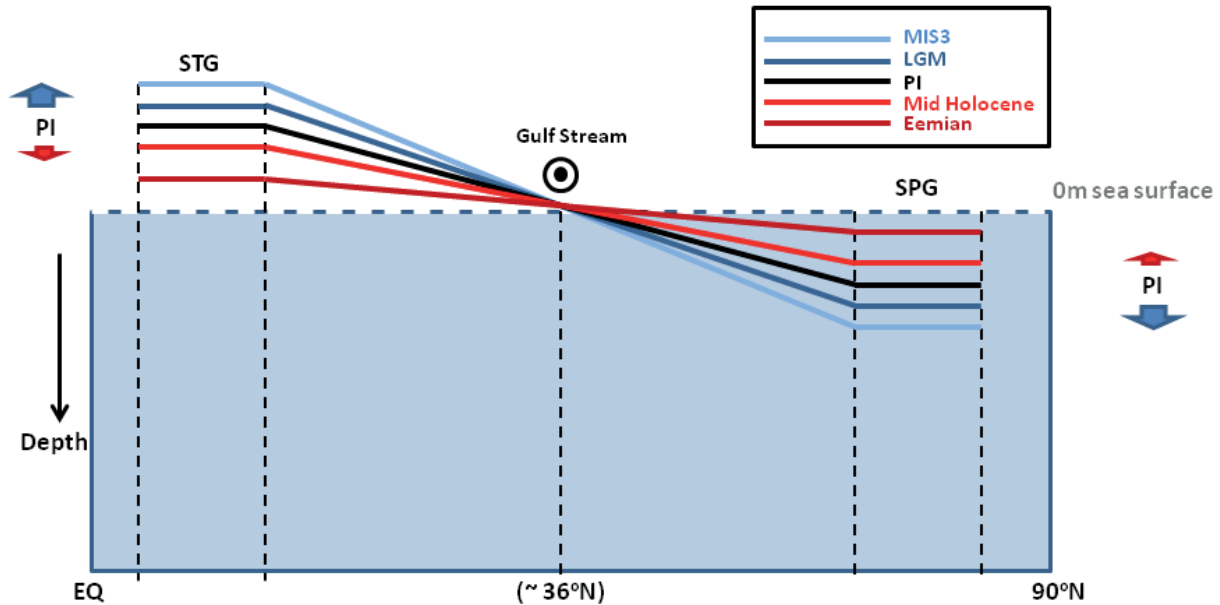


Figure 3.11. Schematic diagram for the SSH variations during different climate states. In accordance with the strength change of wind stress curl and North Atlantic gyres for each climate (Figure 3.10), the meridional sea level anomalies during glacial climate states show larger gradients than the PI and warmer climate, which can favour stronger AMOC

Based on the study of Munk and Palmen [1951], the variability of the STG is r by the wind stress curl with respect to the westerlies and northeastly trades, whereas SPG is determined by the interplay between the westerlies and subpolar easterlies. In Table 3.3, the correlation coefficients of the North Atlantic gyres and corresponding wind stress curl are calculated to clarify their relationship, using the method introduced by Munk and Palmen [1951]. In our calculation, the original model output data for the surface winds and the SSH have been interpolated to a regular  $1^\circ \times 1^\circ$  grid. This leads to the smoothing of extreme values of the

SSH, which are used as the indicator for the strength of the gyres, and inevitably influences the values of correlation coefficients in the Table 3.3.

As shown in Figure 3.10, the strength of AMOC changes in the same way as the North Atlantic gyres and wind stress curl, i.e., MIS3 > LGM > PI > Mid Holocene > Eemian. Here, the strength of the AMOC is defined by the maximum value of the meridional overturning stream function in upper 3000m at 30°N. In comparison, the glacial-interglacial variability is much larger than the anomaly between either different glacial or interglacial climates. Therefore in Figure 3.13 and Figure 3.14, we choose the PI and the LGM as representatives to diagnose the glacial-interglacial variation. It is shown that the AMOC in the LGM simulation is stronger and more variable (Figure 3.13d). Additionally, the glacial STG also shows a larger variability (Figure 3.13a), whereas the SPG becomes relatively more stable compared to the PI (Figure 3.13b), which results from the southward expansion of sea ice into the subpolar North Atlantic Ocean during the LGM (Figure 3.5; Figure 3.6). In Figure 3.13c, the SSH anomaly between the STG and the SPG is used to indicate the variability of North Atlantic gyres, which shows a larger drop in the LGM experiment.

### **3.3 Discussion: distinct features of glacial North Atlantic Ocean circulation from interglacial climate states**

#### **3.3.1 Strengthened glacial North Atlantic gyres due to stronger wind stress**

The SSH features in our PI simulation are quite similar to the reconstruction by satellite altimeter data from 1992 to 2002 [Häkkinen and Rhines, 2004], and comparable to other model simulations [e.g. Treguier et al., 2005]. In the surface North Atlantic Ocean, wind induced Ekman transport forms a mound (in the subtropical North Atlantic Ocean) or a

concavity (in the subpolar North Atlantic Ocean), which is complemented by geostrophic balance and other hydrological processes. The SSH at a gyre core is an indicator of ultimate circulation, and used to represent gyre strength.

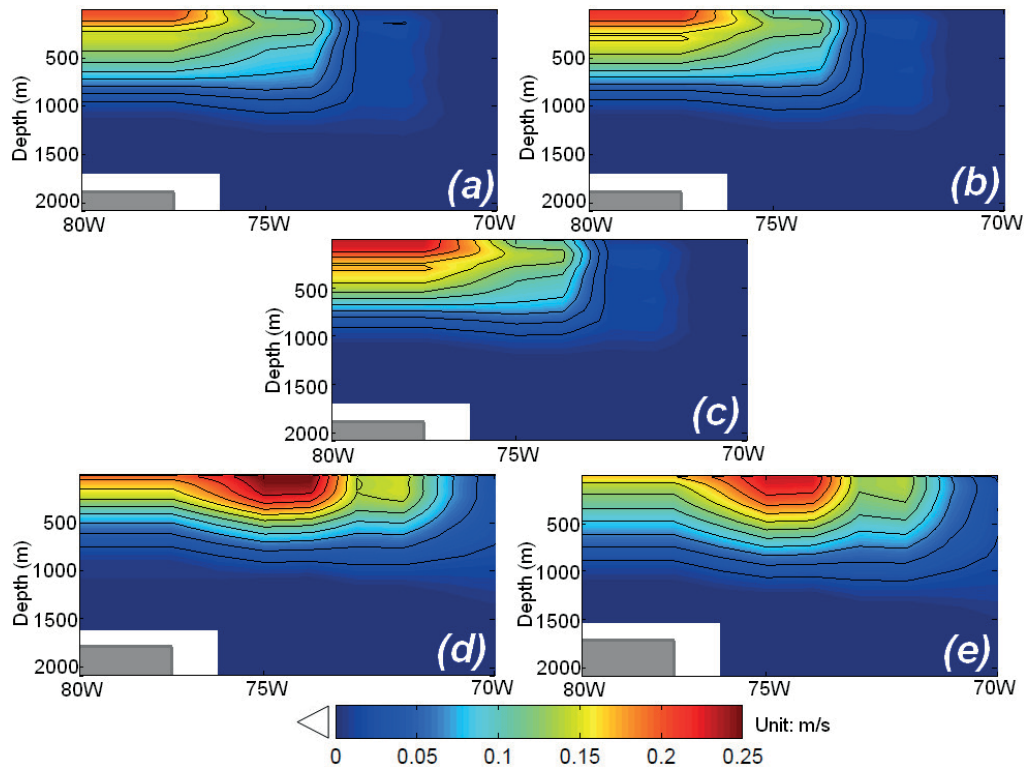


Figure 3.12. Northward velocity of the Gulf Stream at 34°N for the (a) Eemian (b) Mid Holocene (c) PI (d) MIS3 (e) LGM. In contrast to the interglacial (a, b and c), the pathway of the Gulf Stream is offshore shifted (eastwards) during the LGM and MIS3 (d and e).

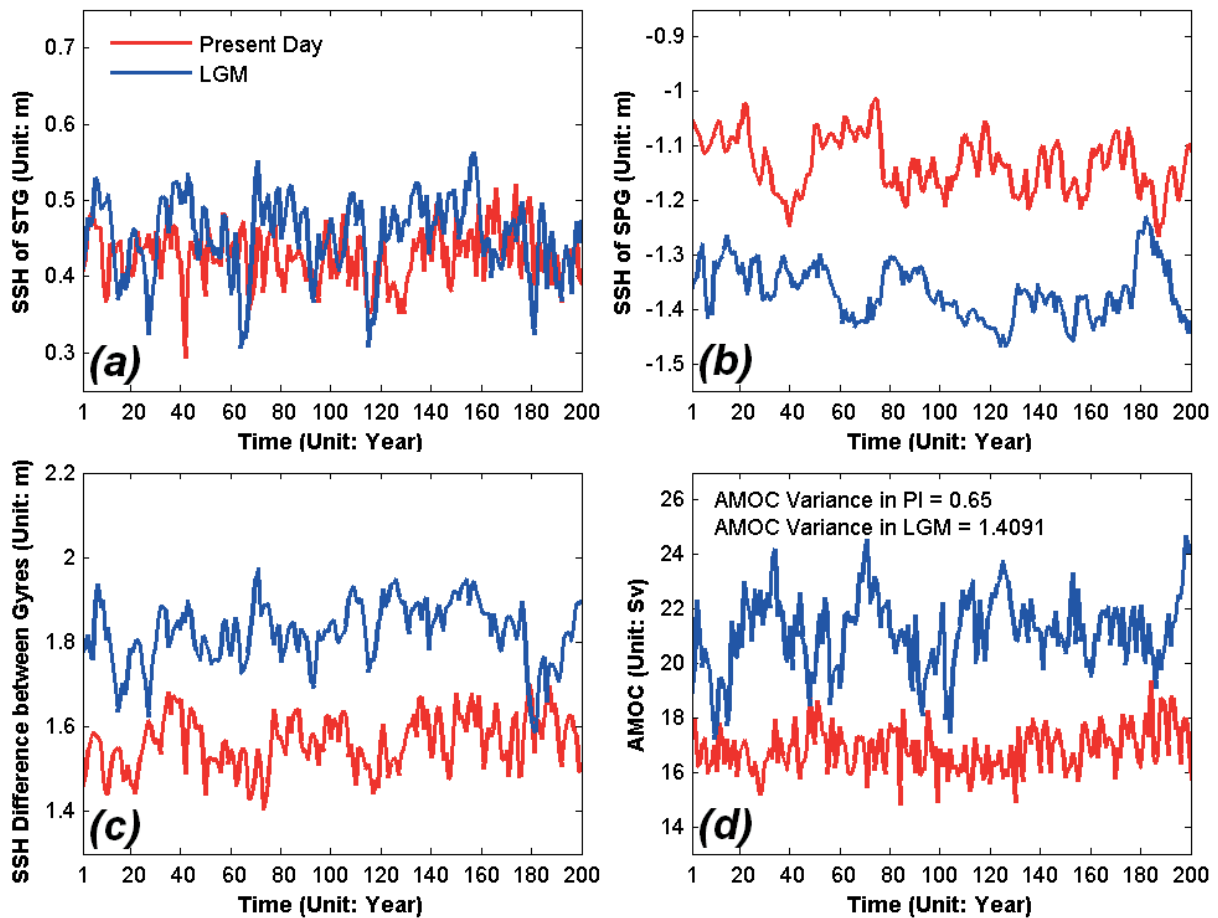


Figure 3.13. Time series of the North Atlantic gyres and AMOC in the PI and LGM simulations: (a) STG, (b) SPG, (c) meridional SSH difference between the STG and SPG, and (d) AMOC strength.

Over the subtropical North Atlantic Ocean, anticyclonic surface winds lead to an increase of sea level, which operates over similar magnitudes among the interglacial simulations (i.e. the PI, Mid Holocene and Eemian interglacial). In comparison, the existence of the Laurentide Ice Sheet results in an stronger anomalous eastward wind at  $30^{\circ}\text{N}$ - $40^{\circ}\text{N}$  over the North Atlantic Ocean during the glacial (Figure 3.1; Figure 3.2), which is mostly attributed to increased elevation and colder SATs [Pausata et al., 2011]. As shown in Figure 3.10, this significantly intensifies the wind stress curl over the subtropical North Atlantic Ocean, and consequently

enhances STG during glacial periods. In addition, a greater altitude drop from the central Laurentide Ice Sheet to the North Atlantic Ocean leads to an even stronger anomalous eastward wind at 30°N-40°N and a subsequent enhanced STG in the MIS3 simulation (Figure 3.1d; Figure 3.2c, d;). Similarly, the strength of our glacial SPG is also strengthened when compared to the interglacial simulations (Figure 3.9; Figure 3.10; Figure 3.11). The cyclonic SPG results from the wind stress curl over subpolar North Atlantic Ocean, which is strongly related to the easterly wind over the area south to Iceland. During glacial periods, a greater sea level pressure gradient from Greenland to Iceland, resulting from a higher Greenland Ice Sheet, significantly enhances surface winds and SPG. Overall, the intensification of North Atlantic gyres during the glacial periods results from the existence of the Laurentide Ice Sheet and elevated Greenland Ice Sheet.

### **3.3.2 Barotropically strengthened glacial Gulf Stream**

The Gulf Stream flows along the eastern North American coastline, and grows stronger as it flows northwards. Up to 1000m depth, it is measured to be 79.5 Sv at 34°N by Hogg and Johns [1995], which is stronger than the value of 64.5 Sv in our PI simulation. However, there is still debate about the strength of North Atlantic western boundary current in the literature [e.g. Curry and McCartney, 2001; Bryden et al., 2005]. According to the currently most complete oceanographic observation data for the Gulf Stream from 1950 to 2004, the variation of the present Gulf Stream is as high as 20 Sv [Dzhiganshin and Polonsky, 2009]. In our Mid Holocene simulation, the hydrography of the Gulf Stream is quite similar to the PI (Figure 3.9), but the strength is slightly reduced by 3 Sv. This is in agreement with the reconstruction from oxygen isotopes, which shows  $4 \pm 2$  Sv less geostrophic transport via the upper 800 m of the Florida Strait during the Mid Holocene [Lynch-Stieglitz et al., 2009]. Lynch-Stieglitz et al. [1999] indicates that the Florida Strait outflow and the Gulf Stream are

weaker during the LGM. In comparison, the water exchange between the Mexican Gulf and the North Atlantic Ocean significantly reduces from 8.9 Sv to 1.93 Sv in our LGM run. However, the strength of the Gulf Stream at 34°N still shows an increase of 20.3 Sv (~31%) relative to that in the PI simulation. This indicates that the strength of the glacial Gulf Stream is not only determined by the outflow from the Mexican Gulf, but also strongly attributed to the driven by STG. As shown in Figure 3.9, the position of the Gulf Stream reveals the maximum meridional SSH gradient, which is larger in the LGM and MIS3 simulations. This indicates a stronger barotropic effect, which can lead to a positive feedback for the strengthening of the glacial Gulf Stream. Another important feature of the glacial Gulf Stream is an offshore shift due to the anomalous eastward wind between 30°N and 40°N, which simply results from the existence of the Laurentide Ice Sheet (Figure 3.2d, e). Consequently, since core sites are mostly located at the PD stream location, proxy data may indicate a reduced Gulf Stream during the LGM. This provides a fundamental difficulty in reconstructing the past Gulf Stream transport at the present-day Gulf Stream position from ocean sediments. As documented in various proxy records, the Gulf Stream shows strong stadial-interstadial variability during the MIS3 [Vautravers et al., 2004]. Our MIS3 simulation is integrated under stadial conditions, and therefore it is limited in detecting this variation. However, our findings provide an opportunity to explain that the stadial-interstadial variation of the Gulf Stream may be linked to a change in surface winds, which are induced by the variation of Laurentide and Greenland ice sheets elevations.

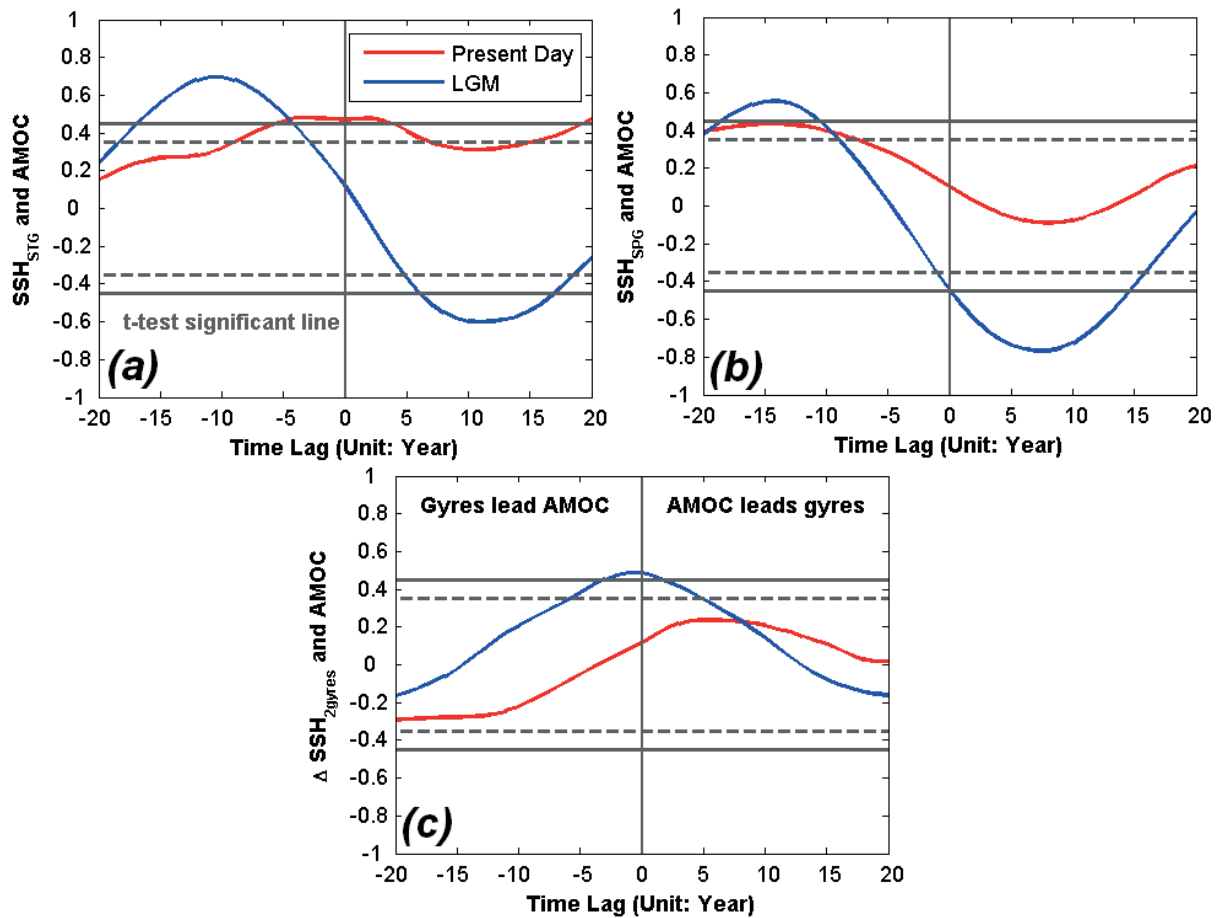


Figure. 3.14 The time-lag correlation coefficients (a) between the STG and the AMOC, (b) between SPG and AMOC, (c) between the SSH difference of two-gyres and AMOC. When assuming 30 degrees of freedom with 95% (dashed gray line) and 99% (solid gray line) confidences in the t-test, the values outside gray lines indicate significant correlations. A negative time lag means North Atlantic gyres lead AMOC variation, and a positive correlation coefficient indicates that the feedback of the AMOC to gyres variation is positive.

### 3.3.3 Stronger glacial AMOC associated with intensified North Atlantic gyres

Throughout our simulations, the strength of the glacial AMOC is exhibited as being stronger than that during the interglacial. More precisely, the AMOC changes in accordance with glacial-interglacial variation of North Atlantic gyres. As shown in Figure 3.10, SPG and STG are intensified simultaneously, leading to a larger sea level drop from the subtropical to the subpolar North Atlantic Ocean. This can potentially induce a northward surface flow, which acts in the same direction as the AMOC surface branch (Figure 3.11). In Figure 3.14a, the correlation between the time series of STG and AMOC is significant in the PI simulation, whereas it is even higher in our LGM run. This suggests that the variability of the STG has a larger impact on the AMOC during glacial climates. Similarly, the correlation between the glacial SPG and AMOC is also enhanced (Figure 3.14b). It is worth noticed that, for a better comparison with other climate simulations, the LGM simulation used in this study is initialized from the PD ocean state. In the study of Zhang et al. [2012], another simulation for the LGM is conducted, which has the same experimental setup in COSMOS, but initialized from a well-stratified and cold ocean. This initial condition results in a weaker AMOC state, but the analysis in their experiment is still in line with the conclusions addressed in this study due to the similar surface properties between these two LGM states. Overall, our results indicate that the intensified North Atlantic gyres during the glacial periods act in a positive feedback enhancing AMOC. Since paleoceanographic data seems to be more consistent with a shallower state of AMOC (e.g. Hesse et al. [2011]), so a weakening mechanism for the AMOC might be missing in our model set up (e.g. stratified initial state, hydrological balance and etc.). However, it is beyond the scope of this scientific topic. Hofmann and Ramstorf [2009] illustrates that stronger surface winds can intensify the variability of surface ocean

gyres. In comparison, our research obtains similar results for STG in the North Atlantic Ocean, whereas a stronger sea ice export from polar region can significantly reduce the variability of SPG during glacial periods. Montoya and Levermann [2008] finds that the wind-driven gyre circulation can be a threshold in determining AMOC, by changing the locations of deep-water formation. Throughout analyzing North Atlantic gyres, we find that the variation of meridional sea level height induced by changing the North Atlantic gyres can also play a role in affecting the strength of AMOC.

### **3.4 Discussion: the effect of elevated North-hemisphere ice sheet to the surface North Atlantic Ocean circulation during the glacial climate periods**

We analyze the glacial and interglacial variations of the North Atlantic gyres, Gulf Stream and AMOC. Our main findings are: (i) Compared to the interglacial, surface winds over the North Atlantic Ocean are enhanced due to the existence of the Laurentide Ice Sheet and higher elevation of Greenland Ice Sheet during glacial climates. (ii) Glacial North Atlantic gyres are intensified in response to stronger surface winds. (iii) Larger SSH anomaly between the subtropical and the subpolar North Atlantic Ocean barotropically intensifies the strength of the Gulf Stream during the glacial periods. Between 30°N and 40°N, the Gulf Stream pathway is shifted offshore due to an anomalous eastward wind over the North Atlantic Ocean. (iv) By enhancing the North Atlantic gyres and corresponding meridional SSH gradient, surface winds act as a positive feedback in strengthening AMOC during glacial periods.

Our LGM experiment is based on PMIP3 ice sheets, whereas the MIS3 experiment uses reconstructed ice sheets in ICE5G, which is not provided by PMIP3. In comparison, the ICE5G Laurentide Ice Sheet during LGM has a higher altitude, which can lead to a stronger

anomalous eastward wind across the North Atlantic Ocean, and further intensify the North Atlantic gyres. This is in line with our mechanism study in this paper. Here, we propose the mechanism of ‘higher ice sheets - stronger surface winds – intensified North Atlantic gyres’ during the last glacial-interglacial cycle, and do not aim to reconstruct the MIS3 and LGM circulation regimes. Furthermore, using ocean sediment records, Lynch-Stieglitz et al. [1999] reconstruct a weaker Gulf Stream during the LGM, in contrary to that in our LGM simulation. Based on our findings, these two results can be reconciled with respect to the offshore shift of the Gulf Stream pathway during the LGM. In addition to surface winds, SSH is affected by internal dynamics within the ocean, which can also influence North Atlantic gyres and AMOC variation. Further work can be conducted in this direction, but there are difficulties in determining a reference depth to calculate hydrological height in the North Atlantic Ocean.

## **4 Dependence of abrupt Atlantic meridional ocean circulation changes on climatic states**

The last glacial-interglacial cycle, from ~120 ka B.P. to the Holocene epoch (since ~10 ka B.P.), is punctuated by several abrupt climate changes [e.g. North Greenland Ice Core Project Members, 2004], which can occur within a few decades [Dansgaard et al., 1993]. The magnitude of these climate changes are stronger between 25 and 70 ka B.P., and less pronounced during maximum glacial conditions around the LGM. Furthermore, proxy evidence from North Atlantic deep-sea sediments demonstrates a suppression of abrupt climate changes during the Holocene [e.g. Zhao et al., 1995]. Overall, these proxy records suggest that the signature of abrupt climate changes are non-uniform during different climate states throughout the last glacial-interglacial cycle. Furthermore, records of sedimentary nutrient proxy evidence and kinematic proxies indicate a notable correlation of abrupt climate changes and variations in AMOC [e.g. McManus et al., 2004; Thornalley et al., 2011]. In the so-called ‘water hosing’ experiments in numerical models, freshwater fluxes to the North Atlantic surface ocean have shown to be a potential key factor to modulate the strength and stability of the AMOC in regional and global climate change scenarios [Ganopolski and Rahmstorf, 2011]. Therefore, AMOC changes by applying freshwater perturbation have been used to induce abrupt climate changes [e.g. Rahmstorf, 1996; Prange et al., 2004; Liu et al., 2009].

Models of different complexity commonly show that the mechanism for the AMOC reduction is strongly related to a surface freshening at deep-water formation sites in the North Atlantic Ocean. However the underlying physical processes for an AMOC recovery after the end of

the freshwater perturbation are potentially more diverse. For instance, Hu et al. [2008] and Renold et al. [2010] reveal a gradual and two-phase recovery of the AMOC during the present and the LGM, and they emphasize the roles of the Bering Strait and Nordic Seas on these AMOC variations, respectively. Prange et al. [2004] performed freshwater hosing experiments with a model of intermediate complexity for different glacial background states and found a two-step relaxation for background conditions with convection sites in the South Labrador Sea and the Nordic Seas, and a slower response for an AMOC background state without convection in the Nordic Seas. By changing freshening locations and magnitudes, Otto-Bliesner and Brady [2010] identified different recovery characteristics of the AMOC within hundreds of years after removing the freshwater perturbation. Their results also present the importance of southward expansion of polar sea ice, which can lead to an increase of colder and fresher water export into the high-latitudes North Atlantic Ocean, accompanied by a meridional shift of the Intertropical Convergence Zone. Furthermore, it has been suggested that variations in the location of the freshwater perturbation in the high-latitudes North Atlantic Ocean can induce distinctively enhanced northward transports of warm, saline, subsurface water into the South Labrador Sea and the Nordic Seas, which subsequently lead to distinct reductions of deep-water formation despite a similar overall AMOC slowdown [Kleinen et al., 2009]. Moreover, the AMOC stability behavior and sensitivity to freshwater perturbations has been shown to be dependent on the background climate condition. (e.g. Prange et al., 2004; Knorr and Lohmann, 2007)

Here, we aim to investigate the underlying dynamics for the resumption process and overshoot phenomenon of the AMOC recovery, which may have operated differently during various stages of the last glacial-interglacial cycle. Therefore, we conduct hosing experiments for the three different climate states and examine the subsequent changes of the convective

process in the South Labrador Sea and the Nordic Seas, as well as their interplay with hydrographic changes in the low-latitudes Atlantic Ocean. Special emphasis is given to the North Atlantic spatio-temporal changes of the overall AMOC recovery characteristics among three different climate states.

## 4.1 Design of hosing experiments

We employ the Community Earth System Model (COSMOS), which has been applied and tested for the Cenozoic climate [Knorr et al., 2011; Stepanek and Lohmann, 2012], glacial [Zhang et al., 2012] and interglacial climate states [Wei et al., 2012; Wei and Lohmann, 2012]. Before conducting abrupt climate changes experiments, the climates for the PI, LGM and 32 ka B.P. have been run for over 2000 years to reach their respective quasi-equilibrium states. Here, the values of orbital parameter and greenhouse gas concentration are equally used as the experiments of PI, LGM and MIS3 in Chapter 3 (please see Table. 3.1), as well as their land-sea masks and paleo river run-off routes.

When performing the freshwater perturbation experiments, a freshwater flux of 0.2 Sv (1 Sv = 106 m<sup>3</sup>/s) is added to the Ice-Rafted Debris belt in the North Atlantic Ocean, around 40°N-55°N in the central Atlantic Ocean [Zhao et al., 1995; Hemming, 2004]. The forcing lasts for 150 years, after which an additional 300 years are utilized for recovery, i.e. without freshwater perturbation.

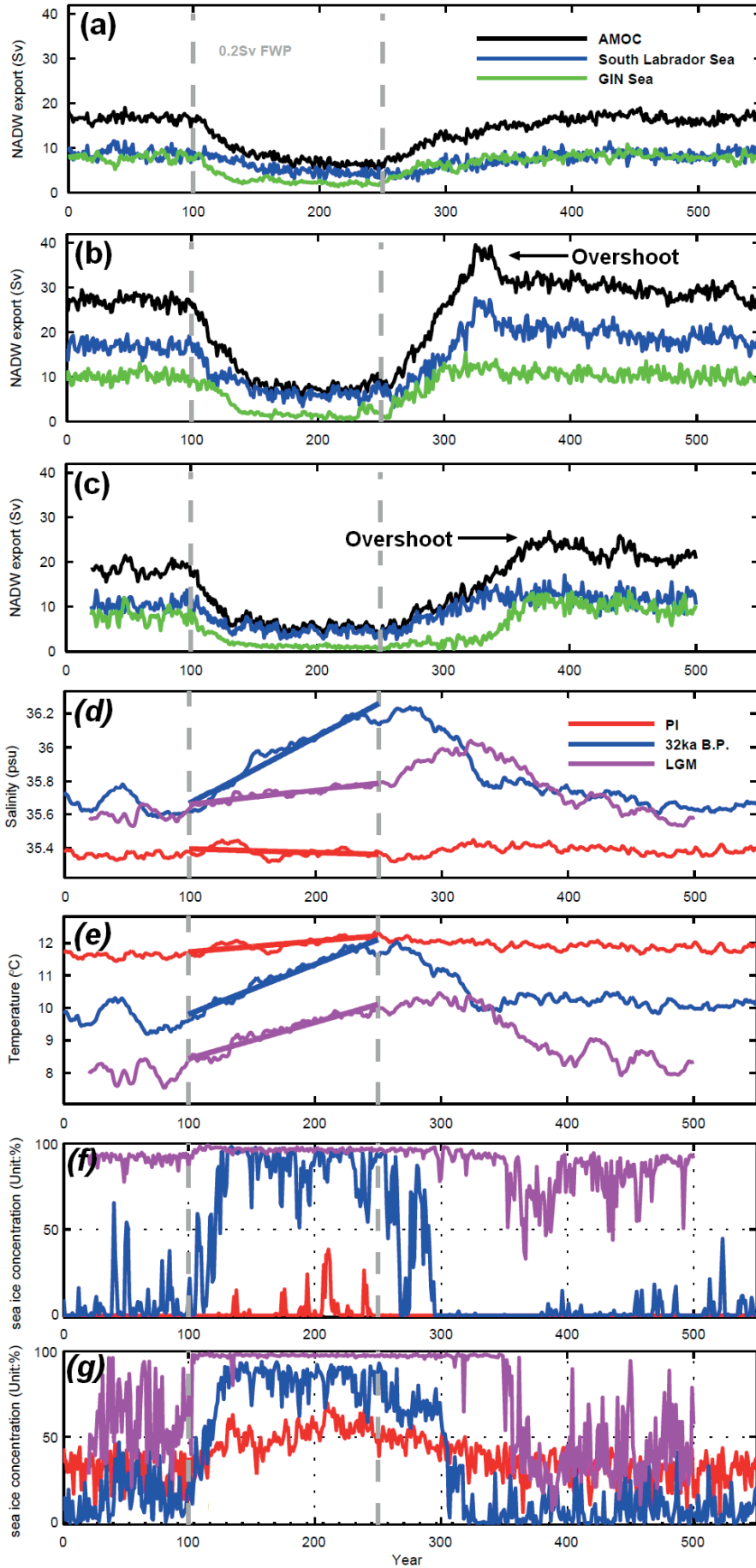


Figure 4.1. Time series of the strength of the AMOC and deep-water formation in the South Labrador Sea and the Nordic Seas for (a) PI, (b) 32ka B.P. and (c) LGM. Here, the intensity of the AMOC is presented by the maximum value of the meridional overturning stream function in upper 3000m at 30°N. The dashed grey lines indicate the time period (between 100 and 250 years) when the fresh water perturbation is applied. (d) Salinity and (e) temperature averaged over the tropical Atlantic Ocean (20°S-30°N) at the depth of 500m is shown for the 500 years of each model run. Over the curves for salinity and temperature, the linear fitting lines illustrate different increase rates of temperature and salinity. The time series of the SIC in (f) the Nordic Seas and (g) the South Labrador Sea are exhibited, respectively.

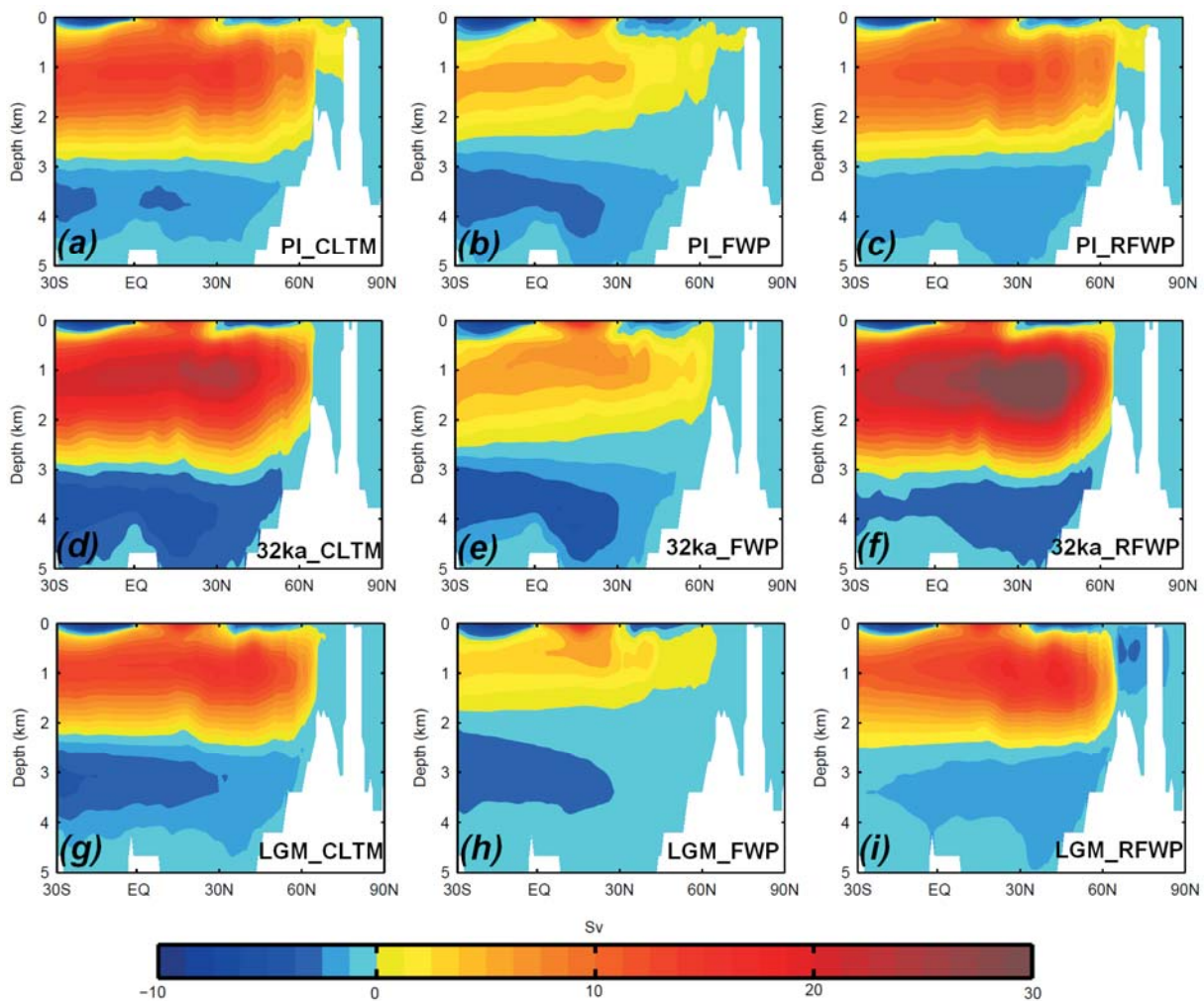


Figure 4.2. Temporal changes of the Atlantic Meridional Overturning Circulation (AMOC) in each hosing experiment. The state before applying fresh water forcing is named by the ‘CLTM’ (i.e. climatology mean), and the ‘FWP’ (i.e. fresh water perturbation) stands for the mean state of the last 10 years of freshening. Then, the ‘RFPW’ (i.e. recovered from fresh water perturbation) is used to present the state with an AMOC overshoot during the LGM and 32ka B.P., or the mean state between 380 and 400 year during the PI, when the AMOC has completely recovered.

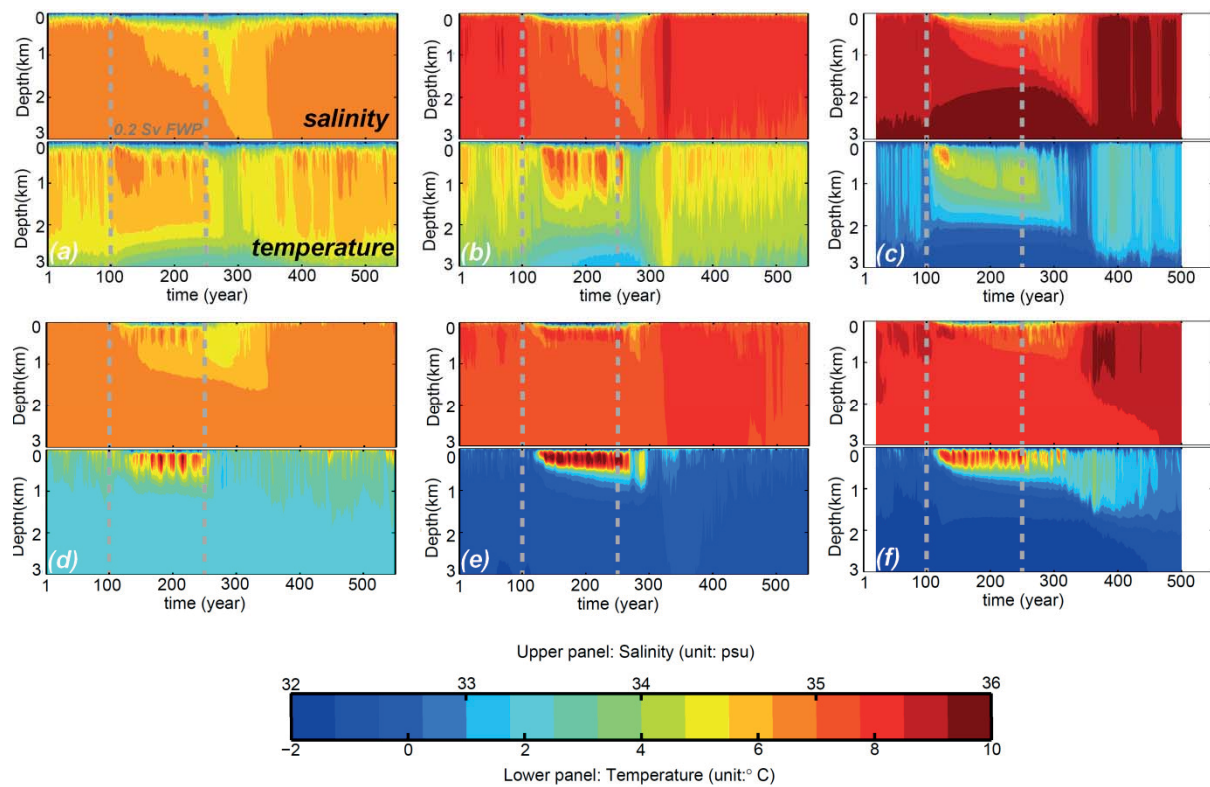


Figure 4.3. Time evolving of the vertical structure of the salinity (upper panel) and temperature (lower panel) in the South Labrador Sea are exhibited for the experiment of (a) the PI, (b) 32ka B.P. and (c) LGM, respectively. The Nordic Seas is shown in the lower row for comparison (panels d, e and f).

## 4.2 Results: distinct recovery features of AMOC on different climate states

The three hosing experiments show a similar AMOC reduction at the end of the 150-year fresh water perturbation (Figure 4.1), which temporal changes of the AMOC in the experiments for each climate state are shown in Figure 4.2. Interestingly, the following recovery stages exhibit a clear dependence on the climate background states. The most prominent differences are the overshoots characteristics during the recovery. In the following, we will subdivide the underlying dynamics of the overall recovery into two stages: one directly following the end of the freshwater perturbation that describes the initial resumption, and a superposed phase that coincides with the AMOC overshoot dynamics.

### 4.2.1 Initial resumption of the AMOC

At the end of the 150-year freshwater perturbation, the AMOC is suppressed to a comparable strength of  $\sim 5$  Sv in all the three climate states (Figure 4.1a-c). Correspondingly, the deep-water formation in the South Labrador Sea and the Nordic Seas decrease substantially. Here, deep-water formation in the Nordic Seas is defined as the vertical maximum value of stream function at the south edge of the Nordic Seas ( $62^\circ\text{N}$ ), and the deep-water formation in Labrador Sea is defined as the difference of AMOC strength and deep-water formation rate in the Nordic Seas. This method for calculation of deep-water formation has been well-explained and used by Cheng et al. [2011] (Figure 4.1a-c).

In experiment PI, the deep-water formation in the South Labrador Sea reaches a minimum ( $\sim 5$  Sv) between 140 and 150 model years, whereas it is  $\sim 2$  Sv in the Nordic Seas. After the end of the freshwater perturbation, the increase of the AMOC occurs with an instant resumption of deep-water formation in both areas. About 110 years later (i.e. after  $\sim 260$  model years), the deep-water formation and the AMOC have recovered to their starting levels prior to the

freshwater perturbation (Figure 4.1a). This result is comparable to the work of Mignot et al. [2007], who designed a similar experiment, using a negative anomalous salt flux corresponding to 0.35 Sv for 100 years between 50°N and 80°N. In the 32ka B.P. and LGM experiments, the deep-water formation in the South Labrador Sea reduces to 4-7 Sv (Figure 4.1b, c). However, in the Nordic Seas, it is quasi-terminated after 250 model years in the 32ka B.P. experiment, and a shutdown of deep-water formation is diagnosed in our LGM run (Figure 4.1b and c). Subsequently, an instant restart of deep-water formation in the South Labrador Sea is triggered, whereas the restart in the Nordic Seas occurs 30 years later. So, the initial resumption of the AMOC recovery in the LGM simulation is triggered in the South Labrador Sea. The underlying physical process is related to a modified salinity stratification and temperature inversion between the surface and intermediate layers that quickly build up during the freshwater perturbation. The most significant temperature and salinity anomalies are found in the intermediate layer during the 32ka (Figure 4.3). After deactivating the freshwater forcing, an instant collapse of water mass stratification is detected with respect to both the salinity stratification and the temperature inversion (Figure 4.3). The most rapid recovery of convective processes occurs in the 32ka B.P. experiment, which also highlights the role of hydrostatical anomalies once the freshwater forcing is removed. The salinity changes associated with the surface freshening is detected down to 3000m depth in the South Labrador Sea. However, it is limited within the upper 1000m in the Nordic Seas. Similarly, the salinity anomaly in the Nordic Seas is emphasized mostly in the 32 ka B.P. experiment, which also shows the quickest collapse of the salinity stratification and the temperature inversion after 250 model years.

In Figure 4.1f and g, sea ice cover shows an instant decrease after the end of freshwater perturbation, and reaches a minimum accompanying with the occurrence of the AMOC

overshoot. During this process, fresh water due to sea ice melting increases salinity stratification, and counteracts the convective process. In the 32ka B.P. experiment, the area of deep-water formation becomes free of sea ice during the AMOC overshoot. However, a rapid rebuild-up of sea ice results from cold surface air temperature during the LGM.

### **4.2.2 The AMOC overshoot**

So far we have shown that the initial resumption of the AMOC is strongly dependent on the background climate conditions. In the following we will investigate the role of these conditions for the superposed overshoot characteristics during the overall AMOC recovery. Between 320 and 340 model years, the AMOC strength is 12 Sv in the 32ka B.P. experiment, which is characterized by a water mass with high temperature and high salinity (HTHS) at the intermediate depth in the South Labrador Sea (Figure 4.1b; Figure 4.3b). Approximately five decades later, these water property anomalies and the corresponding AMOC overshoot (~5 Sv) are detected in the LGM experiment, but they are completely absent in the PI experiment. According to previous studies, these decadal-scaled AMOC variations are in agreement with the effect of water mass advection from the tropical Atlantic after a slowdown of AMOC [Stommel, 1961; Bryan, 1986].

As shown in Figure 4.1d, e, the increase of salinity and temperature during the freshwater perturbation occurs with different rates as indicated by the field-mean values for intermediate-layer water of the tropical Atlantic Ocean. These changes are negligible in the PI simulation, and stronger in the LGM simulation with the largest changes in the 32ka B.P. simulation by showing an increase of 0.6 psu and 2.1°C. The variation of water properties in the tropical Atlantic Ocean accompanying the suppression of the AMOC agrees with proxy records and modelling results by Rühlemann et al. [2004], which demonstrate an intense warming of intermediate depth waters in the tropical North Atlantic Ocean (Figure 4.4). In

accompany, the salinity is also intensified, due to the slowdown of transporting tropical salty water into higher-latitude North Atlantic Ocean (Figure 4.5). In consequence, the slowdown of the AMOC results in a suppressed northward heat transport. This leads to a tropical warming (Figure 4.1e), which is most pronounced in the 32ka B.P. experiment in accordance with the largest reduction of the AMOC. After the end of freshwater perturbation, salinity and temperature reaches the level of the first 100 years within a few decades. This indicates that the anomalies in the intermediate layer of tropical Atlantic Ocean are linked to the freshwater perturbation in the North Atlantic. Overall, a stronger anomaly of water properties in the tropical Atlantic Ocean also favours a larger AMOC overshoot.

In the comparison between the states during the suppressed AMOC and AMOC overshoot, the water mass change of the ocean north of 45°N exhibit reversed changes to the tropical Atlantic. The HTHS water is transported from the tropical Atlantic Ocean into the South Labrador Sea (Figure 4.6). Similar to the differences in the AMOC overshoot strength, the anomalous sea surface temperature is also most pronounced in the 32ka B.P. experiment (Figure 4.7). After entering the South Labrador Sea, this HTHS water warms up the intermediate layer, which breaks down the salinity stratification, and generates an abrupt intensification of the convective process. Accordingly, the lack of HTHS water in the South Labrador Sea leads to the absence of the AMOC overshoot in the PI experiment (Figure 4.1a; Figure 4.2a).

The HTHS tropical Atlantic water is also found in the Nordic Seas during the LGM, coinciding with the duration of the AMOC overshoot between 370 and 410 model years (Figure 4.3f). Nevertheless, it is not accompanied by an intensification of the deep-water formation (Figure 4.1c), but a substantial reduction of sea ice cover (Figure 4.1f). This suggests that the fresh water from sea ice melting constrains the convective processes during

the AMOC overshoot. The anomaly of salinity and temperature in the Nordic Seas is only a passive effect of the AMOC recovery, driven by the recovery of the deep-water formation in the South Labrador Sea.

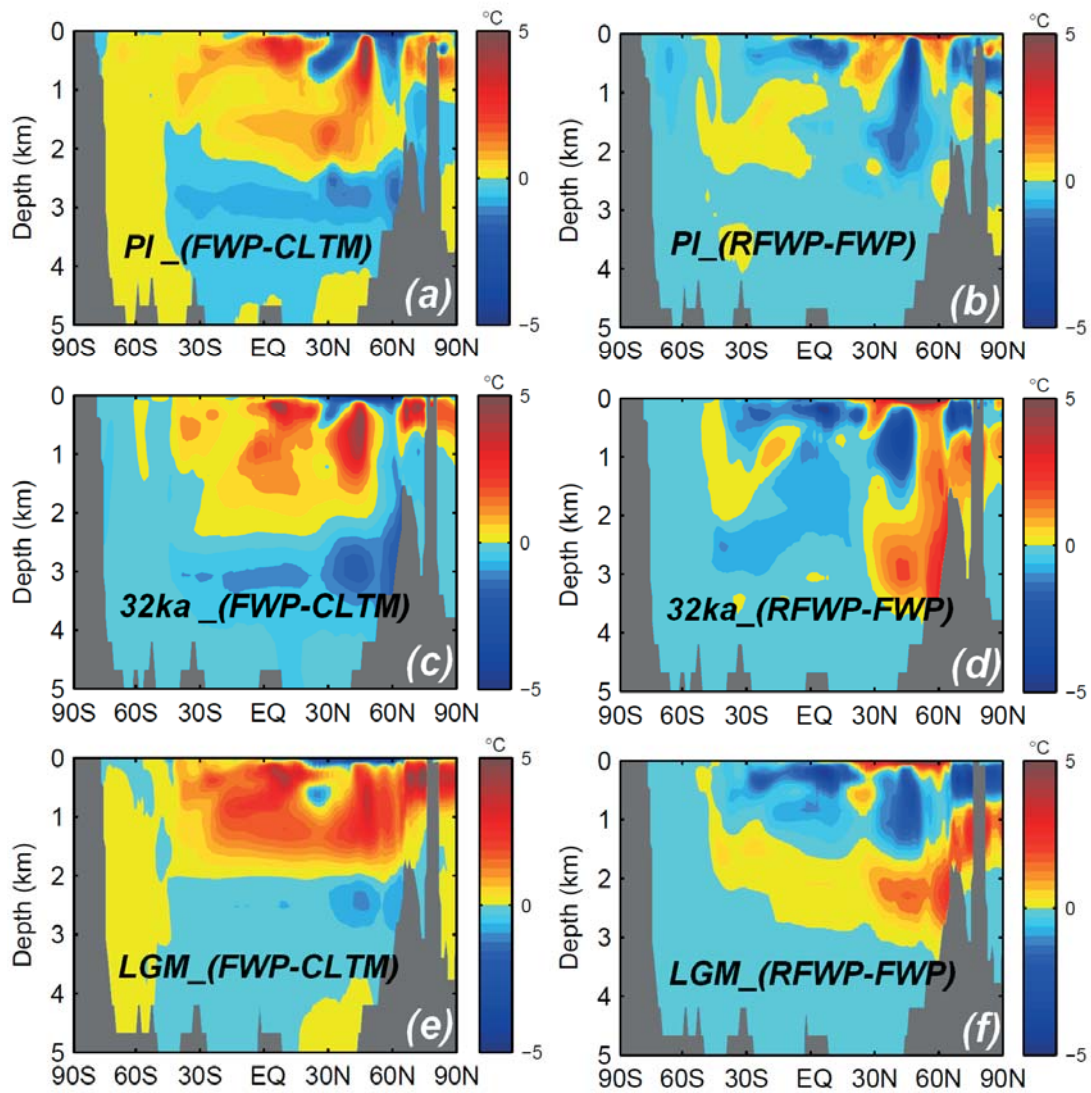


Figure 4.4. Anomalies of temperature between different states in freshwater perturbation experiments. The left column shows the difference between the states of ‘CLTM’ and ‘FWP’, and the right exhibits the anomaly between the states of ‘RFPW’ and ‘FWP’. From top to bottom, the climate state of the PI, 32ka B.P. and LGM are shown, respectively.

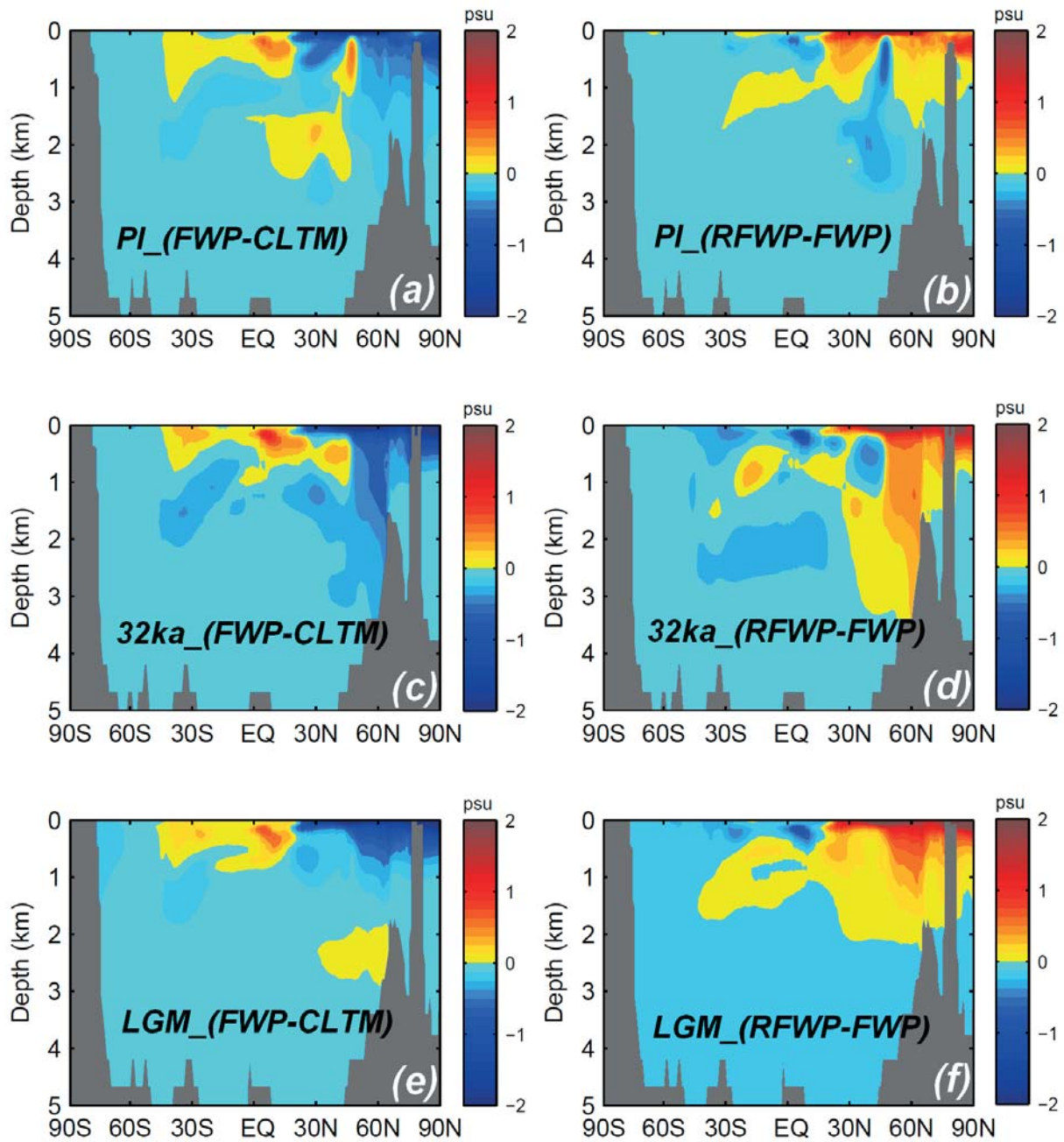


Figure 4.5. Anomalies of temperature between different states in freshwater perturbation experiments. The left column shows the difference between the states of ‘CLTM’ and ‘FWP’, and the right exhibits the anomaly between the states of ‘RFP’ and ‘FWP’. From top to bottom, the climate state of the PI, 32ka B.P. and LGM are shown, respectively. The order is the same as in the Figure 4.4.

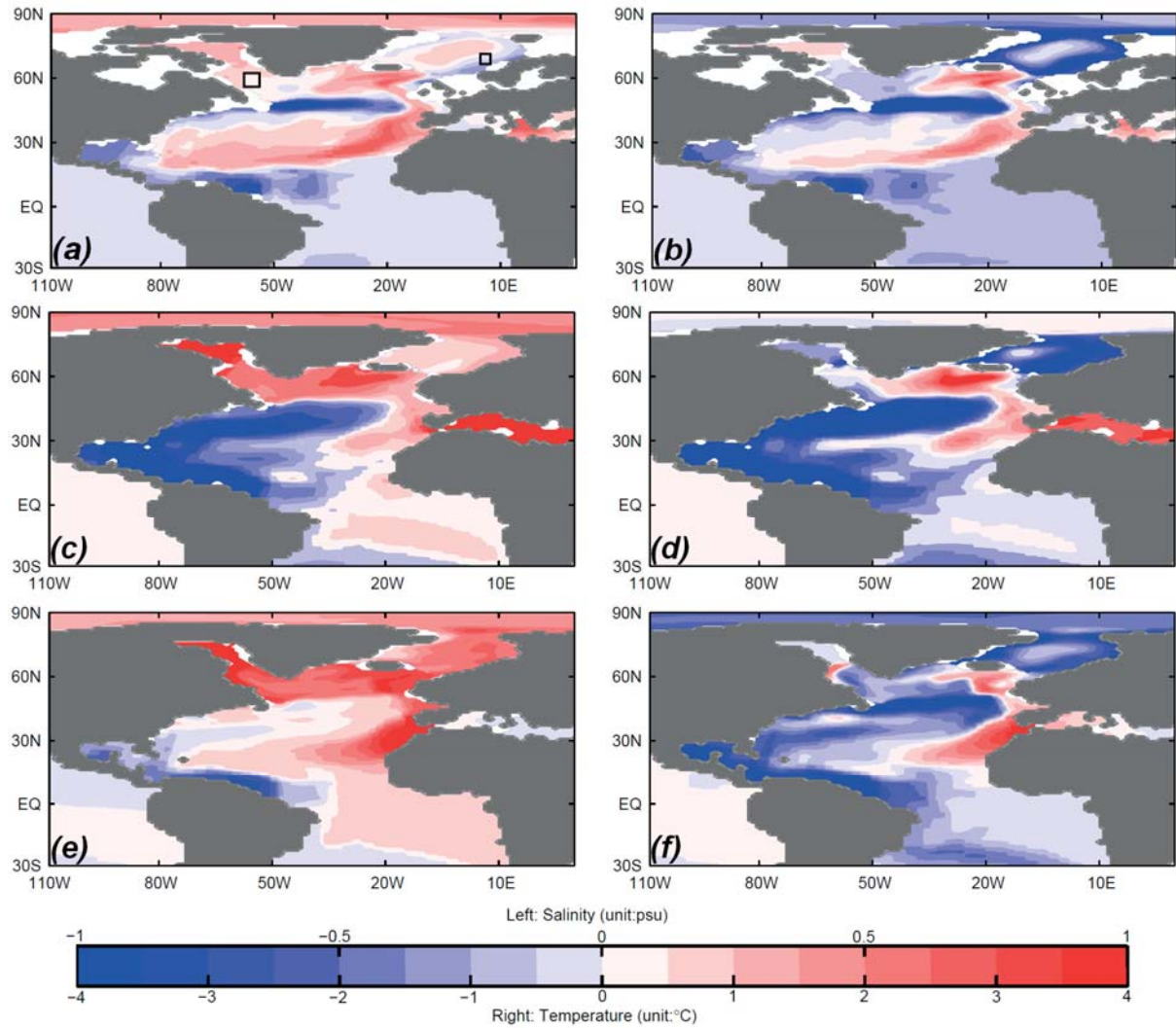


Figure 4.6. Anomalies of salinity (left column) and temperature (right column) at 500m depth of the AMOC overshoots state (32ka B.P.: 320-340 model year; LGM: 370-390 model year, or totally recovered state for the PI (340-360 model year)) relative to suppressed AMOC state (average of last 20 years with fresh water perturbation, i.e. 230-250 year). Two black boxes indicate the areas of deep-water formation in the South Labrador Sea and the Nordic Seas, respectively.

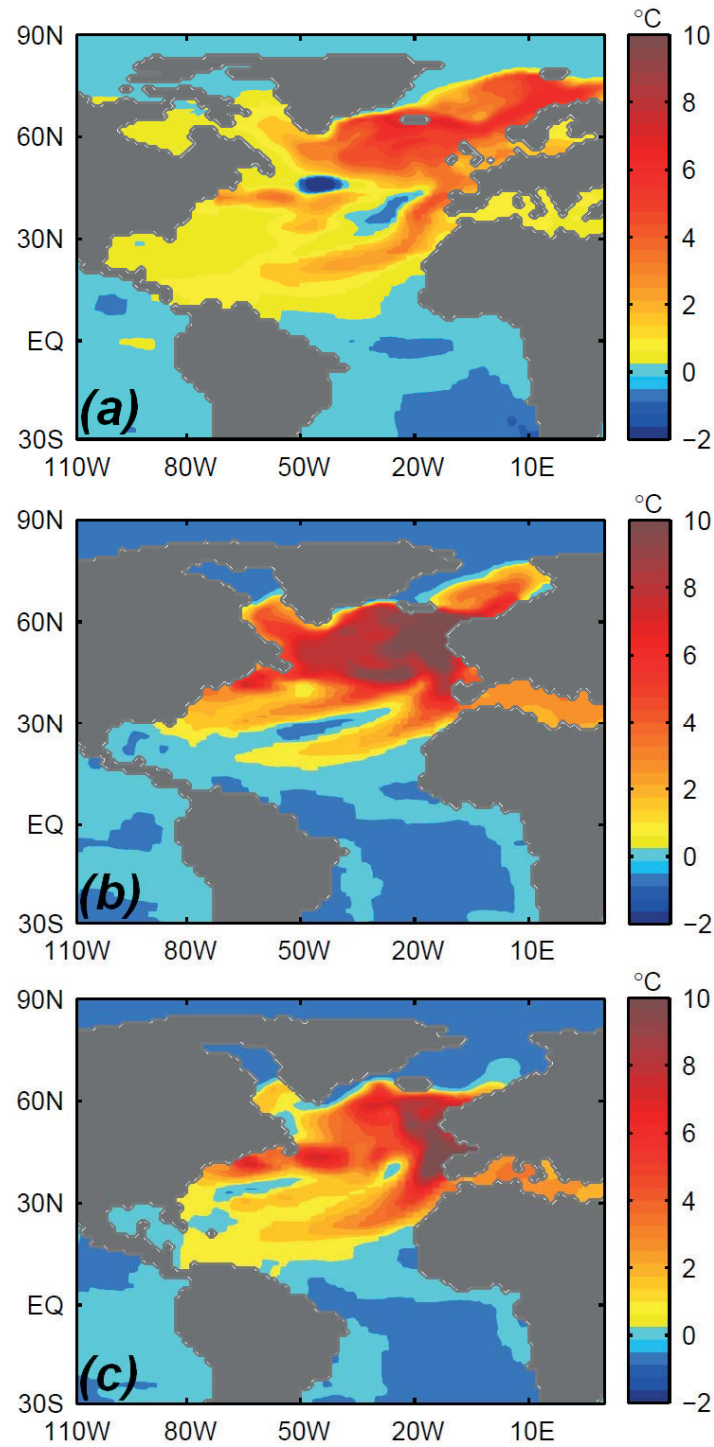


Figure 4.7. Anomaly of SSTs between the states of 'RFPW' and 'FWP'. From top to bottom, the climate state of the PI, 32ka B.P. and LGM are shown, respectively.

### **4.3 Discussion: the alternative role of the South Labrador Sea in triggering glacial AMOC overshoot**

Based on our fresh water hosing experiments we detect two different stages during the overall AMOC recovery. Compared to the PI experiment, the resumption of the AMOC is abrupt and much faster during 32ka B.P. and the LGM. The magnitude of the AMOC overshoot is particularly pronounced in the 32 ka B.P. experiment and weaker in the LGM experiment, while no overshoot occurs in the PI experiment. The abruptness of AMOC recovery and the magnitude of the overshoot are mainly governed by hydrostatical instabilities in the Labrador Sea and significant accumulations of heat and salinity in the intermediate layer of the tropical Atlantic Ocean during the freshwater perturbation. The associated changes can be interpreted as a combination of a convective (hydrostatic instability) and advective feedback (salinity advection from the tropical Atlantic), which crucially depends on the climate background.

Proxy records (e.g. Thornalley et al. [2011]) and numerical simulations (e.g. Barker et al. [2010]) indicate that the occurrence of an AMOC overshoot is closely related to the intensification of North Atlantic deep-water formation. After entering the eastern part of northern North Atlantic Ocean, the warmer and saltier tropical intermediate-layer water separates, and advects into the South Labrador Sea and the Nordic Seas, respectively. Both locations might have the potential to dominate the AMOC recovery. Liu et al. [2009] found that the overshoot is associated with a strong subsurface warming in the Nordic Sea, and they suggest a dominant role of the Nordic Seas on the AMOC overshoot. According to our investigation, the intermediate-layer warming is accompanied by a strong reduction of sea ice cover, but not correlated with an intensification of deep-water formation in the Nordic Seas. This behavior is mainly related to a stronger northward heat transport due to the recovered AMOC, which is mainly driven by the South Labrador Sea, and the restriction of deep-water

formation in the Nordic Seas by sea ice melting. Cheng et al. [2011] identified the exchange between the North Atlantic and the Nordic Seas as an important key element in explaining the full magnitude of the AMOC overshoot during the Bølling-Allerød warming. Our simulations identify that the interplay of the South Labrador Sea and the low latitude Atlantic Ocean acts as an alternative key player that governs overshoot dynamics. Furthermore, the underlying dependence of the overshoot dynamics on the background climate provides an explanation for the different climatic responses to the freshwater perturbations which are an intrinsic part of climate variability during glacial-interglacial cycles (e.g. the 8.2ka B.P. Event and the Heinrich Event 1) [LeGrande and Schmidt, 2009; Hemming, 2004].

## **5 Dynamics perspective of the GLAMAP/CLIMAP discovered extreme sea-surface conditions in the Nordic Seas during the Last Glacial Maximum**

The ocean dynamics in the Nordic Seas, including the Greenland Sea, Iceland Sea and Norwegian Sea, presents as an image of the Arctic-North Atlantic meridional water mass exchange and northward heat transport. The variability of various water inflows and waterfront systems results in the complexity of ocean circulation and vertical ventilation in the Nordic Seas, which crucially influence regional and global climate change, also sensitive to their feedbacks. For instance, Hass [1996] uses ocean sediment records to prove that the Europe climate variations since the Holocene are well coupling with the Atlantic inflow water into the Nordic Seas. It is also illustrated that the outflow water from the Nordic Seas is important for the hydrographic features in the northern North Atlantic Ocean [Rahmstorf, 1999]. Subsequently, this outflow water plays a key role in determining the North Atlantic Deep Water formation and AMOC. Furthermore, Kösters et al. [2005] demonstrates that the outflow water via the Denmark Strait also contributes to the Europe climate variations, but has a weaker effect on the AMOC in comparison to the Norwegian Current, i.e. the Atlantic inflow water. Subsequently, Köhl et al. [2007] describes that the wind stress curl around Iceland leads to a variation of the barotropic flow through the Denmark Strait. Also, Skagseth et al. [2004] concludes that the variability of the Norwegian Current is response to the changes in large-scale wind field.

Considering the important role of the Nordic Seas in climate system, the ocean circulation in the Nordic Seas would be a central piece to untangle the features of glacial climate period. So

far, various proxy records have proved that the variations of ocean circulation in the Nordic Seas is sensitive to the past climate change (e.g. Fronval and Jansen [1996]; Rasmussen et al. [2008]). Focusing on the climate during the LGM, CLIMAP [CLIMAP, 1981] and GLAMAP [Pflaumann et al., 2003; Paul and Schäfer-Neth, 2004] have reconstructed the SSTs and sea ice cover in the Nordic Seas, based on different proxies and distinct methods. Using biological transfer functions and oxygen isotope stratigraphy, CLIMAP shows constant SSTs of the Nordic Seas, which have the temperature of freezing point all the year around during the LGM, accompanied by persistent sea-ice coverage. In contrast, GLAMAP uses foraminiferal transfer functions by the SIMMAX-28 modern analogue technique, and reveals a less pronounced cooling in the Nordic Seas with significant seasonality of sea ice cover, especially a temporally sea ice free ocean in the eastern part of the Nordic Seas during the glacial summer season. In addition, the southward sea ice expansion into the northern North Atlantic Ocean is not presented in the GLAMAP with respect to CLIMAP. Using an Atmosphere General Circulation Model, Lohmann and Lorenz [2000] illustrate large differences in surface atmospheric circulation between the PI and the LGM period. Additionally, they also describe significant inconsistency between the simulations with the CLIMAP and GLAMAP surface ocean as bottom forcing. Furthermore, ESMs, with coupled atmosphere and ocean components, also exhibit large variance in accessing proxy-indicated ocean during the LGM. Braconnot et al. [2007] compare the simulations for the LGM climate by 12 different ESMs, which show large inconsistency between each other, especially in the high-latitudes ocean, whereas their differences in PI simulations are largely suppressed. Moreover, Otto-Bliesner et al. [2007] shows large spreads of AMOC spatial patterns and strengths between different ESM simulations for the LGM, resulting from their distinct simulations in polar-subpolar oceans, e.g. the Nordic Seas. Oka et al. [2012] attribute these differences in simulating glacial AMOC

to model-dependent thresholds existing in the northern North Atlantic Ocean. Overall, the stand-alone proxy study of CLIMAP and GLAMAP can only present the values on specific sites, and ESM model simulations cannot provide further knowledge of the underlying dynamics due to their disability in assessing proxy-reconstructed ocean. Therefore, the usage of a high-resolution model is crucial to understand different physical processes in the Nordic Seas. This high-resolution model has been mainly used for PI application [e.g. Kauker et al., 2003; Kauker et al., 2009], and also applied for past Nordic Seas during the Mid Holocene [Prange and Lohmann, 2004], Early Holocene [Lohmann et al., 2005] and the LGM [Stärz et al., 2012].

## **5.1 Experiments and atmospheric forcing**

### **5.1.1 Design of NAOSIM experiments**

Here, we use the NAOSIM model, whose model details have been described in Chapter 2.1. Our version of NAOSIM has been used and verified to diagnose the modern sea ice variation [e.g. Kauker et al., 2003; Kauker et al., 2009]. Based on the topography (ETOPO5) in PI experiment (NAOSIM-NCEP), sea level is reduced by 120m in our LGM experiments, with further adjustment according to glacial ice sheets [Ehlers et al., 2007], which leads to the closure of the Bering Strait and the Canadian Archipelago seas (Figure 5.1). Subsequently, the GSR, i.e. the Greenland-Scotland Ridge, becomes the only gateway for water volume and heat exchange between northern polar oceans (the Nordic Seas and Arctic Ocean) and the remained global oceans. The GSR has three ocean channels, including the Denmark Strait, the Iceland-Faroe Ridge (IFR, oceanic area between the Iceland and Faroe Island) and the Faroe-Scotland Channel (FSC, oceanic gateway between the Faroe Island and Scotland Island).

In initializing our LGM experiment, NAOSIM starts from the rest of sea ice. During the LGM, sea ice is much larger than the present, and can be fast created in the first model year. Additionally, sea ice thickness in our LGM experiments is restricted less than 30m, to avoid the unrealistic extreme sea ice growth in Baffin Bay and along northern Greenland coast [Stärz et al., 2012].

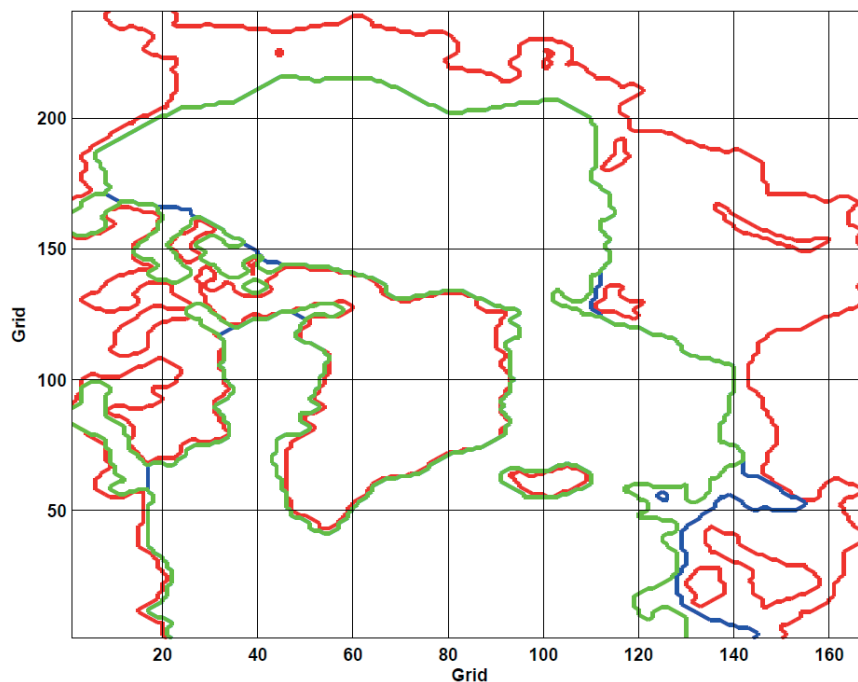


Figure 5.1. The land sea masks in the NAOSIM simulations for (red) the PD and (blue) LGM. The grey shadowed area shows the elevated land area during the LGM, cause of a 120m sea level reduction and glacial ice sheet. In addition, the green line indicate the land sea mask in our NAOSIM sensitivity study experiments for ocean gateway.

During the LGM, the Arctic climate has a reduced meteoric precipitation and a weakened hydrological cycle (Lohmann and Lorenz, 2000). The Siberian sector is influenced by cold, dry winds due to the Fenno-Scandinavian ice sheet (Hubberten et al., 2004; Siebert and

Marsiat, 2001; Siegert and Dowdeswell, 2004), as well as an anticyclonic regime over Siberia that hinders the advection of Atlantic air masses (Arkhipov et al., 1986; Velichko et al., 1997). Furthermore, the closure of the Bering Strait blocks the Pacific inflow of freshwater into the Arctic Ocean. Consequently, the amount of river discharges around Arctic Ocean in our LGM experiments is reduced from present  $3300 \text{ km}^3/\text{a}$  to  $1800 \text{ km}^3/\text{a}$  with enhanced seasonality [Aagaard, 1989; Starz et al., 2012]. According to the conservation of salt, 1 psu is homogeneously added to the ocean water. In consequence, the prescribed northern North Atlantic inflow at the southern ocean boundary is modified by adding 1 psu, additionally  $2^\circ\text{C}$  is reduced in consistent with North Atlantic cooling during the LGM period [Butzin et al., 2005]. Both our PD and LGM experiments are run for 120 years, and the mean state over the last 20 years is used for the analysis of the sea surface conditions in the Nordic Seas.

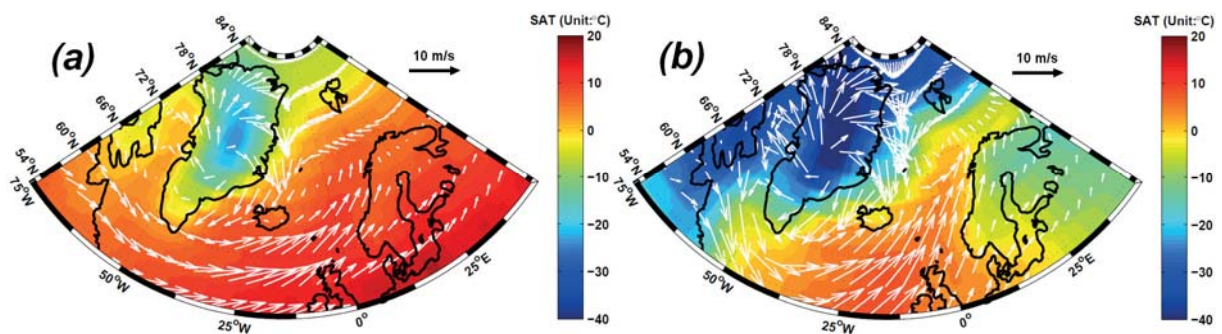


Figure 5.2. The mean state of (a) summer and (b) winter SATs and surface winds, which are NCEP/NCAR reanalysis data, used as the atmospheric forcing in our NAOSIM-NCEP experiment.

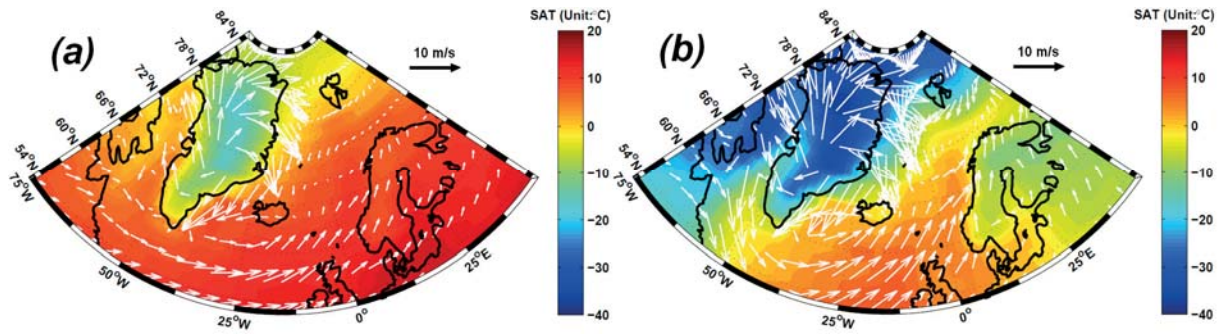


Figure 5.3. The mean state of (a) summer and (b) winter SATs and surface winds, which are simulated in the ECHAM3/T42L19 PD control experiment, and used as the atmospheric forcing in our NAOSIM-PD experiment.

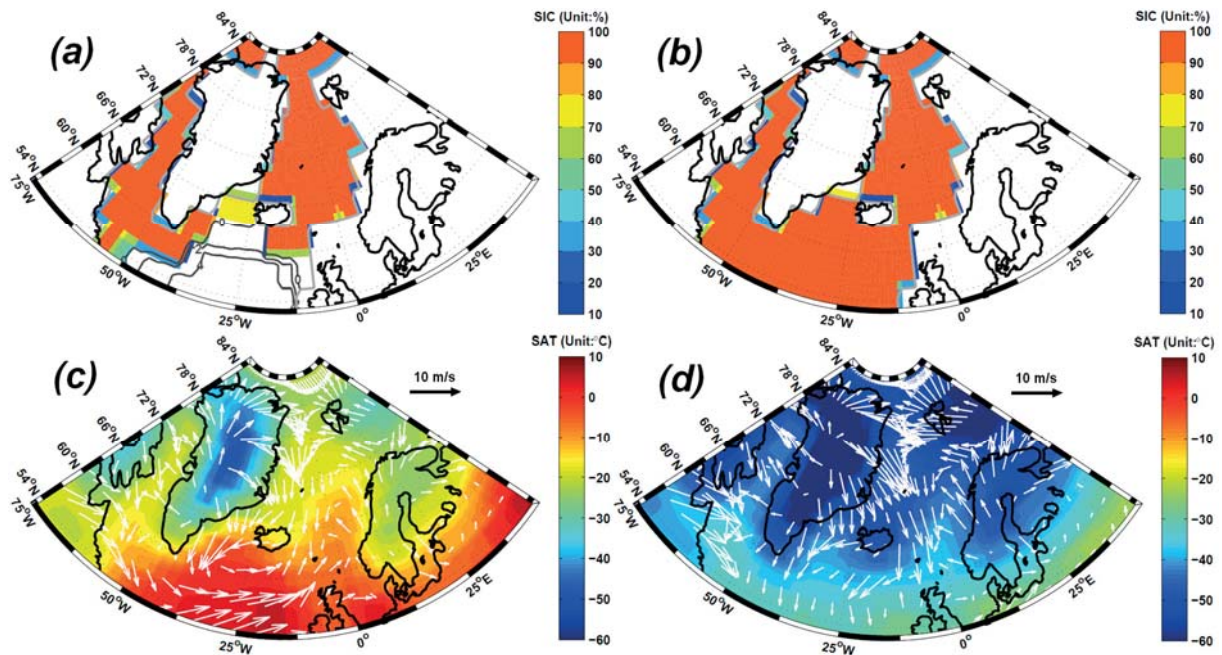


Figure 5.4. SST and sea ice cover in ECHAM3 based on CLIMAP during LGM (a) summer and (b) winter. Then, the corresponding SATs and surface winds during (c) summer and (d) winter, which are simulated by ECHAM3/T42L19 and used as the atmospheric forcing in our NAOSIM-C experiment.

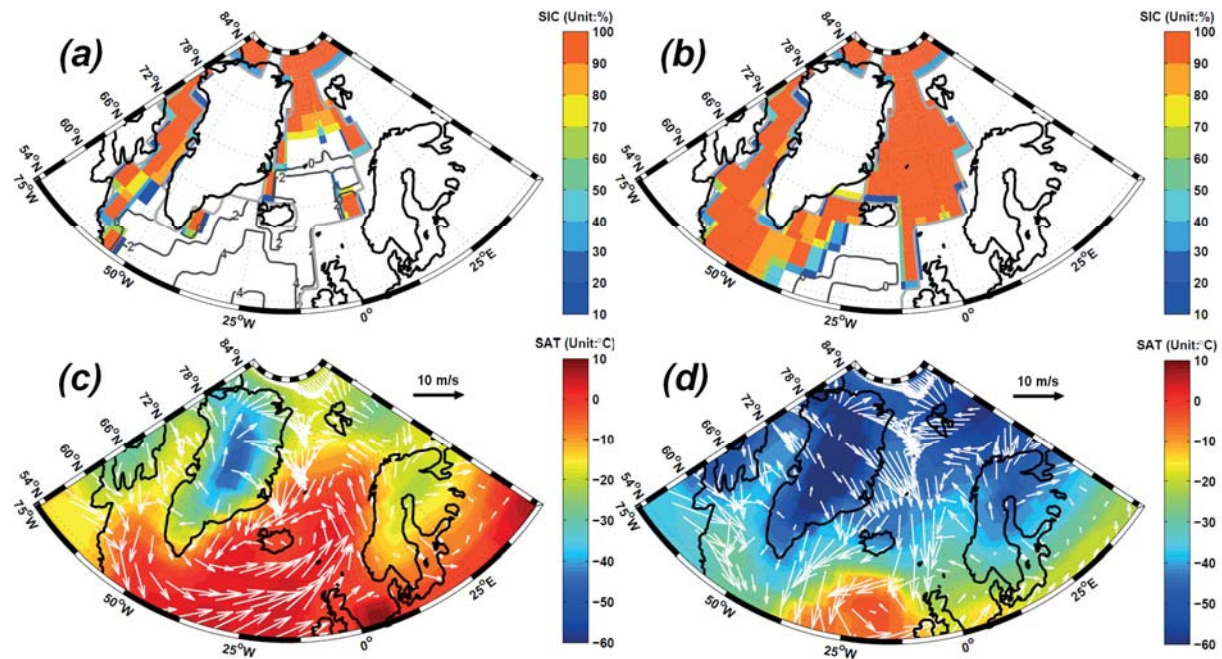


Figure 5.5. SST and sea ice cover in ECHAM3 based on GLAMAP during LGM (a) summer and (b) winter. Then, the corresponding SATs and surface winds during (c) summer and (d) winter, which are simulated by ECHAM3/T42L19, are used as the atmospheric forcing in our NAOSIM-G experiment.

### 5.1.2 Atmospheric forcing

For PI, we performed two control experiments, one with the standard daily NCEP/NCAR reanalysis data (1948-2007), i.e. NAOSIM-NCEP experiment [Kalnay et al., 1996] (Figure 5.2), the other with forcing coming from simulated surface atmosphere conditions in Atmosphere General Circulation Model (AGCM) ECHAM3/T42L19, i.e. NAOSIM-PD experiment [Lohmann and Lorenz, 2000; Romanova et al., 2004] (Figure 5.3).

Our LGM experiments use the simulated surface atmosphere conditions in Atmosphere General Circulation Model (AGCM) ECHAM3/T42L19 with respect to the CLIMAP and GLAMAP for glacial surface ocean, respectively, i.e. the NAOSIM-C and NAOSIM-G

experiment [Lohmann and Lorenz, 2000; Romanova et al., 2004] (Figure 5.4; Figure 5.5). The ECHAM3/T42L19 simulations for the LGM are forced by glacial surface boundary conditions like SSTs, albedo and sea ice cover, with adapted LGM topography and ice sheets [Lohmann and Lorenz, 2000; Romanova et al., 2004] (Figure 5.4a, b; Figure 5.5a, b). When assessing the CLIMAP corresponding atmosphere circulation, the SSTs between 30°S and 30°N is additionally reduced by 3°C, aiming to a better fit with the proxies in the tropical [Lohmann and Lorenz, 2000]. In all our NAOSIM experiments, the atmospheric boundary conditions are applied for the NAOSIM twice per day and are repeated over a 15 year cycle.

### **5.1.3 Design of sensitivity study experiments**

In regional ocean model, the choices of sea surface salinity resorting and ocean boundaries would potentially influence the simulated results, especially in the Nordic Seas (e.g. Lohmann et al., [2005]; Kaucker et al., [2005]; Drange et al., [2005]). Also, it has been illustrated that the variability of surface hydrography of the Norwegian Sea is closed related to the North Atlantic inflow during past 150 ka [Kuijpers et al., 1998]. Here, we conduct three groups of experiments for the sensitivity study of the surface salinity restoring, stream function at open ocean boundary and width of ocean gateways at the GSR, listed in Table 5.1.

Meshland et al. [2005] reconstruct different SSS of the LGM Nordic Seas from the present using proxy data, whereas Otto-Bliesner et al. [2007] also reveal various SSS in the Nordic Seas by different ESMs. Here, we conduct the NAOSIM-C-sal experiment, which applies glacial sea surface salinity from a climate model output [Shin et al., 2003] in order to discuss the effect of different surface salinity restoring. Furthermore, aiming to test the effect of different efficiencies of meridional water mass exchange at the 50°N oceanic boundaries, we conduct the experiments with modification of a half additional (NAOSIM-C-3/2PSI) and a half reduced (NAOSIM-C-1/2PSI) stream function referring to the NAOSIM-C experiment,

respectively. A similar sensitivity study has been done by Kauker et al. [2005] for present conditions. Moreover, we also design two experiments with closed FSC and partially closed IFR, which locates at the main path of the Norwegian Current, to further diagnose the effect of the North Atlantic inflow water to the LGM Nordic Seas surface conditions (NAOSIM-C-gtway and NAOSIM-G-gtway experiments), which inflow is illustrated to be different from present, and important for the LGM Nordic Seas [Rasmussen and Thomsen, 2008].

## **5.2 Results of high-resolution NAOSIM experiments**

### **5.2.1 The experiment for present-day Nordic Seas**

Our control experiment (NAOSIM-NCEP) matches the observation of the oceanic circulation of the surface Nordic Seas and other high-resolution ocean model simulations [e.g. Kauker et al., 2003; Drange et al., 2005] (Figure 5.6). Compared to NAOSIM-NCEP experiment, our NAOSIM-PD experiment also successfully captures the main features of surface ocean conditions in the Nordic Seas (Figure 5.6; Figure 5.7). However, sea ice edge in our NAOSIM-PD experiment is relatively eastward shifted in the East Greenland Current area, which is related to the stronger zonal winds in the western part of the Nordic Seas (Figure 5.2; Figure 5.3; Figure 5.6a, b; Figure 5.7a, b).

As shown in Figure 5.8a, b, the Norwegian Current transports warm and salty North Atlantic water into the Nordic Seas via the FSC. Subsequently, it flows northwards along the Scandinavian coast to the south of Svalbard. Then, one branch of this current enters the Arctic Ocean through the Barents Sea, and the other joins in the East Greenland Current via the Northern Greenland Sea. The Arctic outflow water, which is colder and fresher than North Atlantic inflow waters, dominates the western part of the Nordic Seas, with seasonal

characteristic of southward sea ice transport (Figure 5.6a, b; Figure 5.8a, b). In present, central and eastern parts of the Nordic Seas are always sea ice-free, and the SSTs in this region are above 0°C all year around (Figure 5.6a, b). In the atmosphere, the relevant SATs over the Nordic Seas exhibit notable difference between the east and west part, as well as a stronger seasonality in temperature (Figure 5.2). Compared to summer, winter SATs exhibit a larger meridional gradient over the east part of the Nordic Seas, accompanying stronger northward winds over the Norwegian Current. At the same time, the wind above the East Greenland Current is also notably intensified during winter, which encourages a southward advection of Arctic sea ice into the Nordic Seas. As shown in Figure 5.2, winter wind fields over the GSR have a larger northward tilt that may accelerate the North Atlantic surface inflow.

Table 5.1 List of our NAOSIM experiments

Experiment Name	Description
NAOSIM-NCEP	PD control experiment with NCEP atm. forcing
NAOSIM-PD	PD expt. with ECHAM3/T42L19 ctrl. expt. outdata as atm. forcing
NAOSIM-C	LGM standard set up with CLIMAP corresponding atm. forcing
NAOSIM-G	LGM standard set up with GLAMAP corresponding atm. forcing
NAOSIM-C-sal	NAOSIM-C, with CCSM output SSS as surface salinity restoring
NAOSIM-C-1/2PSI	NAOSIM-C, with 1/2 reduced stream function at open boundary
NAOSIM-C-3/2PSI	NAOSIM-C, with 1/2 increased stream function at open boundary
NAOSIM-C-gtway	NAOSIM-C, with closed FSC and partially closed IFR
NAOSIM-G-gtway	NAOSIM-G, with closed FSC and partially closed IFR.

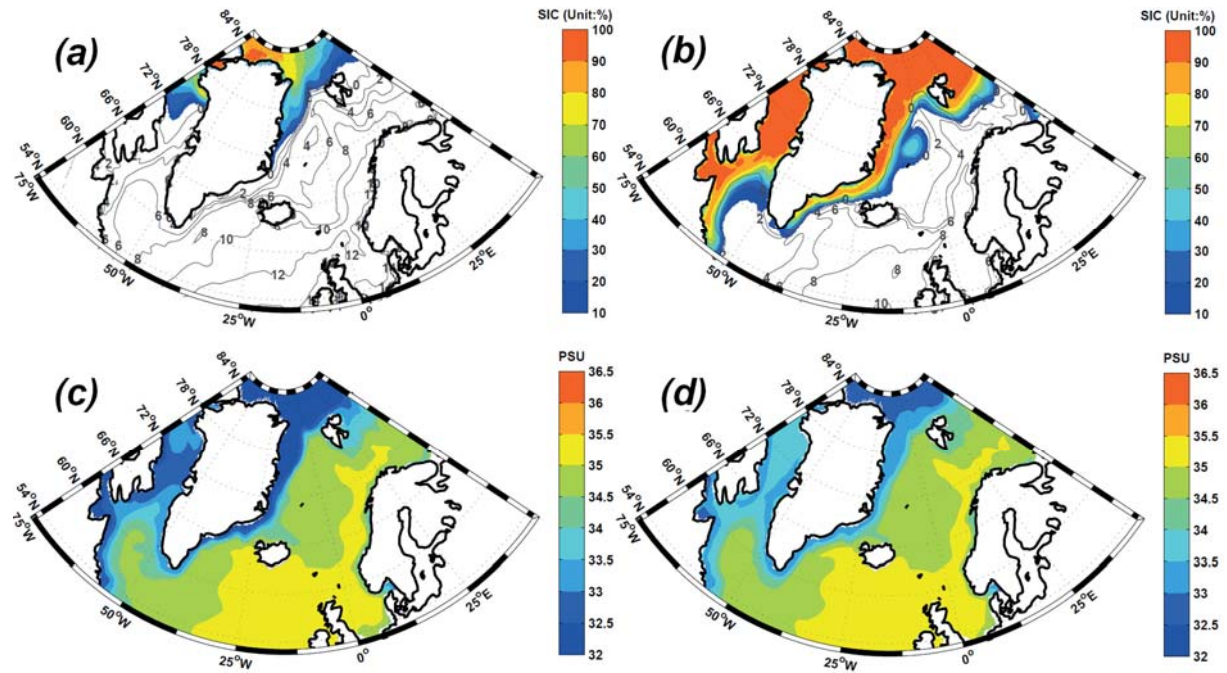


Figure 5.6. The simulated SST, SIC (upper row) and SSS (lower row) in our NAOSIM-NCEP experiment. Summer and winter seasons are shown in the left and right columns, respectively.

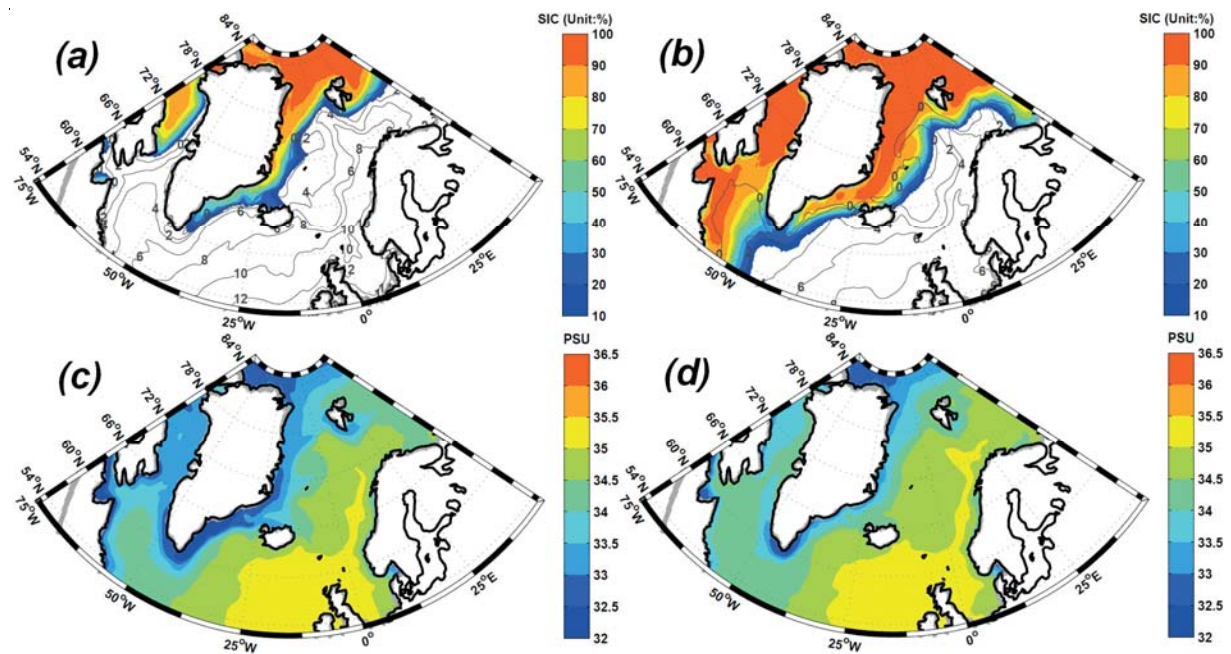


Figure 5.7. The simulated SST, SIC (upper row) and SSS (lower row) in our NAOSIM-PD experiment. Summer and winter seasons are shown in the left and right columns, respectively.

### 5.2.2 The CLIMAP and NAOSIM-C experiment

CLIMAP emphasizes three dominant features of surface conditions in the Nordic Seas during the LGM [CLIMAP, 1981]:

- (i) The SSTs of the Nordic Seas are at the freezing point during the summer, as cold as in winter (Figure 5.4a).
- (ii) Perennial sea ice covers the entire Nordic Seas, which is southwards exported via all the three oceanic channels of the GSR (Figure 5.4a, b)
- (iii) The northern North Atlantic Ocean also exhibits low SSTs, and is influenced by the southwards exported sea ice from the Nordic Seas (Figure 5.4a, b).

In atmosphere, the corresponding SATs and surface winds with respect to the CLIMAP, simulated in the ECHAM3/T42L19 experiment, are shown in Figure 5.4c, d, which have been used to diagnose the changes in the surface atmospheric circulation during the LGM [Lohmann and Lorenz, 2000].

Summer SATs over the Nordic Seas is colder than  $-15^{\circ}\text{C}$ , whereas it becomes lower than  $-45^{\circ}\text{C}$  during LGM winter. The strongest cooling is found over the area of PD Barents Sea, which is covered by ice sheet during the LGM (Figure 5.4c, d). In contrast, the area south to  $60^{\circ}\text{N}$  in the northern North Atlantic Ocean shows the warmest, which is above  $0^{\circ}\text{C}$  during summer. The directions of surface winds over the Nordic Seas are mostly constant throughout the year, and have noticeably stronger speeds in winter (Figure 5.4c, d). However, the surface wind directions over the GSR are reversed in winter from the northward direction in summer, accompanying stronger winter sea ice export across the GSR (Figure 5.4). In comparison to the NAOSIM-NCEP experiment, offshore winds are shown along the Scandinavian coast, which result from the existence of the Scandinavian ice sheet during the LGM (Figure 5.2; Figure 5.4c, d).

As shown in Figure 5.4a, b and Figure 5.9a, b, our NAOSIM-C experiment provides similar SSTs and sea ice cover as in the CLIMAP. In the central and eastern parts of the Nordic Seas, perennial sea ice is above 50% concentration all year around, with sea ice edges penetrating to the south of GSR (Figure 5.9a, b). Furthermore, the SST line of 0°C in the northern North Atlantic Ocean is located at the same position as proposed by the CLIMAP reconstruction (Figure 5.4a, b; Figure 5.9a, b).

Moreover, our NAOSIM-C experiment supplies additional details of spatial features of sea ice cover. In contrast to the completely sea ice covered summer Nordic Seas in the CLIMAP reconstruction, sea ice in our NAOSIM-C experiment exhibits a eastward reduction in SIC from >90% (central Nordic Sea) to ~60% (the area closed to the Scandinavia coast) during summer (Figure 5.9a, b). Also, the seasonal cycle of total sea ice cover in the entire Nordic Seas shows a notably enhanced seasonality in our NAOSIM-C experiment, mainly resulting from the central and eastern parts of Nordic Seas (Figure 5.10). It is also shown that the oceanic area west to British Islands has winter SSTs above 0°C with sea ice cover < 30% in our NAOSIM-C experiment, whereas this area is reconstructed to be covered by a perennial sea ice by CLIMAP (Figure 5.4a, b and Figure 5.8a, b). In general, our NAOSIM-C experiment is in agreement with the SSTs and sea ice cover of the CLIMAP for the Nordic Seas, and model-supplied details of sea ice cover additionally shows a notable seasonality in the central and eastern parts of Nordic Seas.

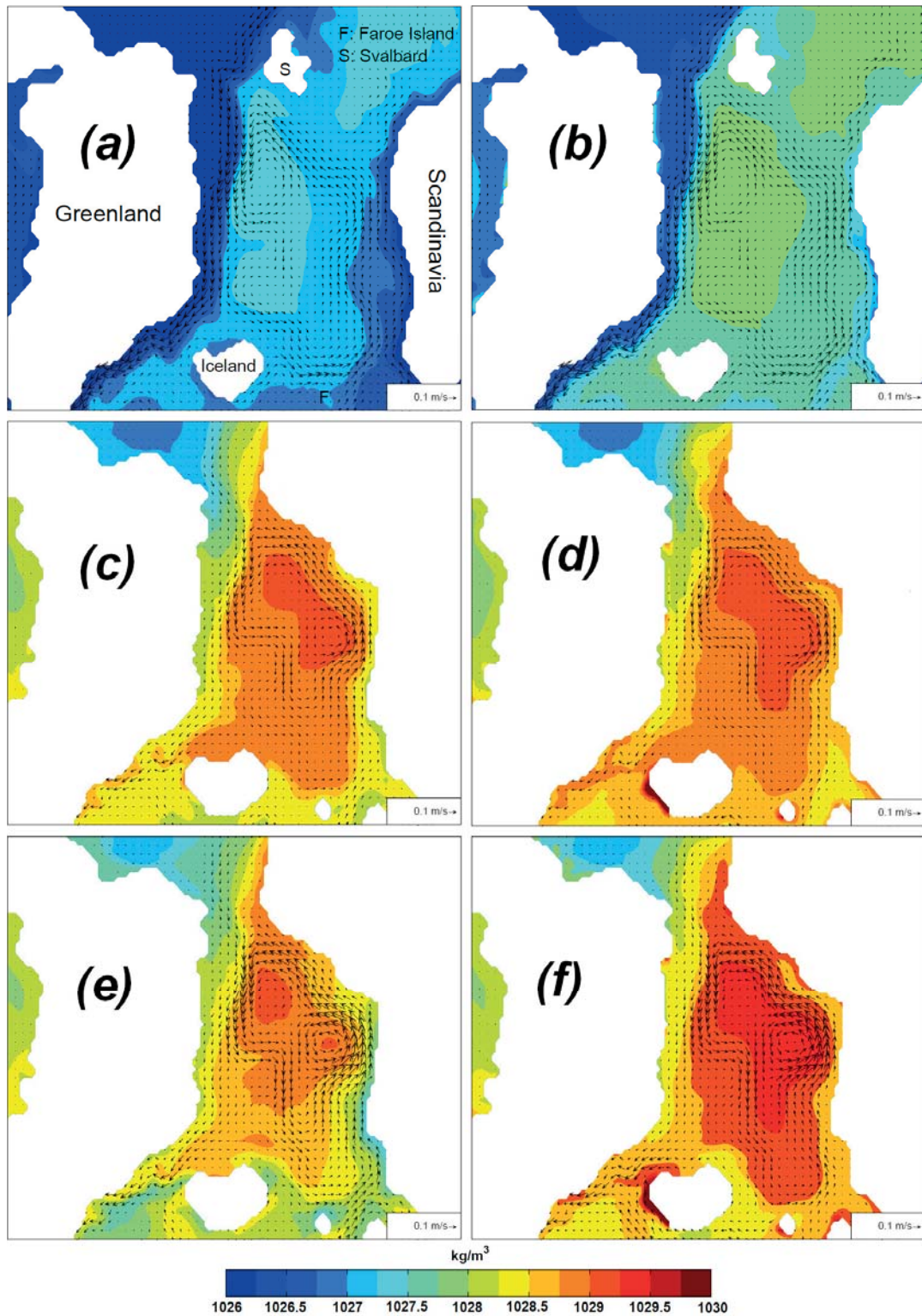


Figure 5.8. The upper 60m-mean ocean circulation and water density during summer (left column) and winter (right column) are shown for (a and b) NAOSIM-NCEP, (c and d) NAOSIM-C and (e and f) NAOSIM-G experiments, respectively.

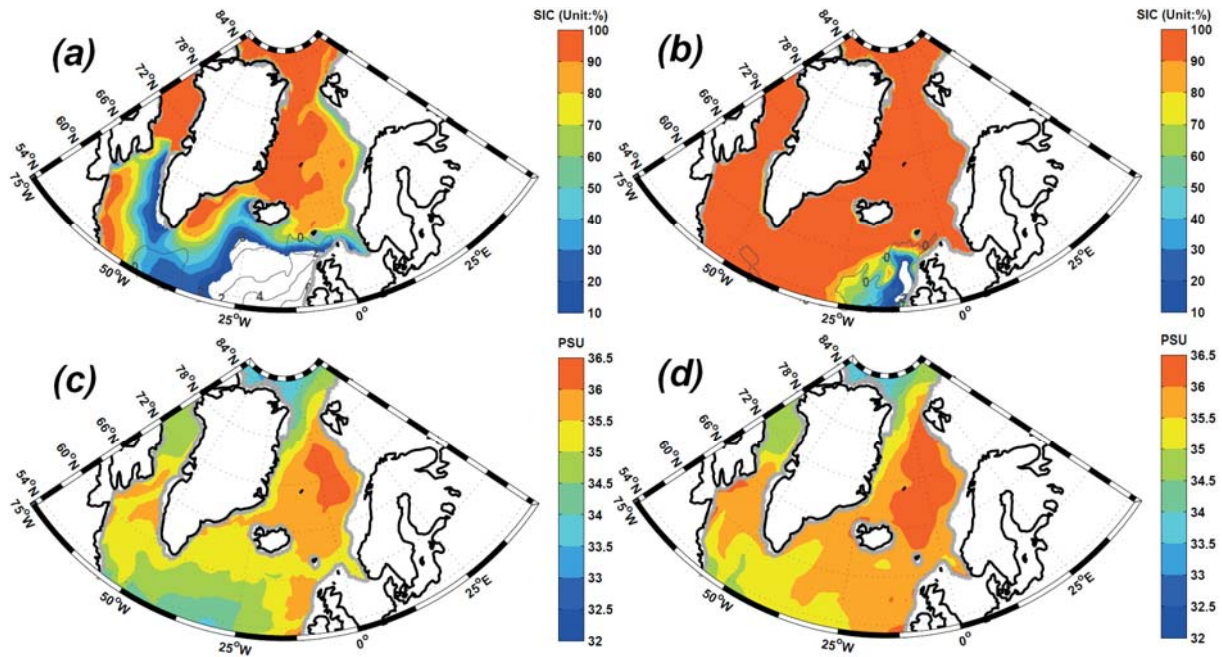


Figure 5.9. The simulated SST, SIC (upper row) and SSS (lower row) in our NAOSIM-C experiment. Summer and winter seasons are shown in the left and right columns, respectively.

Our NAOSIM-C experiment also provides the information of the SSS and ocean circulation in the Nordic Seas during the LGM. The generally increase in salinity resulted from the conservation of salt from the 120m reduction of sea level during the LGM (Figure 5.6c, d; Figure 5.9c, d). The Arctic outflow water leads to the low salinity in the western part of the Nordic Seas. Compared to NAOSIM-NCEP experiment, a most emphasized change is the high value of salinity within the central part of the Nordic Seas in our NAOSIM-C experiment (Figure 5.6c, d; Figure 5.9c, d). As shown in Figure 5.11, this high SSS is resourced from the upwelling of deeper-layer water with high salinity. In addition, the surface ocean circulation follows the spatial changes of sea water density, which mostly describes the geostrophy effect. In the comparison between Figure 5.8c, d and Figure 5.9c, d, it is shown that the surface density changes in the LGM Nordic Seas are closely related to the SSS variations. During the LGM, the Nordic Seas surface circulation show two major distinct features from the present:

- (i) An cyclonical gyre are found in the eastern part of the Nordic Seas in our NAOSIM-C experiment, whose core positions can be presented with highest salinity.
- (ii) (ii) Both the East Greenland Current and the Norwegian Current are notably weaker, which indicates a weaker water exchange between the Arctic-Nordic ocean parts and the northern North Atlantic Ocean.

As shown in Figure 5.12g, h, the water exchange across GSR is balanced due to the closure of the Bering Strait and the Canadian Archipelago Seas, and the northward heat transport across the GSR during the LGM is reduced to ~25% of the present. Furthermore, the total water exchange via the Fram Strait is always balanced to be zero, since it is the unique oceanic gateway between the Nordic Seas and the Arctic Ocean during the LGM, whereas the heat transport becomes insignificant in our NAOSIM-C experiment (Figure 5.12i, j).

### **5.2.3 The GLAMAP and NAOSIM-G experiment**

Compared to CLIMAP, GLAMAP reveals a less pronounced surface cooling in the Nordic Seas during the LGM, with stronger seasonality [Pflaumann, 2003]. As shown in Figure 5.9a and Figure 5.13a, the eastern parts of the Nordic Seas are completely free of sea ice in summer, and the SSTs are higher than 3°C at the GSR. During winter, sea ice covers the entire Nordic Seas, which has a significant sea ice export into the northern North Atlantic Ocean via the Denmark Strait and the FSC (Figure 5.13b). As shown in Figure 5.4c, d and Figure 5.5c, d, the GLAMAP corresponding atmospheric conditions, used in the NAOSIM-G experiment, also exhibit significant differences in comparison with CLIMAP indicated surface Atmospheric conditions. In contrast to persistent low SATs (<0°C) all year around used for the NAOSIM-C experiment, the GLAMAP corresponding summer SATs show the temperature higher than 0°C over the central and eastern parts of the Nordic Seas, whereas they reduce by 20°C in winter (Figure 5.4c, d; Figure 5.5c, d). This winter-summer variation

in SATs is suppressed over the northern North Atlantic Ocean south to GSR. In accompany, surface wind directions above the Norwegian Current pathway reveals a reversion between summer (northward) and winter (southwards) season, which wind direction change is only seen over the GSR in the NAOSIM-C experiment. Along the Scandinavian coast, the ice sheet induced offshore winds are exhibited to be similar as the CLIMAP corresponding surface atmospheric circulation.

In our NAOSIM-G experiment, winter sea ice cover and SSTs are simulated to be mostly equivalent to the GLAMAP (Figure 5.5a, b; Figure 5.13a, b). However, the central part of the Nordic Seas, is described with a gradual SIC change from >90% (western part of the Nordic Sea) to total absence (eastern part of the Nordic Sea) in summer, which is reconstructed to be completely sea ice free by proxies (Figure 5.5a; Figure 5.13a). In accompany, the summer SSTs along the Scandinavian coast reach 2°C. At the same time, sea ice export via the GSR is not as strong as in winter, and only throughout the Denmark Strait. Compared to the NAOSIM-C experiment, this enhanced seasonal variability in our NAOSIM-G experiment is in line with the difference between CLIMAP and GLAMAP.

In spite of significant differences in SST and sea ice cover, the SSS and surface oceanic circulation are comparable between the NAOSIM-C and NAOSIM-G experiments (Figure 5.9c, d; Figure 5.13c, d; Figure 5.8c-f). Nevertheless, the area with high salinity in the eastern part of the Nordic Seas shows larger winter-summer difference in the NAOSIM-G experiment. In summer, the reduction of high SSS area is accompanied by stronger sea ice melting in the southeastern part of the Nordic Seas, whereas sea ice grows significantly in the northeastern part of the Nordic Seas (Figure 5.13c; Figure 5.14a). Moreover, the surface oceanic circulation in the NASOM-G experiment has higher velocities along the Norwegian Current pathway than the NAOSIM-C experiment, which is in agreement with stronger wind speeds

in NAOSIM-G experiment (Figure 5.4c, d; Figure 5.5c, d; Figure 5.8c-f). The northward surface winds over the Norwegian Current in summer have a positive feedback in accelerating the surface circulation of Nordic Seas, when the surface ocean is free of sea ice cover. In consequence, this stronger surface wind can lead to an intensified North Atlantic inflow and northward heat transport via the FSC than in the NAOSIM-C experiment (Figure 5.12e). In contrast to the stronger seasonality in our NAOSIM-C experiment than the CLIMAP reconstruction, our NAOSIM-G experiment reveals a suppressed seasonal cycle than the GLAMAP reconstruction (Figure 5.10).

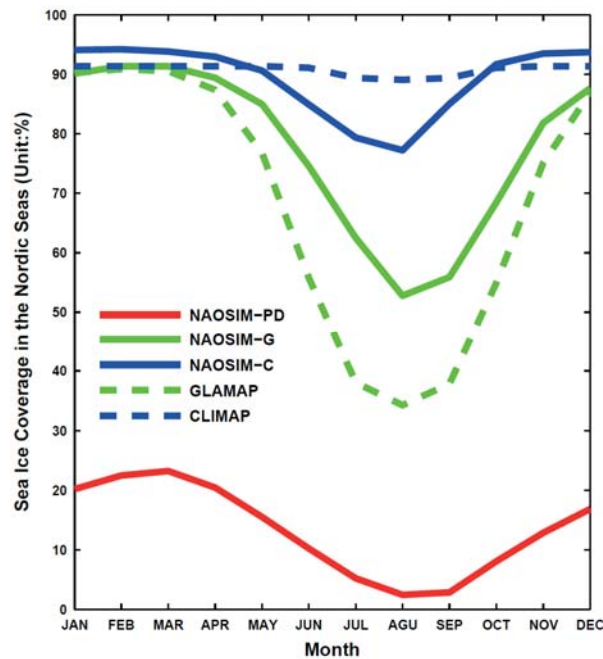


Figure 5.10. The seasonality of sea ice cover in the Nordic Seas. Proxy data indicated seasonal cycle are shown in dashed lines (CLIMAP: dashed blue line and GLAMAP: dashed green line), whereas the seasonal cycle simulated in our NAOSIM experiments are shown in solid lines (NAOSIM-NCEP: solid red line; NAOSIM-C: solid blue line and NAOSIM-G: solid green line).

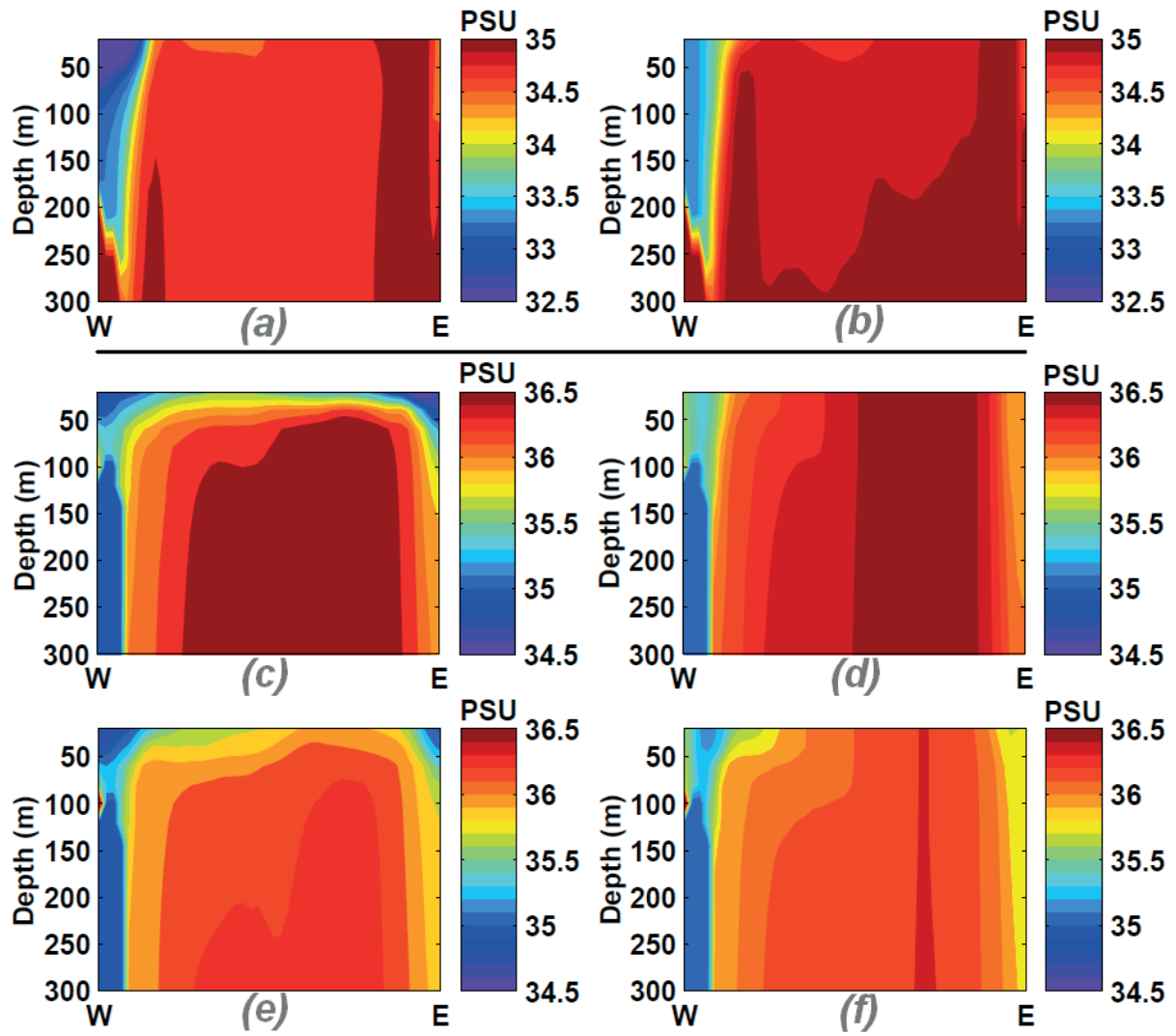


Figure 5.11. Salinity at vertical Section in the Nordic Seas at 72°N during summer (left column) and winter (right column), which are shown for (a and b) NAOSIM-NCEP, (c and d) NAOSIM-G and (e and f) NAOSIM-C experiments, respectively.

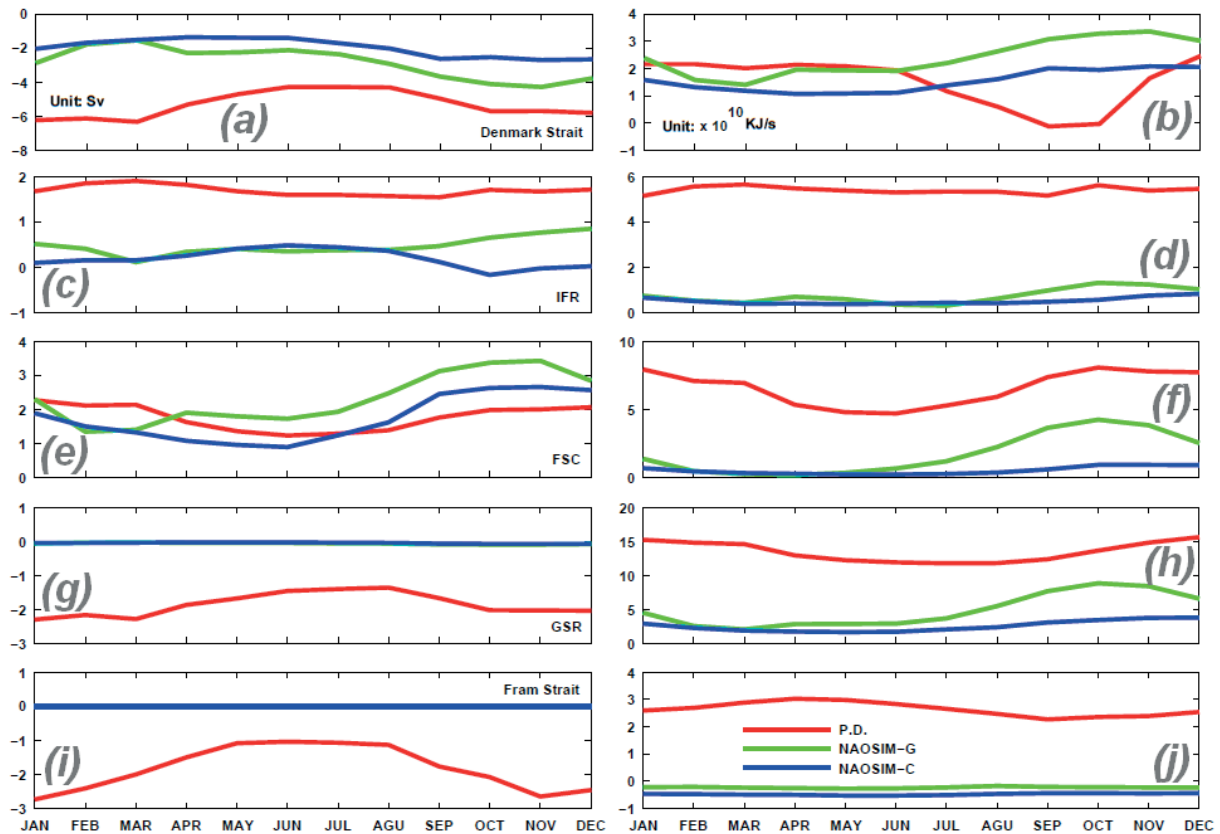


Figure 5.12. The seasonal cycle of water (left column) and heat transport (right column) across various ocean gateways (IFR: Iceland-Faroe Ridge, FSC: Faroe-Scotland Channel, GSR: Greenland-Scotland Ridge). The northward water and heat transport are exhibited with positive values.

#### 5.2.4 The sensitivity study of sea surface salinity restoring

In comparison between the NAOSIM-C and NAOSIM-C-sal experiments, the main differences are shown in the oceanic area south to GSR (Figure 5.9 and Figure 5.15). The usage of glacial salinity restoring field significantly leads to the differences in the northern North Atlantic Ocean, which have higher SST, SSS and reduced sea ice cover. The  $0^{\circ}\text{C}$  SST line is northward shifted into the GSR area (Figure 5.15), and the northeastern part of the North Atlantic Ocean is free of sea ice during winter.

In contrast, the sea surface conditions (SST, SSS and sea ice cover) show insignificant changes in the Nordic Seas (Figure 5.9 and Figure 5.15). However, in the other part of NAOSIM model areas, the choice of surface salinity restoring is important for the maintaining of the halocline in the surface layer of the Arctic Ocean during the LGM, which is not shown here, but well explained by Stärz et al. [2012].

### 5.2.5 The sensitivity study of open ocean boundary

As shown in Figure 5.16 and Figure 17, a 50% change in stream function at ocean boundary leads to negligible variations of the SSTs and sea ice cover in the LGM Nordic Seas. In addition, the oceanic water and heat transport across different ocean gateways also show insignificant changes, which are much less than the anomalies between the NAOSIM-C and NAOSIM-G experiment, and are also kept in similar amplitude of seasonal cycle as the NAOSIM-C experiment (Figure 5.18).

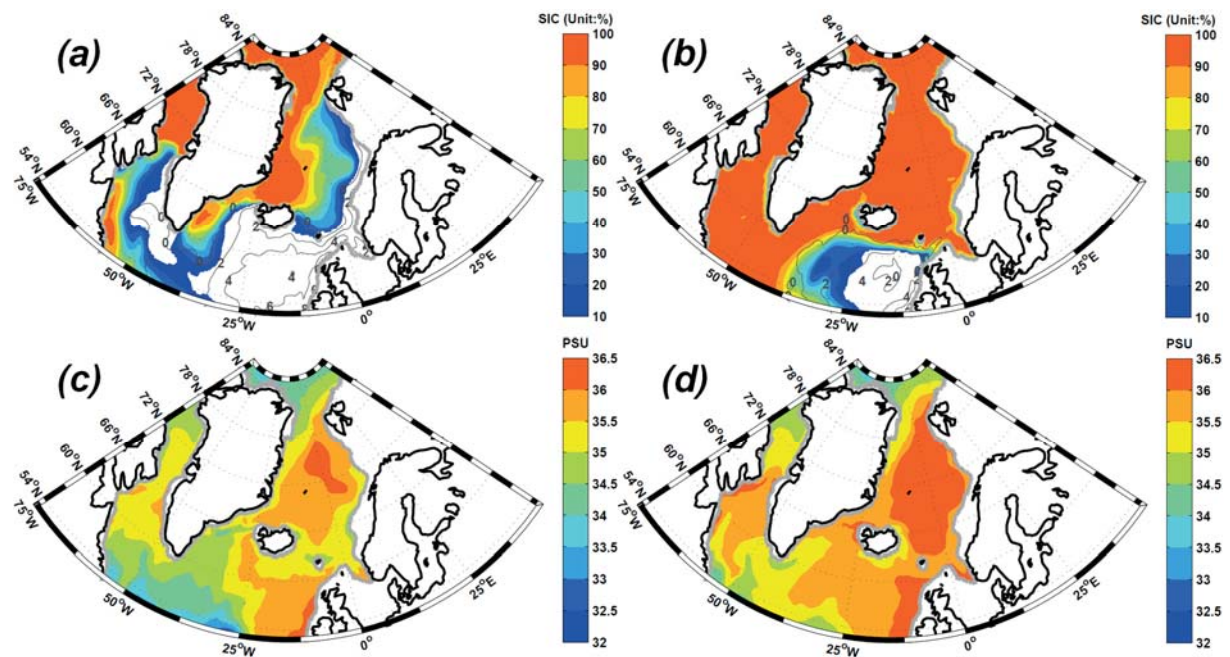


Figure 5.13. The simulated SST, SIC (upper row) and SSS (lower row) in our NAOSIM-G experiment. Summer and winter seasons are shown in the left and right columns, respectively.

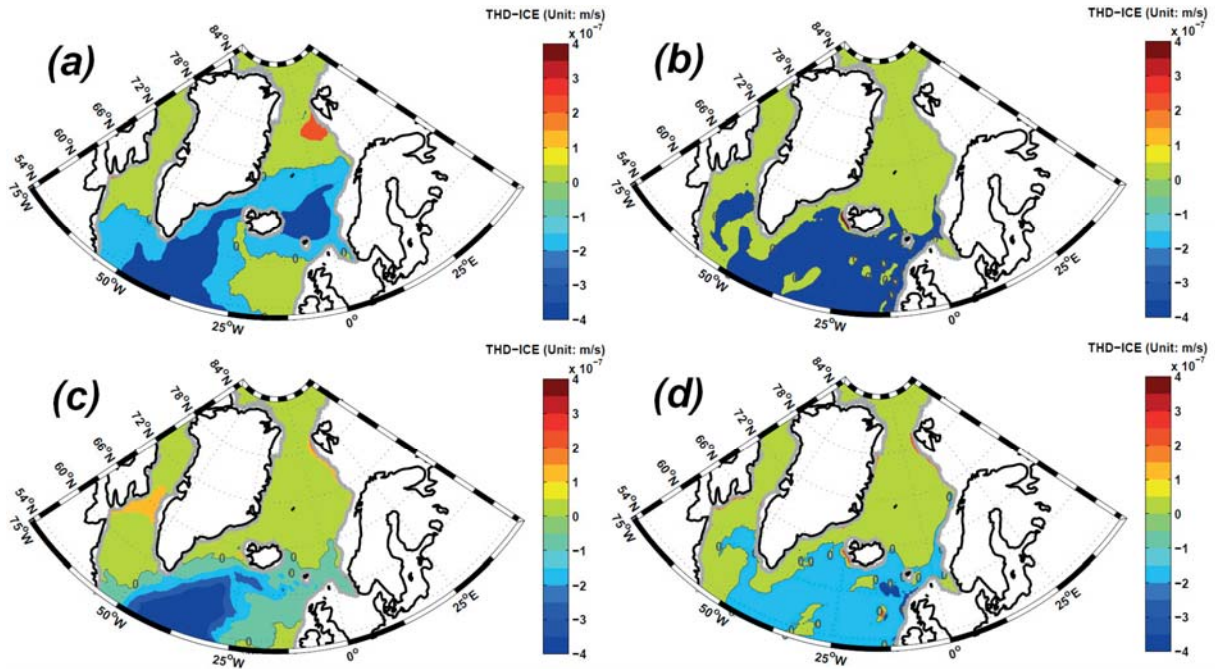


Figure 5.14. The summer (left column) and winter (right column) thermal-dynamical sea ice growth in the (a, b) NAOSIM-G and (c, d) NAOSIM-C experiments. The positive values of thermodynamic sea ice growth means sea ice formation.

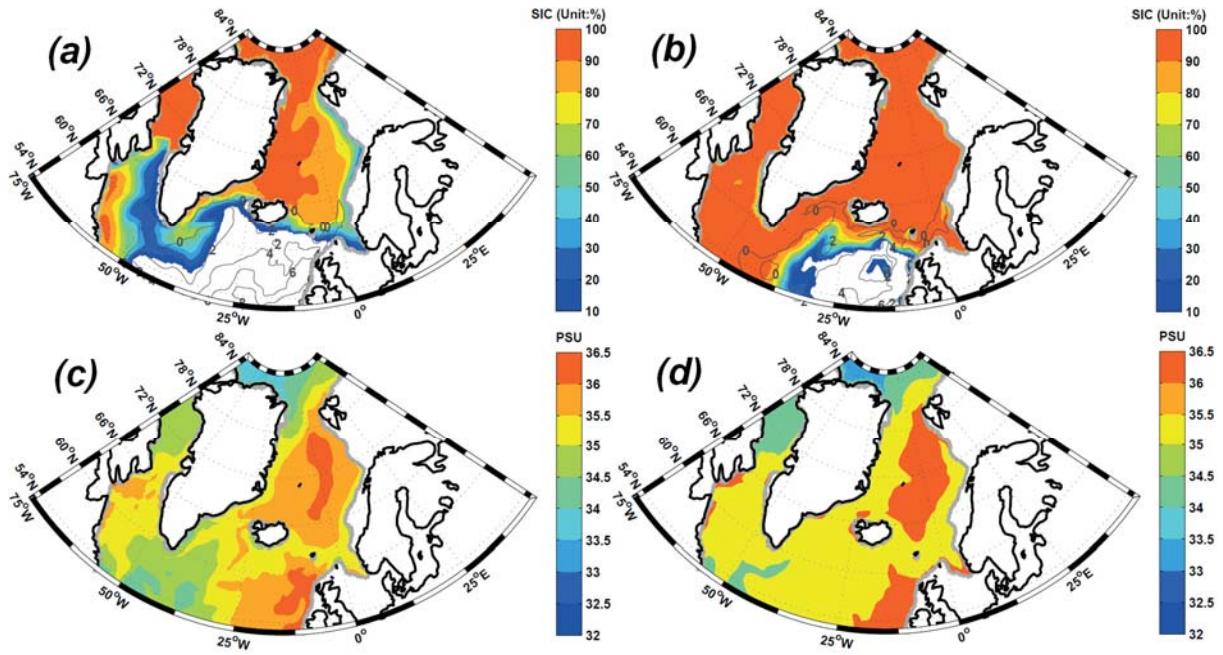


Figure 5.15. The simulated SST, SIC (upper row) and SSS (lower row) in our NAOSIM-C-sal experiment. Summer and winter seasons are shown in the left and right columns, respectively.

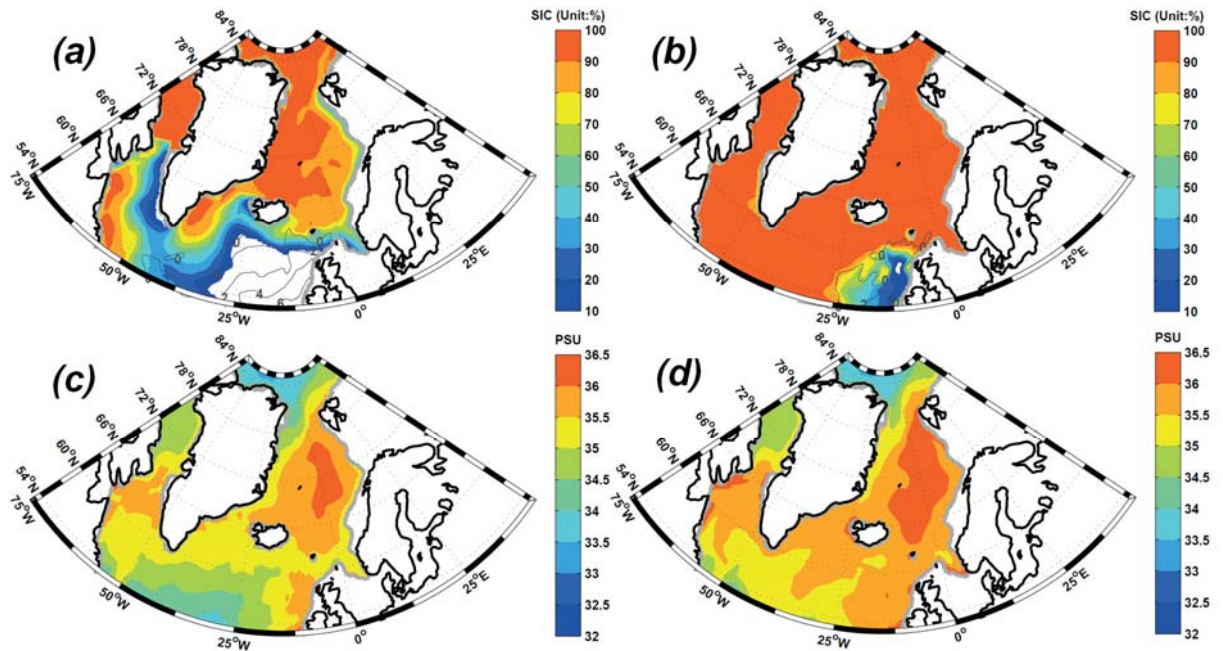


Figure 5.16. The simulated SST, SIC (upper row) and SSS (lower row) in our NAOSIM-C-1/2PSI experiment. Summer and winter seasons are shown in the left and right columns, respectively.

### 5.2.6 The sensitivity study of the ocean gateway

As shown in Figure 5.9 and Figure 5.19, under the CLIMAP atmospheric forcing, the closure of ocean gateways in the NAOSIM-C-gtway experiment results in a reduced southward sea ice export into the northern North Atlantic Ocean in both summer and winter, whereas there is an enhanced seasonality of SSTs and sea ice cover in the eastern part of the Nordic Seas than the CLIMAP, as same as in our NAOSIM-C experiments. In addition, the GLAMAP corresponding experiments with either open (NAOSIM-G) or closed ocean gateways (NAOSIM-G-gtway) are simulated to be in comparable surface ocean conditions in the Nordic Seas, whose anomalies are mostly exhibited in the SSTs of the northwestern part of the North Atlantic Ocean (Figure 5.13; Figure 5.20).

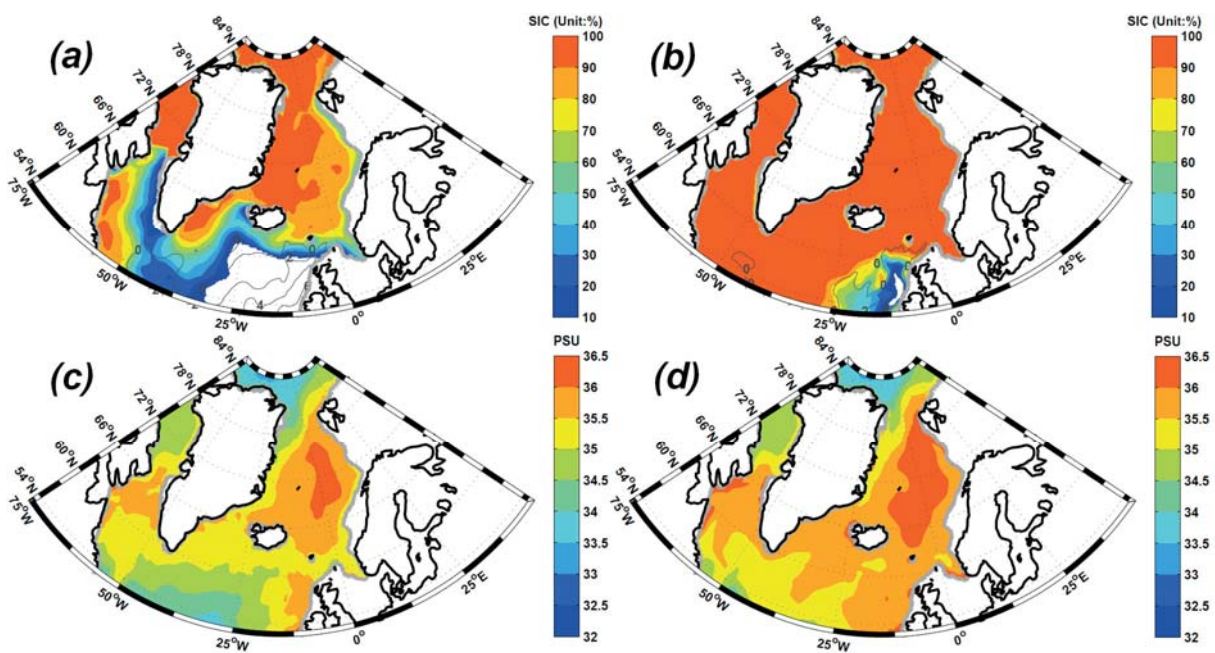


Figure 5.17. The simulated SST, SIC (upper row) and SSS (lower row) in our NAOSIM-C-3/2PSI experiment. Summer and winter seasons are shown in the left and right columns, respectively.

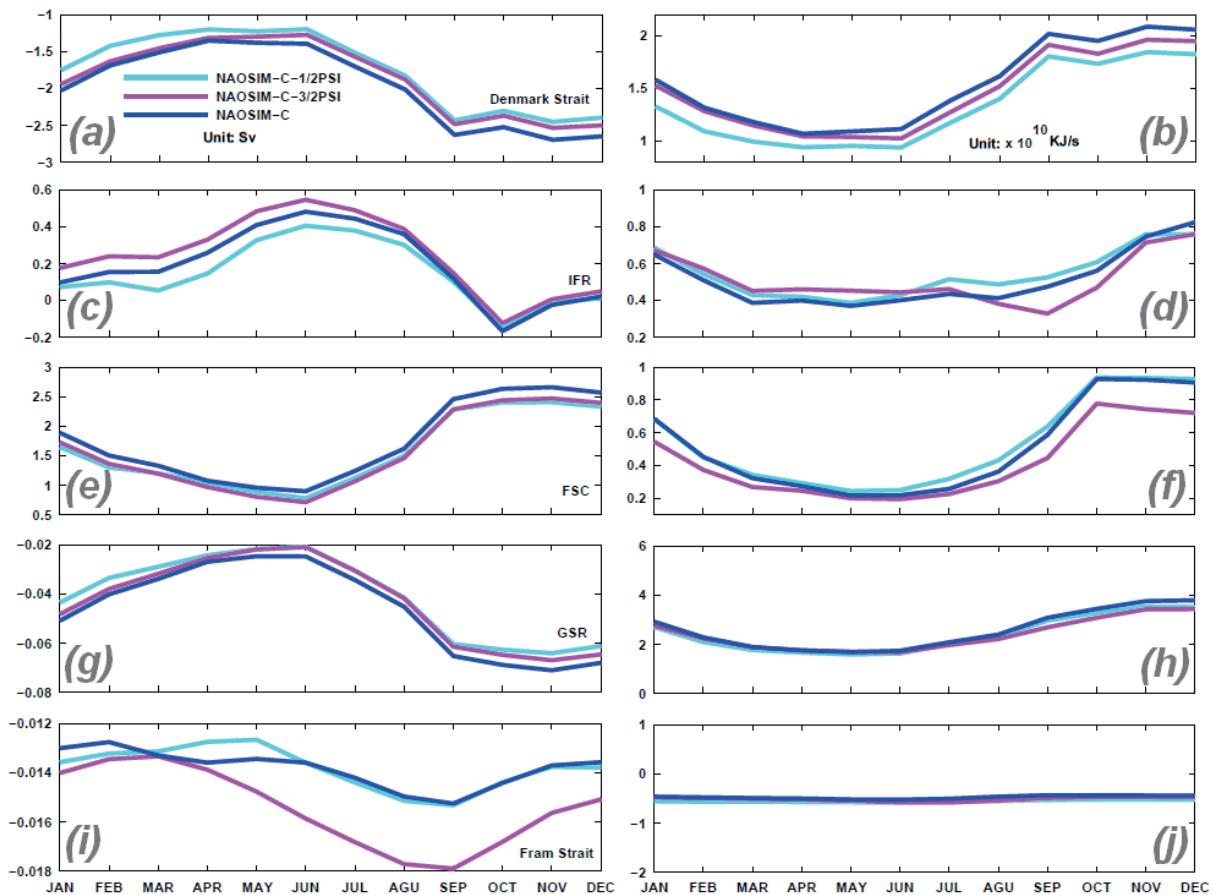


Figure 5.18. The seasonal cycle of water (left column) and heat transport (right column) across various ocean gateways (IFR: Iceland-Faroe Ridge, FSC: Faroe-Scotland Channel, GSR: Greenland-Scotland Ridge) in the NAOSIM-C, NAOSIM-C-1/2PSI and NAOSIM-C-3/2PSI experiments. The northward water and heat fluxes are exhibited with positive values.

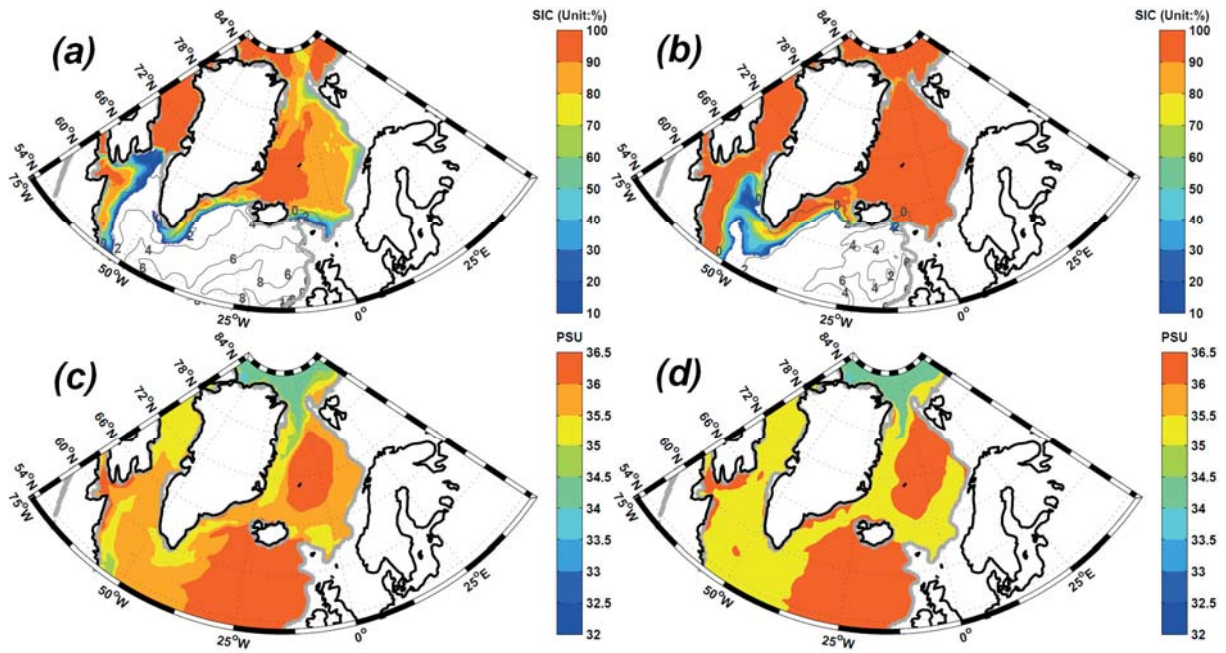


Figure 5.19. The simulated SST, SIC (upper row) and SSS (lower row) in our NAOSIM-C-gtway experiment. Summer and winter seasons are shown in the left and right columns, respectively.

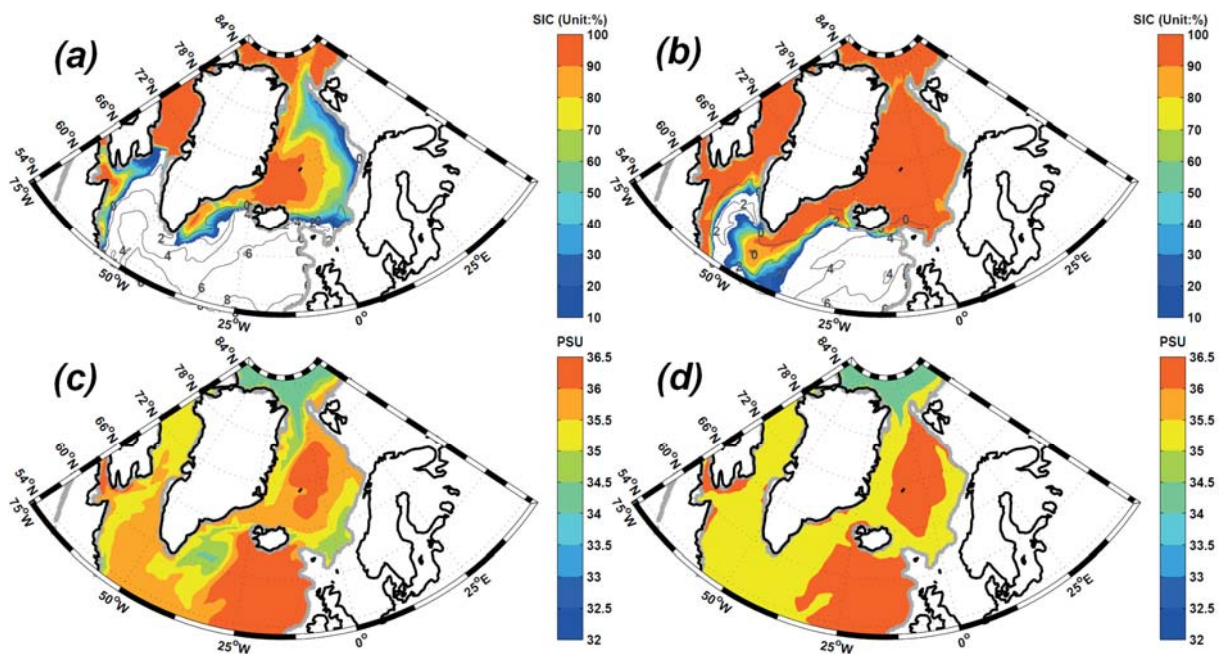


Figure 5.20. The simulated SST, SIC (upper row) and SSS (lower row) in our NAOSIM-G-gtway experiment. Summer and winter seasons are shown in the left and right columns, respectively.

### **5.3 NAOSIM discovered hydrographic features of the surface Nordic Seas during the LGM**

By conducting the experiments using different atmospheric forcing with respect to the CLIAMP and GLAMAP, we detect their distinctive surface ocean conditions in the Nordic Seas, aiming to a further understanding of underlying dynamics indicated by proxies.

Our experiments rediscovered spatial patterns of the SST and sea ice cover in the Nordic Seas during the LGM, which are generally in line with the CLIMAP and GLAMAP for the LGM, respectively. Compared to the totally sea ice covered summer Nordic Seas by CLIMAP, our NAOSIM-C experiment shows a gradual reduction of SIC from western (>90%) to eastern (~50%) part of the Nordic Seas during Summer. This west-eastwards summer sea ice change is not contrary to the proxy reconstruction, but it is not able to be calibrated by the proxies applied in CLIMAP. In addition, the choice of method used for mapping the original scattered distributed proxy data could also induce differences for the under-sampled regions [Paul and Mulitza, 2009]. Overall, our NAOSIM-C experiment points out the existence of noticeable seasonality of sea ice cover under the CLIMAP indicated surface atmosphere conditions. Furthermore, our NAOSIM-G experiment shows relatively more summer sea ice cover in the eastern part of Nordic Seas, which is accompanied by a significantly sea ice melting in the southeastern part of Nordic Seas and noticeable sea ice growth in the northeastern part of the Nordic Seas. Part of the freshwater from sea ice melting in the southeastern part of Nordic

Seas is northwards transported by the Norwegian Current, and subsequently leads to the more summer sea ice cover in the central and eastern part of Nordic Seas. Especially, the GLAMAP induced summer surface winds have a positive feedback to encourage this recirculation of sea ice melting water. Overall, our NAOSIM-G experiment shows a colder surface ocean of the Nordic Seas in summer than the GLAMAP, whereas the NAOSIM-C experiment exhibits a less summer sea ice cover than winter. These two experiments points out an intermediate cooling summer surface conditions and seasonality in the Nordic Seas between CLIMAP and GLAMAP, by supplying additional details of SSTs and sea ice cover.

Moreover, the SSS and surface oceanic circulations in our NAOSIM-C and NAOSIM-G experiments are different from PI experiments, but more comparable with each other. In both NAOSIM-C and NAOSIM-C experiments, the directions of surface oceanic circulation in the Nordic Seas are closely related to surface density change. Additionally, the Nordic Seas surface density shows similar spatial patterns with the SSS during the LGM, rather than the SST. Nevertheless, the differences in surface winds between the NAOSIM-C and NAOSIM-G experiment can lead to changes in the speed of surface ocean currents. In the NAOSIM-G experiments, the northward summer surface winds have a positive effect on the Norwegian Current, where is free of sea ice in summer. This could be a reason for the stronger ocean circulation in our NAOSIM-G experiment than that in the NAOISM-C experiment. In addition, these northward surface winds discourage the southward expansion of sea ice export in summer, and reversely encourage the North Atlantic inflow. This process leads to the area of sea ice melting in higher latitudes, i.e. surrounding the Faroe Island in our NAOSIM-G experiment. Subsequently, this sea ice melting water is partially northward transported, and results in a shrinking of the area with high SSSs in the central and eastern part of the Nordic Seas. As shown in Figure 5.21, the above hydrographic features and sea ice variations are not

able to be shown in our COSMOS model, resulting from its low resolution. These differences between NAOSIM and COSMOS emphasize the advantage of the usage of high-resolution ocean model in the aim of data-model intercomparison.

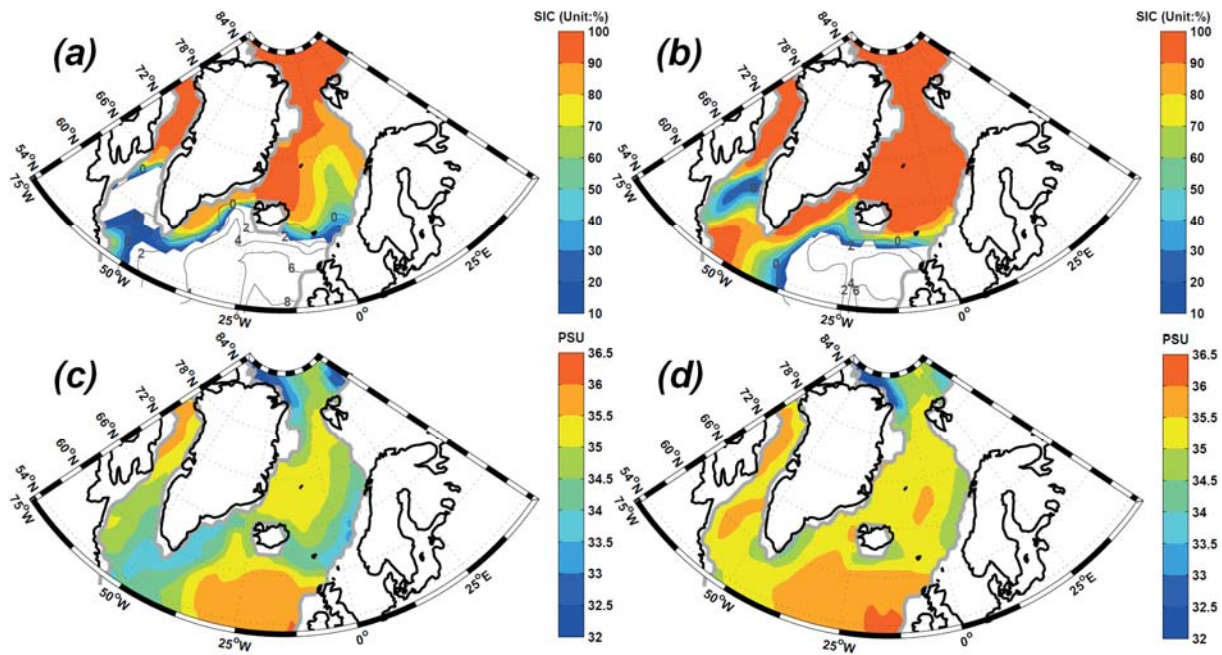


Figure 5.21. The simulated SST, SIC (upper row) and SSS (lower row) in our COSMOS LGM experiment. Summer and winter seasons are shown in the left and right columns, respectively.

Our finding is in line with the conclusions of project of Multiproxy Approach for the Reconstruction of the Glacial Ocean surface (MARGO), which is a proxy study involving the CLIMAP, GLAMAP samples and even more (Figure 5.22). Commonly, MARGO reconstructed a relatively colder surface condition than the GLAMAP, which is more similar to the CLIMAP in the Nordic Sea, but a lower sea ice cover during glacial summer season [MARGO Project Members, 2005]. Additionally, Meland et al. [2005] use planktic foraminifer as an indicator, and suggest less sea ice cover in the Nordic Seas than the

CLIMAP reconstruction, at the same time which is accompanied by more dynamic-complex oceanic circulations (Figure 5.23). In addition, our results also discover detailed features of SSS and surface oceanic circulation in the Nordic Sea. It is described that the variations of spatial salinity patterns dominant the directions of surface ocean currents, under both the CLIMAP and GLAMAP atmospheric forcing. However, the relatively stronger velocities in the GLAMAP corresponding experiment is due to positive effect of surface wind driven, especially in summer. Moreover, the high resolution feature of NAOSIM induces the capability of our results to provide a better understanding of the hydrographic processes at ocean gateways, which is not able to be detected in the ESMs, e.g. the Fram Strait and the GSR oceanic area. The seasonality of the sea ice cover in the eastern part of the Fram Strait is illustrated by Müller et al. [2009], which can be attributed to summer-winter difference in the Norwegian Current due to the change of surface wind direction that is more pronounced in our NAOSIM-G experiment. According to the study of proxies by Rasmussen and Thomsen [2008], three significantly visible features of the oceanic circulations in the Nordic Seas are mentioned (Figure 5.24):

- (i) The Atlantic inflow can at least reach  $76^{\circ}\text{N}$ , which is better proved by our GLAMAP corresponding experiment that the surface North Atlantic water is more efficiently transported northwards till the southern margin of Svalbard with larger current speed.
- An instability of the inflow of Atlantic water is indicated by proxies, accompanying similar unstable conditions both to the north and south of the GSR.
- (iii) The ocean north to Faroe Island is affected by sea ice melting water.

In the experiment with GLAMAP corresponding atmospheric forcing, sea ice edges have strong seasonal variations at the GSR, which shifts more southwards in winter than summer.

Additionally, the freshwater from sea ice melting can perturb the signals in proxy records at the sea ice edge area.

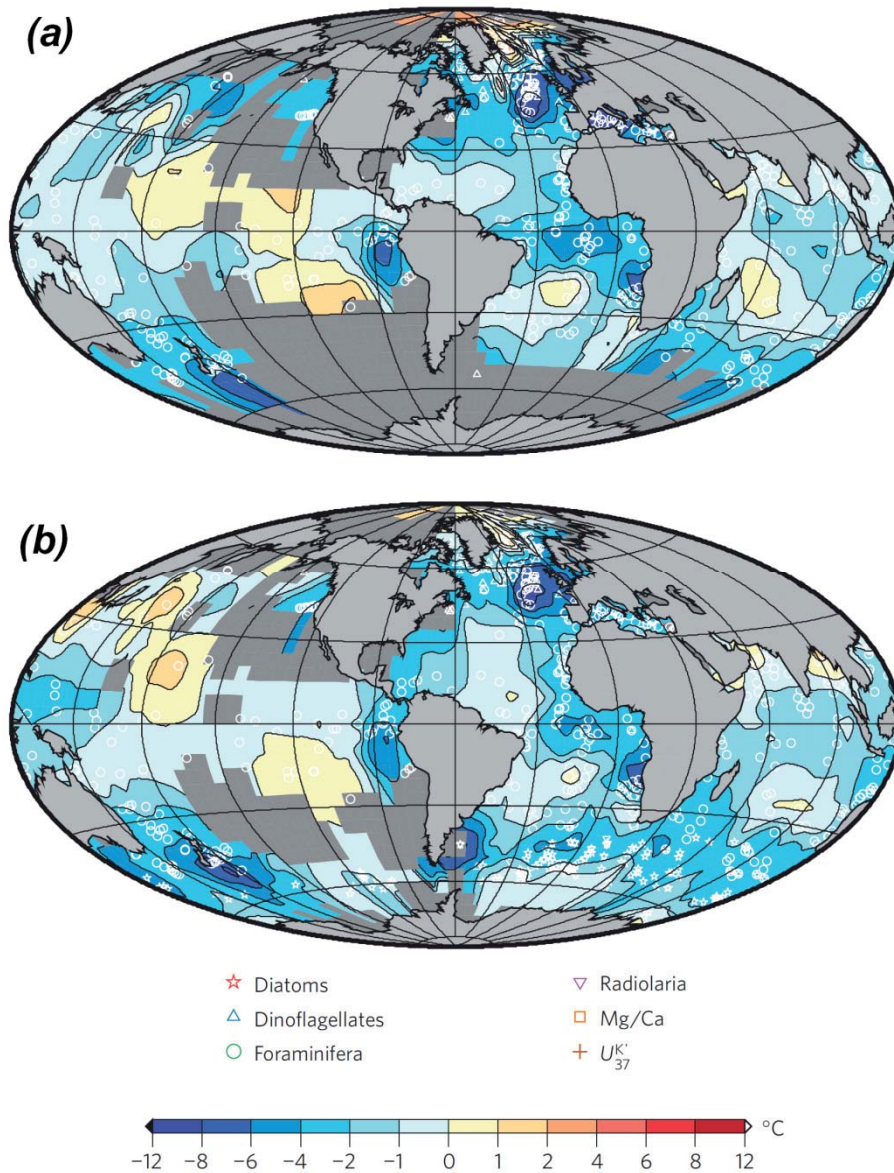


Figure 5.22. The Maps of reconstructed LGM SST anomalies relative the PI by MARGO (after MARGO [2009]). (a) Northern Hemisphere summer (July–August–September), (b) Northern Hemisphere winter (January–February–March). The symbols show the location and proxy type of the original available data.

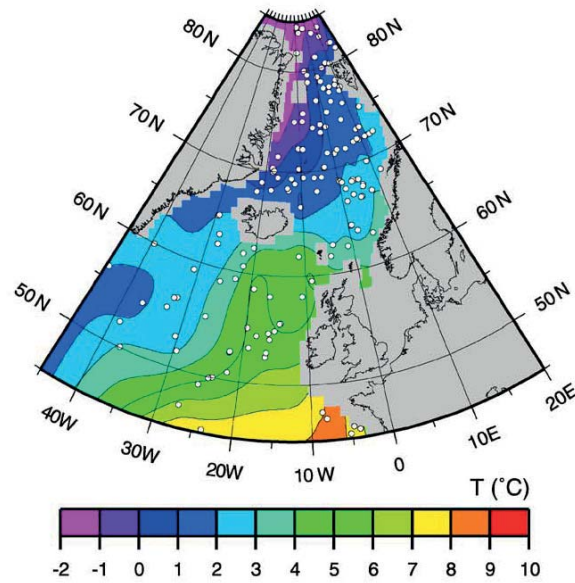


Figure 5.23. Summer SST reconstruction for the LGM (after Meland et al. [2005]).

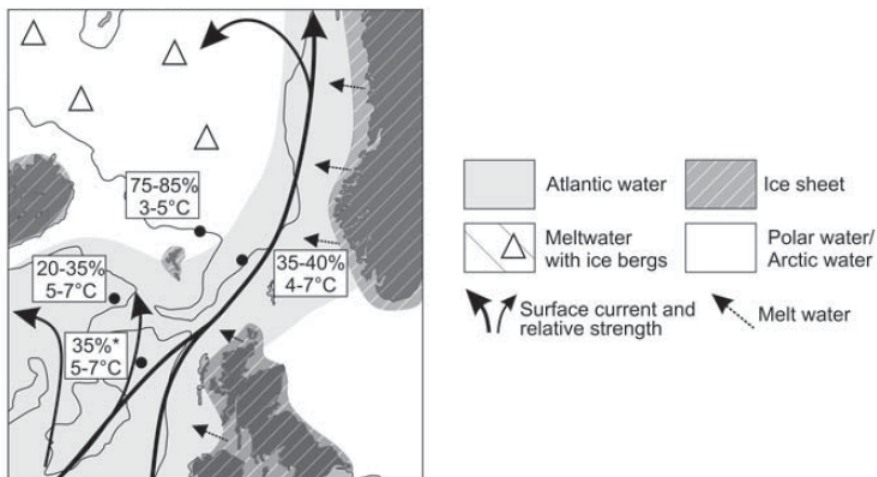


Figure 5.24. LGM summer sea surface temperatures and current systems in the northeastern Atlantic and southeastern Nordic seas (after Rasmussen and Thomsen [2008]).

## 5.4 What we learn from NAOSIM sensitivity study experiments

In total, we conducted three groups of sensitivity study experiments for sea surface salinity restoring (Chapter 5.2.4), stream function at open ocean boundary (Chapter 5.2.5) and the switch of the pathway of PD Norwegian Current (Chapter 5.2.6), respectively.

Our NAOSIM-C-sal experiment shows that internal dynamics in the Nordic Sea is independent on the salinity field, but the surface ocean conditions in northern North Atlantic Ocean are distinct when using PD or glacial restoring fields. Here, this sensitivity study for surface salinity restoring is complementary to Prange and Lohmann [2003, 2004] and Lohmann et al. [2005], since in their model setups, the salinity restoring was not necessary and they concentrated on the effect of the freshwater input only.

Furthermore, the experiments designed for diagnosing open ocean boundary (NAOSIM-C-1/2PSI and NAOSIM-C-3/2PSI) and ocean gateways (NAOSIM-C-gtway and NAOSIM-G-gtway) only show significant change in the northern North Atlantic Ocean (south to the GSR), but always similar SSTs and sea ice cover in the Nordic Seas. It is indicated that the northern North Atlantic Ocean is sensitive to both the water transport from lower latitudes, i.e. the stream function at 50°N open ocean boundary, also the outflow water and sea ice export from the Nordic Seas. In general, our findings of the intermediately cooling surface conditions and barotropic-dominated surface ocean circulations in the NAOSIM-G and NAOSIM-C experiments are robust features of the Nordic Seas during the LGM.

Additionally, we can learn from these sensitivity study experiments that various northern North Atlantic Ocean can be accompanied by a similar surface Nordic Seas during the LGM, which are more affected by the glacial surface air conditions. In the future study of past

Nordic Seas, the application of modeling work should be emphasized to gain more knowledge about the ‘ocean-atmosphere’ system.

## **5.5 Messages from NAOSIM experiments for the LGM**

- (i) The Nordic Seas have intermediate cooling surface conditions between the CLIMAP and GLAMAP reconstructions, with seasonal sea ice cover in the eastern part of the Nordic Seas.
- (ii) The surface ocean currents in the Nordic Seas show similar directions during the LGM, which are determined by the common spatial features of SSS of the Nordic Seas under CLIMAP and GLAMAP indicated atmospheric forcing.
- (iii) The above two features of the Nordic Seas during the LGM are robust, which are not related to our choices in surface salinity restoring and water transport at open ocean boundary of NAOSIM.

## 6 Conclusions and future perspectives

In this PhD study, we apply COSMOS model to untangling the effect of elevated northern hemisphere ice sheets to the North Atlantic Ocean surface circulation and AMOC during glacial climate periods. In addition, the COSMOS model is also used to explain the different spatial and temporal features of abrupt climate changes during the last glacial and interglacial cycle. Using the high-resolution NAOSIM model, we make further understanding of the sea surface conditions and underlying physical processes of CLIMAP and GLAMAP.

Proxies studies illustrates that the North Atlantic Ocean circulation and AMOC are different between glacial and interglacial climate states, and closely related with climate variations [e.g. CLIMAP, 1981; Slowey and Curry, 1992; de Vernal et al., 2002; Pflaumann, et al., 2003; McManus et al., 2004; Vautravers et al., 2004; Van Meerbeeck et al., 2009]. Base on previous mechanism study [Munk and Palmen, 1950; Rhines and Schopp, 1991] and climate modeling work [Pausata et al., 2011], we assume that the higher elevation of glacial ice sheet can lead to the changes of the North Atlantic Ocean circulation and AMOC during glacial climate. Using COSMOS model to simulate five different climate states, we found that the existence of the Laurentide Ice Sheet and higher elevation of Greenland Ice Sheet during glacial climate periods lead to stronger surface winds over the subtropical and subpolar North Atlantic Ocean than those during interglacial periods. Subsequently, the stronger surface winds during the glacial result in the intensification of the North Atlantic gyres and the Gulf Stream. Furthermore, a larger sea level gradient between the subtropical and subpolar North Atlantic Ocean results in a northward surface flow, which may provide a positive feedback on AMOC intensification. Furthermore, our results show that the pathway of the Gulf Stream is shifted

offshore due to anomalous eastward winds induced by the existence of Laurentide Ice Sheet during the glacial periods (Chapter 3).

Greenland ice cores show different features of abrupt decadal climate changes during the last glacial-interglacial cycle, which are less pronounced during maximum glacial conditions and strongly suppressed during the Holocene [Dansgaard et al., 1993]. Additionally, the records of sedimentary nutrient proxy evidence and kinematic proxies indicate a notable correlation of abrupt climate changes and variations in the Atlantic meridional overturning circulation (AMOC) [e.g. McManus et al., 2004; Thornalley et al., 2011]. Therefore, we conduct hosing experiments for the climate state of PI, 32 ka B.P. and LGM, towards aiming to explain these different features of abrupt decadal climate changes during the last glacial-interglacial cycle. Our results show that the freshening of the surface North Atlantic Ocean can lead to a similar AMOC reduction after 150 years freshwater perturbation, whereas the subsequent recovery stages exhibit distinct tempo-spatial characteristics, with respect to the initial AMOC resumption and the strength of a superposed AMOC overshoot. According to our mechanism analysis, the temperature inversion between the surface and intermediate layer in the South Labrador Sea induces a rapid restart of convective processes during the initial AMOC resumption, which is different in each experiment (32ka B.P. > LGM > PI). A few decades later, an AMOC overshoot is caused by the advection of warmer and saltier tropical Atlantic Ocean water into the South Labrador Sea. Only during glacial periods, the combined effect of the tropical Atlantic Ocean and the South Labrador Sea is response to the overshoot dynamics. In comparison to the 32ka B.P. experiment, this mechanism is noticeably weaker during the LGM, and completely absent during the PI (Chapter 4).

For the Nordic Seas during the LGM, GLAMAP and CLIMAP show extremely different surface conditions [CLIMAP, 1981; Pflaumann, et al. 2003]. Additionally, various ESMs

exhibit large spreads of simulation in the glacial Nordic Seas. Therefore, we use the high-resolution ocean model for a better understanding of the Nordic Seas surface conditions during the LGM. Using the atmosphere forcing corresponding to GLAMAP and CLIMAP, our NAOSIM experiments successfully reveal the large-scale properties of surface conditions in the Nordic Seas, which are in agreement with proxy reconstructions. Furthermore, the modeling study uncovers additional details of surface water properties and associated oceanic circulation. In these two experiments, the difference of surface ocean conditions between the CLIMAP and GLAMAP is less pronounced, accompanied by an intermediate seasonality. In addition, in spite of distinct features of simulated SSTs and sea ice cover, both of the experiments with the GLAMAP and CLAIMAP atmospheric forcing point out comparable surface ocean circulation of the Nordic Seas during the LGM. Moreover, additional sensitivity experiments prove that the choice of surface salinity resorting and open ocean boundary has insignificant effect to our findings. Therefore, our high-resolution NAOSIM simulations overcome the drawbacks of the ESM in presenting the LGM Nordic Seas circulation, and provide further understanding of the underlying physical processes (Chapter 5).

Overall, our results show that the variations of the North Atlantic Ocean during the last glacial-interglacial cycle are dependent on the background climatic states, observed over various spatial and temporal scales. Based on the investigations in Chapter 3-5, future work can be continued in the following directions:

In the work of Chapter 3, the correlation between the North Atlantic gyres and surface winds during glacial climate period has been shown stronger than during glacial climate periods. In the following, our study can be continued by further isolating the atmospheric and oceanic

effect to the North Atlantic surface ocean circulation base on different background climatic states, and their roles in northward heat transport (Chapter 3).

The property variations of the intermediate-layer tropical Atlantic Ocean water have been observed during the process of AMOC reductions. However, the underlying mechanism related to this variation is still not explained. This may result from the ventilation change in the tropical Atlantic Ocean, or an advection from the southern part of the Atlantic Ocean. Further analysis is recommended in this direction. In addition, many other studies present an alternative role of the Nordic Seas response to abrupt decadal climate changes of AMOC. Oka et al. [2012] illustrates a potential thermal threshold for the AMOC variation, which is model-dependent. Therefore, further diagnosis may be done in order to compare our results with other ESMs and proxies (Chapter 4).

Currently, ESM has difficulties in assessing proxy-indicated past oceans, cause of its too low resolution for the complexity of oceanic circulation. In Chapter 5, our high-resolution regional ocean model overcomes this drawback, and has successfully rediscovered the features of past oceans, in agreement with proxy reconstruction. However, this high-resolution regional ocean model lacks both atmosphere-ocean feedbacks and global climate feedbacks. Here, our approach provides a future perspective for the combination of using ESM and high-resolution regional ocean model in diagnosing paleo ocean circulation. Using multi-year surface atmospheric forcing, which are simulated for a past climate regime in ESM (with coupled atmosphere-ocean system), the high-resolution regional ocean model can be used to gain detailed physical processes in the ocean, which results are in fine resolutions for the intercomparison with the proxy data. In general, the combination of using ESM and high-resolution regional ocean model can encourage the linking of proxy data and models, and favors a better understanding of past oceans (Chapter 5).

In summary, our modeling work further explores the underlying dynamics of the North Atlantic climate system during the last glacial-interglacial cycle. Future research on processes within climate models can help us develop the knowledge of the climate system.

## 7 Reference

- Aagaard, K., E.C. Carmack (1989), The Role of Sea Ice and Other Fresh Water in the Arctic Circulation. *J. Geophys. Res. (C10)*, 14485–14498.
- Aitken, M. J. (1997), Luminescence dating, in Taylor, R. E. and M. J. Aitken (eds.), *Chronometric Dating in Archaeology, Advances in Archaeological and Museum Science Series, Vol. 2*, Plenum, New York.
- Arkipov, S.A., L. L. Isayeva, V. G. Bespaly, O. Glushkova (1986), Glaciation of Siberia and north-east USSR. *Quaternary Science Reviews* (0), 463-474.
- Backeberg, B. C., P. Penven, and M. Rouault (2012), Impact of intensified Indian Ocean winds on mesoscale variability in the Agulhas system, *Nat Clim Change*, 2(8), 608-612.
- Barker, S., G. Knorr, M. J. Vautravers, P. Diz, and L. C. Skinner (2010), Extreme deepening of the Atlantic overturning circulation during deglaciation, *Nat Geosci*, 3(8), 567-571.
- Berger, A. L. (1978), Long-Term Variations of Daily Insolation and Quaternary climatic Changes, *J Atmos Sci*, 35(12), 2362-2367.
- Bjerknes, J. (1969), Atmospheric teleconnections from the equatorial Pacific. *Mon. Weather Rev.*, 97, 163-172.
- Braconnot, P., B. Otto-Bliesner, S. Harrison, S. Joussaume, J.-Y. Peterchmitt, A. Abe-Ouchi, M. Crucifix, E. Driesschaert, Th. Fichefet, C. D. Hewitt, M. Kageyama, A. Kitoh, M.-F. Loutre, O. Marti, U. Merkel, G. Ramstein, P. Valdes, L. Weber, Y. Yu, and Y. Zhao (2007), Results of PMIP2 coupled simulations of the Mid-Holocene and Last Glacial Maximum - Part 1: experiments and large-scale features, *Clim Past*, 3(2), 261-277.

Brook, E. J., S. Harder, J. Severinghaus, E. J. Steig, and C. M. Sucher (2000), On the origin and timing of rapid changes in atmospheric methane during the last glacial period, *Global Biogeochem Cy*, 14(2), 559-572.

Brovkin, V., T. Raddatz, C. H. Reick, M. Claussen, and V. Gayler (2009), Global biogeophysical interactions between forest and climate, *Geophys. Res. Lett.*, 36, L07405, doi:10.1029/2009GL037543.

Bryan, F. (1986), High-Latitude Salinity Effects and Interhemispheric Thermohaline Circulations, *Nature*, 323(6086), 301-304.

Bryden, H. L., H. R. Longworth, and S. A. Cunningham (2005), Slowing of the Atlantic meridional overturning circulation at 25 degrees N, *Nature*, 438(7068), 655-657.

Burkholder, K. C., and M. S. Lozier (2011), Subtropical to subpolar pathways in the North Atlantic: Deductions from Lagrangian trajectories, *J Geophys Res-Oceans*, 116.

Butzin, M., M. Prange, and G. Lohmann (2005), Radiocarbon simulations for the glacial ocean: The effects of wind stress, Southern Ocean sea ice and Heinrich events, *Earth Planet Sc Lett*, 235(1-2), 45-61.

Cheng, J., Z. Liu, F. He, B. L. Otto-Bliesner, and C. Colose (2011), Impact of North Atlantic - Nordic Seas exchange on deglaciation evolution of the Atlantic Meridional Overturning Circulation, *Clim Past*, 7(3), 935-940.

Cianca, A., R. Santana, J. P. Marrero, M. J. Rueda and O. Llinás (2009), Modal composition of the central water in the North Atlantic subtropical gyre, *Ocean Sci. Discuss.*, 6, 2487-2506, doi:10.5194/osd-6-2487-2009.

Clark, P. U., A. S. Dyke, J. D. Shakun, A. E. Carlson, J. Clark, B. Wohlfarth, J. X. Mitrovica, S. W. Hostetler, and A. M. McCabe (2009), The Last Glacial Maximum, *Science*, 325(5941), 710-714.

CLIMAP Project Members (CLIMAP) (1981), Seasonal reconstructions of the Earth's surface at the Last Glacial Maximum, Map Chart Ser. MC-36, Geol. Soc. of Am., Boulder, Colo.

Crucifix, M., P. Braconnot, S. P. Harrison, and B. Otto-Bliesner (2005), Second phase of paleoclimate modelling intercomparison project, *Eos Trans. AGU*, 86(28), 264, doi:10.1029/2005EO280003.

Curry, R. G., and M. S. McCartney (2001), Ocean gyre circulation changes associated with the North Atlantic Oscillation, *J Phys Oceanogr*, 31(12), 3374-3400.

Dansgaard, W., S. J. Johnsen, H. B. Clausen, D. Dahl-Jensen, N. S. Gundestrup, C. U. Hammer, C., S. Hvidberg, J. P. Steffensen, A. E. Sveinbjörnsdottir, J. Jouzel and G. Bond (1993), Evidence for General Instability of Past Climate from a 250-Kyr Ice-Core Record, *Nature*, 364(6434), 218-220.

Delmas, R. J., J. M. Ascencio, and M. Legrand (1980), Polar Ice Evidence That Atmospheric Co<sub>2</sub> 20,000-Yr Bp Was 50-Percent of Present, *Nature*, 284(5752), 155-157.

de Vernal, A., C. Hillaire-Marcel, W. R. Peltier, and A. J. Weaver (2002), Structure of the upper water column in the northwest North Atlantic: Modern versus last glacial maximum conditions, *Paleoceanography*, 17(4).

Drange, H., R. Gerdes, Y. Gao, M. Karcher, F. Kauker, and M. Bentsen (2005), Ocean General Circulation Modelling of the Nordic Seas, in *The Nordic Seas: An Integrated Perspective*, H. Drange, T. Dokken, T. Furevik, R. Gerdes, and W. Berger (eds.), AGU Monograph 158, American Geophysical Union, Washington DC, pp. 199-220.

Dzhiganshin, G. F. and A. B. Polonsky (2009), Low-frequency variations of the Gulf-Stream transport: description and mechanisms, *Physical oceanography*, Vol. 19, No. 3, p. 151-169, doi: 10.1007/s11110-009-9047-5.

- Eddy, J. A. (1976), The Maunder Minimum, *Science*, 192, 1189-1202, doi:10.1126/science.192.4245.1189.
- Ehlers, J., and P. L. Gibbard (2007), The extent and chronology of Cenozoic Global Glaciation. *Quaternary Int.*, 6–20.
- Furevik, T., M. Bentsen, H. Drange, J. A. Johannessen, and A. Korabely (2002), Temporal and spatial variability of the sea surface salinity in the Nordic Seas, *J. Geophys. Res.*, 107(C12), 8009, doi:10.1029/2001JC001118.
- Fronval, T., and E. Jansen (1996), Rapid changes in ocean circulation and heat flux In the Nordic seas during the last interglacial period, *Nature*, 383(6603), 806-810.
- Ganopolski, A., and S. Rahmstorf (2001), Rapid changes of glacial climate simulated in a coupled climate model, *Nature*, 409(6817), 153-158.
- Gerdes, R., C. Koeberle, and J. Willebrand (1991), The influence of numerical advection schemes on the results of ocean general circulation models, *Clim. Dyn.*, 5, 211-226.
- Hagemann, S., and L. Dumenil (1998), A parametrization of the lateral waterflow for the global scale, *Clim Dynam*, 14(1), 17-31.
- Hass, H. C. (1996), Northern Europe climate variations during late Holocene: Evidence from marine Skagerrak, *Palaeogeogr Palaeoclimatol*, 123(1-4), 121-145.
- Häkkinen, S., and P. B. Rhines (2004), Decline of subpolar North Atlantic circulation during the 1990s, *Science*, 304(5670), 555-559.
- Häkkinen, S., and P. B. Rhines (2009), Shifting surface currents in the northern North Atlantic Ocean, *J Geophys Res-Oceans*, 114.
- Hemming, S. R. (2004), Heinrich events: Massive late Pleistocene detritus layers of the North Atlantic and their global climate imprint, *Rev. Geophys.*, 42, RG1005, doi:10.1029/2003RG000128.

- Hesse, T., M. Butzin, T. Bickert, and G. Lohmann (2011), A model-data comparison of delta C-13 in the glacial Atlantic Ocean, *Paleoceanography*, 26.
- Hibler, W. D. (1979), Dynamic Thermodynamic Sea Ice Model, *J Phys Oceanogr*, 9(4), 815-846.
- Hofmann, M., and S. Rahmstorf (2009), On the stability of the Atlantic meridional overturning circulation, *P Natl Acad Sci USA*, 106(49), 20584-20589.
- Hogg, N.G., and W.E. Johns (1995), Western boundary currents, U.S. National Report to International Union of Geodesy and Geophysics 1991-1994, Supplement to Reviews of Geophysics, 33, 1311-1334.
- Hu, A. X., B. L. Otto-Bliesner, G. A. Meehl, W. Q. Han, C. Morrill, E. C. Brady, and B. Briegleb (2008), Response of thermohaline circulation to freshwater forcing under present-day and LGM conditions, *J Climate*, 21(10), 2239-2258.
- Hubberten, H.W., A. Andreev, V.I. Astakhov, I. Demidov, J. A. Dowdeswell, M. Henriksen, C. Hjort, M. Houmark-Nielsen, M. Jakobsson, S. Kuzmina, E. Larsen, J. P. Lunkka, A. Lyså, J. Mangerud, P. Möller, M. Saarnisto, L. Schirmer, A. V. Sher, C. Siegert, M. J. Siegert, J. I. Svendsen (2004), The periglacial climate and environment in northern Eurasia during the Last Glaciation, *Quaternary Sci. Rev.* (11-13), 1333-1357.
- Huber, C., M. Leuenberger, R. Spahni, J. Fluckiger, J. Schwander, T. F. Stocker, S. Johnsen, A. Landals, and J. Jouzel (2006), Isotope calibrated Greenland temperature record over Marine Isotope Stage 3 and its relation to CH<sub>4</sub>, *Earth Planet Sc Lett*, 243(3-4), 504-519.
- Indermühle, A., T. F. Stocker, F. Joos, H. Fischer, H. J. Smith, M. Wahlen, B. Deck, D. Mastroianni, J. Tschumi, T. Blunier, R. Meyer, and B. Stauffer (1999), Holocene carbon-cycle dynamics based on CO<sub>2</sub> trapped in ice at Taylor Dome, Antarctica, *Nature*, 398(6723), 121-126.

Kalnay, E., Kanamitsu, M., Kistler, R., Collins, W., Deaven, D., Gandin, L., Iredell, M., Saha, S., White, G., Woollen, J., Zhu, Y., Leetmaa, A., Reynolds, R., Chelliah, M., Ebisuzaki, W., Higgins, W., Janowiak, J., Mo, K.C., Ropelewski, C., Wang, J., Jenne, R., Joseph, D., 1996. The NCEP/NCAR 40-Year Reanalysis Project. *Bull. Am. Meteorol. Soc.* (3), 437–471.

Kauker, F., R. Gerdes, M. Karcher, C. Koberle, and J. L. Lieser (2003), Variability of Arctic and North Atlantic sea ice: A combined analysis of model results and observations from 1978 to 2001, *J Geophys Res-Oceans*, 108(C6).

Kauker, F., Gerdes, R., Karcher, M., Köberle, C. (2005), Impact of North Atlantic Current changes on the Nordic Seas and the Arctic Ocean. *J. Geophys. Res* (C12), C12002.

Kauker, F., Kaminski, T., Karcher, M., Giering, R., Gerdes, R., and M. Voßbeck (2009), Adjoint analysis of the 2007 all time Arctic sea-ice minimum. *Geophys. Res. Lett.* (3), L03707.

Keigwin, L. D., W. B. Curry, S. J. Lehman, and S. Johnsen (1994), The Role of the Deep-Ocean in North-Atlantic Climate-Change between 70-Kyr and 130-Kyr Ago, *Nature*, 371(6495), 323-326.

Kleinen, T., T. J. Osborn, and K. R. Briffa (2009), Sensitivity of climate response to variations in freshwater hosing location, *Ocean Dynam*, 59(3), 509-521.

Knorr, G., and G. Lohmann (2007), Rapid transitions in the Atlantic thermohaline circulation triggered by global warming and meltwater during the last deglaciation, *Geochem Geophys Geosy*, 8., doi: 10.1029/2007GC001604.

Knorr, G., M. Butzin, A. Micheels, and G. Lohmann (2011), A warm Miocene climate at low atmospheric CO<sub>2</sub> levels, *Geophys Res Lett*, 38., doi:10.1029/2011GL048873.

Köberle, C., and R. Gerdes (2003), Mechanisms Determining the Variability of Arctic Sea Ice Conditions and Export, *J. Climate*, 16, 2843–2858.

Köhl, A., R. H. Kase, D. Stammer, and N. Serra (2007), Causes of changes in the Denmark strait overflow, *J Phys Oceanogr*, 37(6), 1678-1696.

Köhler, P., G. Knorr, D. Buiron, A. Lourantou, and J. Chappellaz (2011), Abrupt rise in atmospheric CO<sub>2</sub> at the onset of the Bolling/Allerod: in-situ ice core data versus true atmospheric signals, *Clim Past*, 7(2), 473-486.

Kösters, F., R. H. Kase, A. Schmittner, and P. Herrmann (2005), The effect of Denmark strait overflow on the Atlantic meridional overturning circulation, *Geophys Res Lett*, 32(4).

Kuijpers, A., S. R. Troelstra, M. Wisse, S. H. Nielsen, and T. C. E. van Weering (1998), Norwegian Sea overflow variability and NE Atlantic surface hydrography during the past 150,000 years, *Mar Geol*, 152(1-3), 75-99.

Laskar, J., P. Robutel, F. Joutel, M. Gastineau, A. C. M. Correia, and B. Levrard (2004), A long-term numerical solution for the insolation quantities of the Earth, *Astron Astrophys*, 428(1), 261-285.

LeGrande, A. N., and G. A. Schmidt (2009), Sources of Holocene variability of oxygen isotopes in paleoclimate archives, *Clim Past*, 5(3), 441-455.

Levitus, S. (1982), *Climatological Atlas of the World Ocean*, NOAA/ERL GFDL Professional Paper 13, Princeton, N.J., 173 pp. (NTISPB83-184093).

Liu, Z., Otto-bliesner, B.L., He, F., Brady, E.C., Tomas, R., Clark, P.U., Carlson, A.E., Lynch-stieglitz, J., Curry, W., Brook, E., Erickson, D., Jacob, R., Kutzbach, J., Cheng, J. (2009), Transient Simulation of Last Deglaciation with a New Mechanism for Bolling-Allerod Warming, *Science*, 325(5938), 310-314.

Lohmann, G., and S. Lorenz (2000), On the hydrological cycle under paleoclimatic conditions as derived from AGCM simulations, *J Geophys Res-Atmos*, 105(D13), 17417-17436.

Lohmann, G., S. J. Lorenz, and M. Prange (2005), Northern high-latitude climate changes during the Holocene as simulated by circulation models, in *The Nordic Seas: An Integrated Perspective*, H. Drange, T. Dokken, T. Furevik, R. Gerdes, and W. Berger (eds.), Geophysical Monograph 158, American Geophysical Union, Washington, DC, pp. 273-288. doi:10.1029/158GM18.

Lüthi, D., M. L. Floch, B. Bereiter, T. Blunier, J. Barnola, U. Siegenthaler, D. Raynaud, J. Jouzel, H. Fischer, K. Kawamura, and T. F. Stocker (2008), High-resolution carbon dioxide concentration record 650,000 - 800,000 years before present. *Nature*, 453, 379-382, doi:10.1038/nature06949.

Lynch-Stieglitz, J. (2001), Using ocean margin density to constrain ocean circulation and surface wind strength in the past, *Geochem Geophys Geosy*, 2, doi: 10.1029/2001GC000208.

Lynch-Stieglitz, J., W. B. Curry, and D. C. Lund (2009), Florida Straits density structure and transport over the last 8000 years, *Paleoceanography*, 24.

Lynch-Stieglitz, J., W. B. Curry, and N. Slowey (1999), Weaker Gulf Stream in the Florida straits during the last glacial maximum, *Nature*, 402(6762), 644-648.

MARGO Project Members (2009), Constraints on the magnitude and patterns of ocean cooling at the Last Glacial Maximum, *Nature Geoscience* 2, 127 – 132, doi:10.1038/ngeo411.

Marshall, J., H. Johnson, and J. Goodman (2001), A study of the interaction of the North Atlantic oscillation with ocean circulation, *J Climate*, 14(7), 1399-1421.

Marsland, S. J., H. Haak, J. H. Jungclaus, M. Latif, and F. Roske (2003), The Max-Planck-Institute global ocean/sea ice model with orthogonal curvilinear coordinates, *Ocean Model*, 5(2), 91-127.

Maslin, M. A., and B. Christensen (2007), Tectonics, orbital forcing, global climate change, and human evolution in Africa: introduction to the African paleoclimate special volume, *J Hum Evol*, 53(5), 443-464.

McManus, J. F., R. Francois, J. M. Gherardi, L. D. Keigwin, and S. Brown-Leger (2004), Collapse and rapid resumption of Atlantic meridional circulation linked to deglacial climate changes, *Nature*, 428(6985), 834-837.

Meland, M. Y. and Jansen, E. and H. Elderfield (2005), Constraints on SST estimates for the northern North Atlantic/Nordic Seas during the LGM. *Quaternary Science Reviews*, 24 (7-9), pp. 835-852.

Mignot, J., A. Ganopolski, and A. Levermann (2007), Atlantic subsurface temperatures: Response to a shutdown of the overturning circulation and consequences for its recovery, *J Climate*, 20(19), 4884-4898.

Milankovitch M. (1920), *Théorie Mathématique des Phénomènes Produits par la Radiation Solaire*, Gauthier-Villars, Paris.

Montoya, M., and A. Levermann (2008), Surface wind-stress threshold for glacial Atlantic overturning, *Geophys Res Lett*, 35(3).

Munk, W. H. and E. Palmén (1951), Note on the dynamics of the Antarctic Circumpolar Current, *Tellus*, 3(1), 53–55, doi: 10.1111/j.2153-3490.1951.tb00776.x.

Müller, J., G. Masse, R. Stein, and S. T. Belt (2009), Variability of sea-ice conditions in the Fram Strait over the past 30,000 years, *Nat Geosci*, 2(11), 772-776.

Neftel, A., H. Oeschger, J. Schwander, B. Stauffer, and R. Zumbunn (1982), Ice Core Sample Measurements Give Atmospheric Co<sub>2</sub> Content during the Past 40,000 Yr, *Nature*, 295(5846), 220-223.

North Greenland Ice Core Project Members (2004), High-resolution record of Northern Hemisphere climate extending into the last interglacial period, *Nature*, 431(7005), 147-151, doi:10.1038/nature02805.

Oka, A., H. Hasumi, and A. Abe-Ouchi (2012), The thermal threshold of the Atlantic meridional overturning circulation and its control by wind stress forcing during glacial climate, *Geophys Res Lett*, 39.

Oppo, D. W., L. D. Keigwin, J. F. McManus, and J. L. Cullen (2001), Persistent suborbital climate variability in marine isotope stage 5 and Termination II, *Paleoceanography*, 16(3), 280-292.

Otto-Bliesner, B. L., C. D. Hewitt, T. M. Marchitto, E. Brady, A. Abe-Ouchi, M. Crucifix, S. Murakami, and S. L. Weber (2007), Last Glacial Maximum ocean thermohaline circulation: PMIP2 model intercomparisons and data constraints, *Geophys Res Lett*, 34(12).

Otto-Bliesner, B. L., and E. C. Brady (2010), The sensitivity of the climate response to the magnitude and location of freshwater forcing: last glacial maximum experiments, *Quaternary Sci Rev*, 29(1-2), 56-73.

Overpeck, J. T., B. L. Otto-Bliesner, G. H. Miller, D. R. Muhs, R. B. Alley, and J. T. Kiehl (2006), Paleoclimatic evidence for future ice-sheet instability and rapid sea-level rise, *Science*, 311(5768), 1747-1750.

Pacanowski, R. C. (1995), MOM 2 Documentation, user's guide and reference manual, GFDL Ocean Group Tech. Rep.3, Geophys. Fluid Dyn. Lab., Princeton Univ., Princeton, N.J..

Paul, A., and C. Schäfer-Neth (2004), How to combine sparse proxy data and coupled climate models. *Quaternary Science Reviews*, doi:10.1016/j.quascirev.2004.05.010

Paul, A., and S. Mulitza (2009), Challenges to Understanding Ocean Circulation during the Last Glacial Maximum, *Eos Trans. AGU*, 90(19), 169.

Pausata, F. S. R., C. Li, J. J. Wettstein, M. Kageyama, and K. H. Nisancioglu (2011), The key role of topography in altering North Atlantic atmospheric circulation during the last glacial period, *Clim Past*, 7(4), 1089-1101.

Peltier, W. R. (2004), Global glacial isostasy and the surface of the ice-age earth: The ice-5G (VM2) model and grace, *Annu Rev Earth Pl Sc*, 32, 111-149.

Petit, J. R., J. Jouzel, D. Raynaud, N. I. Barkov, J.-M. Barnola, I. Basile, M. Bender, J. Chappellaz, M. Davis, G. Delaygue, M. Delmotte, V. M. Kotlyakov, M. Legrand, V. Y. Lipenkov, C. Lorius, L. PÉpin, C. Ritz, E. Saltzman and M. Stievenard (1999), Climate and atmospheric history of the past 420,000 years from the Vostok ice core, Antarctica, *Nature*, 399(6735), 429-436.

Pflaumann, U., M. Sarnthein, M. Chapman, L. d'Abreu, B. Funnell, M. Huels, T. Kiefer, M. Maslin, H. Schulz, J. Swallow, S. van Kreveld, M. Vautravers, E. Vogelsang, and M. Weinelt (2003), Glacial North Atlantic: Sea-surface conditions reconstructed by GLAMAP 2000, *Paleoceanography*, 18(3).

Prange, M., and G. Lohmann (2003), Effects of mid-Holocene river runoff on the Arctic ocean-sea ice system: a numerical study, *The Holocene* 13 (3), 335-342.

Prange, M., and G. Lohmann (2004), Variable freshwater input to the Arctic Ocean during the Holocene: Implications for large-scale ocean-sea ice dynamics as simulated by a circulation model. In *The Climate in Historical Times: Towards a synthesis of Holocene proxy data and climate models*, H. Fischer et al. (eds.), Springer-Verlag, pp. 319-335.

Prange, M., G. Lohmann, V. Romanova, and M. Butzin (2004), Modelling tempo-spatial signatures of Heinrich Events: Influence of the climatic background state. *Quat. Sci. Rev.*, 23/5-6, 521-527.

Raddatz, T. J., C. H. Reick, W. Knorr, J. Kattge, E. Roeckner, R. Schnur, K. G. Schnitzler, P. Wetzell, and J. Jungclaus (2007), Will the tropical land biosphere dominate the climate-carbon cycle feedback during the twenty-first century?, *Clim Dynam*, 29(6), 565-574.

Rahmstorf, S. (1996), On the freshwater forcing and transport of the Atlantic thermohaline circulation, *Clim Dynam*, 12(12), 799-811.

Rasmussen, T. L., and E. Thomsen (2008), Warm Atlantic surface water inflow to the Nordic seas 34-10 calibrated ka BP, *Paleoceanography*, 23(1).

Rattray, M. (1982), A Simple Exact Treatment of the Baroclinicity -Bathymetry Interaction in a Frictional, Iterative, Diagnostic Ocean Model, *J. Phys. Oceanogr.* 12, 997-1003.

Renold, M., C. C. Raible, M. Yoshimori, and T. F. Stocker (2010), Simulated resumption of the North Atlantic meridional overturning circulation - Slow basin-wide advection and abrupt local convection, *Quaternary Sci Rev*, 29(1-2), 101-112.

Rhines, P. B., and R. Schopp (1991), The Wind-Driven Circulation - Quasi-Geostrophic Simulations and Theory for Nonsymmetric Winds, *J Phys Oceanogr*, 21(9), 1438-1469.

Romanova, V., M. Prange, and G. Lohmann (2004), Stability of the glacial thermohaline circulation and its dependence on the background hydrological cycle. *Clim. Dynam.*, 527-538.

Röckner, E., G. Bäuml, L. Bonaventura, R. Brokopf, M. Esch, M. Giorgetta, S. Hagemann, I. Kirchner, L. Kornbluh, E. Manzini, A. Rhodin, U. Schlese, U. Schulzweida, and A. Tompkins (2003), The Atmospheric General Circulation Model ECHAM5. Part 1: Model description, MPI-Report 349, 127, MPI, Hamburg, Germany.

Rühlemann, C., S. Mulitza, G. Lohmann, A. Paul, M. Prange, and G. Wefer (2004), Intermediate depth warming in the tropical Atlantic related to weakened thermohaline

circulation: Combining paleoclimate data and modeling results for the last deglaciation, *Paleoceanography*, 19(1), PA1025, doi:10.1029/2003PA000948.

Sarkisyan, A. S., and V. F. Ivanov (1971), The combined effect of baroclinicity and bottom relief as an important factor in the dynamics of ocean current (AGU translation). *Izv. Acad. Sci. USSR, Atmos. Oceanic Physics.*, 173-188.

Scambos, T. A., C. Hulbe, M. Fahnestock, and J. Bohlander (2000), The link between climate warming and break-up of ice shelves in the Antarctic Peninsula, *J Glaciol*, 46(154), 516-530.

Semtner, A. J. (1976), A Model for the Thermodynamic Growth of Sea Ice in Numerical Investigations of Climate, *J. Phys. Oceanogr.*, 6, 379–389.

Shackleton, N. J., M. F. Sanchez-Goni, D. Pailler, and Y. Lancelot (2003), Marine Isotope Substage 5e and the Eemian interglacial, *Global Planet Change*, 36(3), 151-155.

Shakun, J. D., P. U. Clark, F. He, S. A. Marcott, A. C. Mix, Z. Y. Liu, B. Otto-Bliesner, A. Schmittner, and E. Bard (2012), Global warming preceded by increasing carbon dioxide concentrations during the last deglaciation, *Nature*, 484(7392), 49.

Shin, S.-I., Z. Liu, B. Otto-Bliesner, E. Brady, J. Kutzbach, and S. Harrison (2003), A Simulation of the Last Glacial Maximum climate using the NCAR-CCSM. *Clim. Dynam.* (20), 127–151.

Siegert, M.J., I. Marsiat (2001), Numerical reconstructions of LGM climate across the Eurasian Arctic. *Quaternary Sci. Rev.* (15), 1595-1605.

Siegert, M.J., J. A. Dowdeswell (2004), Numerical reconstructions of the Eurasian Ice Sheet and climate during the Late Weichselian. *Quaternary Sci. Rev.* (11-13), 1273-1283.

Skagseth, O. (2004), Monthly to annual variability of the Norwegian Atlantic slope current: connection between the northern North Atlantic and the Norwegian Sea, *Deep-Sea Res Pt I*, 51(3), 349-366.

Slowey, N. C., and W. B. Curry (1992), Enhanced Ventilation of the North-Atlantic Subtropical Gyre Thermocline during the Last Glaciation, *Nature*, 358(6388), 665-668.

Sowers, T., R. B. Alley, and J. Jubenville (2003), Ice core records of atmospheric N<sub>2</sub>O covering the last 106,000 years, *Science*, 301(5635), 945-948.

Stärz, M., X. Gong, R. Stein, D. A. Darby, F. Kauker and G. Lohmann (2012), Glacial shortcut of Arctic sea-ice transport, *Earth Planet Sc Lett.* (accepted).

Steele, M., R. Morley, and W. Ermold (2001), PHC: A global ocean hydrography with a highquality Arctic Ocean, *J. Clim.*, 14, 2079-2087.

Stepanek, C., and G. Lohmann (2012), Modelling mid-Pliocene climate with COSMOS. *Geosci. Model Dev.*, 5, 1221-1243, doi:10.5194/gmd-5-1221-2012.

Stevens, D. P. (1991), The open boundary condition in the United Kingdom Fine-Resolution Antarctic Model, *J. Phys. Oceanogr.* 21, 1494-1499.

Stommel, H (1961), Thermohaline convection with two stable regimes of flow, *Tellus*, 13, 224-230.

Storch, v. H. and F. W. Zwiers (2002), *Statistical Analysis in Climate Research*, ISBN-13: 978-0521012300, Cambridge University Press.

Thompson, W. G., and S. L. Goldstein (2006), A radiometric calibration of the SPECMAP timescale, *Quaternary Sci Rev*, 25(23-24), 3207-3215.

Thornalley, D. J., S. Barker, W. S. Broecker, H. Elderfield, and I. N. McCave (2011), The deglacial evolution of North Atlantic deep convection, *Science*, 331(6014), 202-205.

Treguier, A. M., S. Theetten, E. P. Chassignet, T. Penduff, R. Smith, L. Talley, J. O. Beismann, and C. Boning (2005), The North Atlantic subpolar gyre in four high-resolution models, *J Phys Oceanogr*, 35(5), 757-774.

Van Meerbeeck, C. J., H. Renssen, and D. M. Roche (2009), How did Marine Isotope Stage 3 and Last Glacial Maximum climates differ? - Perspectives from equilibrium simulations, *Clim Past*, 5(1), 33-51.

Vautravers, M. J., N. J. Shackleton, C. Lopez-Martinez, and J. O. Grimalt (2004), Gulf Stream variability during marine isotope stage 3, *Paleoceanography*, 19(2).

Velichko, A.A., Y. M. Kononov, M. A. Faustova (1997), The last glaciation of earth: Size and volume of ice-sheets. *Quaternary Int.* (0), 43-51.

Waelbroeck, C., L. Labeyrie, E. Michel, J. C. Duplessy, J. F. McManus, K. Lambeck, E. Balbon, and M. Labracherie (2002), Sea-level and deep water temperature changes derived from benthic foraminifera isotopic records, *Quaternary Sci Rev*, 21(1-3), 295-305.

Walker G.T. (1924), Correlations in seasonal variations of weather IX. *Mem Ind Meteor Dept* 24:275-332.

Wanner, H. , J. Beer, J. Bütikofer, T. J. Crowley, U. Cubasch, J. Flückiger, H. Goosse, M. Grosjean, F. Joos, J. O. Kaplan, M. Küttel, S. A. Müller, I. C. Prentice, O. Solomina, T. F. Stocker, P. Tarasov, M. Wagner, and M. Widmann (2008), Mid- to Late Holocene climate change: an overview, *Quaternary Sci Rev*, 27(19-20), 1791-1828.

Wei, W., and G. Lohmann (2012), Simulated Atlantic Multidecadal Oscillation during the Holocene, *J. Climate* (in press), <http://dx.doi.org/10.1175/JCLI-D-11-00667.1>.

Wei, W., G. Lohmann, and M. Dima (2012), Distinct Modes of Internal Variability in the Global Meridional Overturning Circulation Associated with the Southern Hemisphere Westerly Winds, *J Phys Oceanogr*, 42(5), 785-801.

Welander, P. (1982), A Simple Heat Salt Oscillator, *Dynam Atmos Oceans*, 6(4), 233-242.

Wolff, E. W., J. Chappellaz, T. Blunier, S. O. Rasmussen, and A. Svensson (2010), Millennial-scale variability during the last glacial: The ice core record, *Quaternary Sci Rev*, 29(21-22), 2828-2838.

Zalesak, S. T. (1979), Fully multidimensional flux-corrected transport algorithms for fluids, *J. Comput. Phys.*, 31, 335-362.

Zhang, X., G. Lohmann, G. Knorr, and X. Xu (2012), Two ocean states during the Last Glacial Maximum, *Clim. Past Discuss.*, 8, 3015-3041, 2012, doi:10.5194/cpd-8-3015-2012.

Zhao, M., N. A. S. Beveridge, N. J. Shackleton, M. Sarnthein, and G. Eglinton (1995), Molecular Stratigraphy of Cores Off Northwest Africa Sea-Surface Temperature History over the Last 80 Ka, *Paleoceanography*, 10(3), 661-675.

## 8 Acknowledgement

I am particularly grateful to my supervisor Prof. Dr. Gerrit Lohmann, always giving advices and support during my PhD study. Thank you for many opportunities that you have provided and the help you offered in those endeavors.

The PhD study presented in this text is funded by the Helmholtz Graduate School for Polar and Marine Research (POLMAR). I would like sincerely appreciate the help from POLMAR office (Prof. Dr. Jelle Bijma, Dr. Claudia Hanfland, Dr. Claudia Sprengel and Mrs. Dörte Burhop).

Additionally, many thanks are given to my colleagues in the group of Paleoclimate Dynamics, especially Dr. Gregor Knorr, Michael Stärtz, Xu Zhang, Christian Stepanek, Wei Wei, Madlene Pfeiffer, Conor Purcell, Sagar Bora, Paul Gierz and Prof. Dr. Xiangdong Zhang from International Arctic Research Centre (Alaska, USA). We work together to solve many technical problems, and my research work benefits a lot from your guidance and our fruitful discussions. Without you, my PhD study will not be as enjoyable and successful as it is.

Especially, I would like thank my wife Xuemei Su, my families and other friends for your support and encouragement.

## Table of contents

1	Introduction.....	1
2	Methodology.....	9
2.1	Model description for the COSMOS model.....	9
2.2	Model description for the COSMOS model.....	12
2.3	Statistical Analysis .....	14
3	Intensification of Glacial North Atlantic Gyres and Meridional Overturning Circulation due to elevated Northern Hemisphere Ice Sheet.....	15
3.1	Experiment design for five climate states during the last glacial-interglacial cycle .....	18
3.2	COSMOS simulations for five climate states.....	21
3.2.1	The North Atlantic surface winds .....	21
3.2.2	Sea surface temperature and sea ice .....	21
3.2.3	North Atlantic surface circulation and AMOC .....	31
3.3	Discussion: distinct features of glacial North Atlantic Ocean circulation from interglacial climate states .....	34
3.3.1	Strengthened glacial North Atlantic gyres due to stronger wind stress .....	34
3.3.2	Barotropically strengthened glacial Gulf Stream.....	37
3.3.3	Stronger glacial AMOC associated with intensified North Atlantic gyres.....	40
3.4	Discussion: the effect of elevated North-hemisphere ice sheet to the surface North Atlantic Ocean circulation during the glacial climate periods .....	41
4	Dependence of abrupt Atlantic meridional ocean circulation changes on climatic states .....	43
4.1	Design of hosing experiments .....	45
4.2	Results: distinct recovery features of AMOC on different climate states.....	49
4.2.1	Initial resumption of the AMOC .....	49
4.2.2	The AMOC overshoot .....	51
4.3	Discussion: the alternative role of the South Labrador Sea in triggering glacial AMOC overshoot ..	57
5	Dynamics perspective of the GLAMAP/CLIMAP discovered extreme sea-surface conditions in the Nordic Seas during the Last Glacial Maximum .....	59
5.1	Experiments and atmospheric forcing.....	61
5.1.1	Design of NAOSIM experiments .....	61
5.1.2	Atmospheric forcing .....	65
5.1.3	Design of sensitivity study experiments.....	66
5.2	Results of high-resolution NAOSIM experiments.....	67
5.2.1	The experiment for present-day Nordic Seas.....	67
5.2.2	The CLIMAP reconstruction and NAOSIM-C experiment .....	70
5.2.3	The GLAMAP reconstruction and NAOSIM-G experiment .....	74
5.2.4	The sensitivity study of sea surface salinity restoring .....	78
5.2.5	The sensitivity study of open ocean boundary .....	79
5.2.6	The sensitivity study of the ocean gateway.....	82
5.3	NAOSIM discovered hydrographic features of the surface Nordic Seas during the LGM.....	85
5.4	What we learn from NAOSIM sensitivity study experiments .....	91
5.5	Messages from NAOSIM experiments for the LGM .....	92
6	Conclusions and future perspectives .....	93
7	Reference.....	98
8	Acknowledgement.....	114